UNIVERSITY OF GENOA
Department of Physics
Doctoral School in Physics

ISTITUTO ITALIANO DI TECNOLOGIA
Nanoscopy & NIC@IIT

EXPLOITING OPTICAL NON-LINEARITIES FOR SUPER-RESOLUTION LABEL-FREE OPTICAL MICROSCOPY

Supervisor:
Prof. Alberto DIASPRO
Co-supervisor:
Dr. Paolo BIANCHINI

Doctoral dissertation of:
Giulia ZANINI
Matr. 4168210

XXXI Doctoral Cycle
26th March 2019

Ai miei genitori

"I don't know where I'm going but I know where I belong"

Alan Doyle

Acknowledgments

The accomplishment of this Ph.D. thesis was made possible thanks to the guidance and the support of many people, which, from far and from near, took care of my scientific and my personal growth.

First of all, I would like to thank Prof. Alberto Diaspro, head of the Nanoscopy and NIC@IIT research group at Istituto Italiano di Tecnologia, for giving me the chance to be part of his team. In these three years I had the opportunity to work in one of the best optical microscopy research groups, which he formed with immense passion and dedication, and where I could learn really putting my hands on things. Thanks for the lab retreats, for the meetings, for the challenging questions, and for sharing science to the community. Thanks for supporting my research experience in Japan.

Thanks to Dr. Paolo Bianchini for supervising me during the Ph.D. project in IIT. Thanks for teaching me as much as you could about optics, alignment, optical devices, microscopy… Thank you for letting me follow you while you were working in the lab to (indirectly) learn even more. Thank you for devoting some of your time for discussing results and planning the next move, and for accepting my irruptions in your office while you were busy with other tasks: I understand the effort in juggling so many appointments!

Thanks to Dr. Kseniya Korobchevskaya, who started this project before my arrival, providing an excellent basis for moving forward with the research. Thank you for the time you spent in reading and improving the paper, even from far away.

I am deeply grateful to Dr. Takahiro Deguchi, colleague and friend, who supported my work from the beginning and was always ready to help when needed. Thank you for your kindness, and for the time spent with your family, here in Genova and in Osaka. ありがとうございます.

Thanks to Dr. Fumihiro Dake from Nikon Japan, with whom I had the possibility to collaborate at the beginning of this project. Thank you for the time you spent with me in the lab, for sharing your knowledge, for the stimulating discussions.

I would like to thank Prof. Jörg Enderlein (University of Göttingen) and Prof. Ammasi Periasamy (University of Virginia) for spending time in reading and revising this thesis, giving value to my work and suggesting how to improve it.

A special thanks goes to all the Nanoscopy group, to all past and new members I have met, without whom these three years would have not been the same. Thanks for supporting and helping when needed, thanks for plenty of jokes and laughs and relaxing time, thanks for letting me share my best and my hard times, thanks for accepting my ups and downs. A special thanks to Melody and Luca, who started this journey with me, for facing together courses and schools, for managing to open and close missions (what an adventure!), for being supportive also in bad

moments. An additional special thanks to the administrative assistant Manuela Salvatori, for her organizational skills and her prompt solutions.

I would like to thank Fujita-sensei, head of the LASIE group at Osaka University, for accepting my visit to his lab, for proposing the project and supervising the achievements step by step. Thanks to Koike-kun and Kawagoe-san for their full support in the lab from the very first day till the last one. Thanks for facing the problems together, especially for becoming masters of OPO alignment! Thanks to all the LASIE group for the birthday parties, for the "Buon Compleanno" on my birthday cake, for cooking all together, for sharing gifts at Christmas, for the karaoke, for sharing cultures. ありがとうございます.

Living this new Ph.D. life in Genova would have not been the same without establishing new good relationships, and spending memorable moments with new friends. Thanks *in primis* to Chiabrera house for welcoming me in Genova, to Chiara, Themi, Roberta, Irene and Emma for being amazing flatmates! Thanks to Amira, Barbara, Dario, Michela, Oscar, Marco and Irene for all the good memories I have from the very beginning, for all the lunches and the aperitivi and the Christmas and birthday parties! Thanks to Sep, Romeo, Silvia, Misha, Amira, Melody and Alex for being amazing pals in the 9-seats van trip to Slovenia and for sharing lots of sushi lunches in Piccapietra. Thanks to Bertrand, Coralie and little Eliott for sharing the joy of their family. Thanks to Nuno and Diana for enjoying the swing course together. Thanks to Gio21 choir for the opportunity to play and sing with them, as feeling at home!

My deepest thanks to Алекс, strong and brilliant Doctor *cum laude*, who has always been by my side in these tough years, who has never stopped believing in my possibilities and who has incessantly and fondly encouraged me to believe in myself. Thank you for pushing me to do an experience in Japan, it was definitely worth it! Thank you for all the experiences we shared, for all the places we visited together, for sharing good and bad moments. Мерси!

Going back home, where my roots will always be, thanks to my dear friends for caring and for making me feel loved even if far apart and even if we chose different paths in life. A big thanks to my university friends, the peculiar community Fisici-TN, which is now spread all over the world but which does not forget its origin in quel di Povo. It is always nice to meet you once in a while, with new stories to tell, new families to meet, new achievements to celebrate!

Finally, I would like to address my deepest thanks to my parents, Nicoletta and Fulvio, for being always supportive and encouraging, for being genuine in giving suggestions or in questioning choices, for have always been there to guide my path. Thanks to my grandparents, Claudia, Silvio, Carla and Mario, for their wise advices and their warm embraces. Thanks to all my family, who has always been fondly interested in my scientific studies and career. Grazie a tutti voi!

With love,

Giulia

Summary

Optical microscopy uniquely provides non-invasive imaging of biological specimens and has become an essential tool in life sciences. So far, fluorescence microscopy techniques have been the most widely used due to their ability to visualize the molecules of interest with high contrast, high specificity, and high spatial and temporal resolution. In the last decades, much effort was put into the development of advanced super-resolution fluorescence microscopy techniques to circumvent the diffraction limit and image with unprecedented spatial resolution. The non-linearities contained in saturation phenomena were exploited for this purpose, and led to the development of techniques like stimulated emission depletion (STED) and saturated excitation (SAX) microscopy, which proved to have the potentiality to really break the diffraction barrier and tune the resolution down to infinitely small focal volumes (**Chapter 1**). Despite their well-established benefits, (super-resolution) fluorescence microscopy techniques rely on the photophysical properties of fluorescent molecules to obtain the desired contrast and resolution, and the labeling procedures may alter the physical properties of the specimen and may come at the cost of photobleaching and photodamage effects.

With the development of ultrashort pulsed laser sources, new types of non-linear optical interactions became accessible (**Chapter 1**) and started to acquire a central role in optical microscopy for label-free imaging, providing novel non-fluorescence-based contrast mechanisms which purely rely on intrinsic properties of the molecules of interest. In this way, the invasiveness and the phototoxicity can be reduced, and the degradation of the fluorescence signal due to photobleaching can be avoided. Moreover, non-linear optical microscopy techniques allow for three-dimensional imaging due to the intrinsic optical sectioning capabilities of non-linear phenomena, while the use of longer wavelengths in the near-infrared part of the spectrum results in lower absorption and scattering and permits to image deeper inside tissues (**Chapter 1**). The main drawback of these non-linear optical microscopy techniques is their relatively poor spatial resolution, especially when using longer excitation wavelengths, and the fact that the imaging of non-fluorescent species with sub-diffraction resolution is still a challenging task.

In this framework, **this work aims at extending the super-resolution approaches to label-free microscopy techniques**, based on the fact that, in principle, any saturable optical process between molecular states, not necessarily involving fluorescent transitions, is a potential candidate for breaking the diffraction barrier.

In particular, non-linear optical processes are here exploited in near-infrared pump-probe microscopy techniques, such as transient absorption microscopy (TAM) and stimulated Raman

scattering (SRS) microscopy (**Chapter 3**). In these techniques, two synchronized femto/pico-second pulsed laser beams are used to investigate ultrafast electronic and vibrational dynamical properties of the sample with high spatial and temporal resolution, high sensitivity and high chemical specificity. The interaction with the sample is recorded as an intensity variation of one of the two beams, which is extracted from the background adding a fast intensity modulation and filtering with a lock-in amplifier. New dynamical and chemical information can be accessed at the molecular level and in a label-free way, using intrinsic biomolecules as natural contrast agents.

Absorption-based pump-probe microscopy is here optimized to retrieve structural and dynamical information from graphene-based samples with high sensitivity, and its conventional configuration is combined with an additional doughnut-shaped pump beam, which allows for the reduction of the effective focal volume exploiting transient absorption saturation. By optimizing the experimental parameters, such as power and temporal overlap of the saturation beam, single layer graphene deposited on a glass surface can be imaged at the nanoscale (**Chapter 4**).

Moreover, the saturation of the vibrational excitation in SRS microscopy is here theoretically and experimentally assessed, in order to evaluate the applicability of the SAX approach to achieve isotropic sub-diffraction imaging capabilities (**Chapter 5**).

Table of Contents

Table of Figures

Table of Abbreviations

3D	Three-dimensional
AOM	Acousto-optic modulator
APD	Avalanche photodiode
BBO	Beta barium borate
BS	Beam splitter
CARS	Coherent anti-Stokes Raman scattering
CCD	Charge-coupled device
CRS	Coherent Raman scattering
CVD	Chemical vapour deposition
DFG	Differential frequency generation
DL	Delay line
DM	Dichroic mirror
dSAX	Differential saturated excitation
DTA	Differential transient absorption
EOM	Electro-optic modulator
ESA	Excited state absorption
FOV	Field of view
FSRS	Femtosecond stimulated Raman scattering
FT	Fourier transform
FWHM	Full width at half maximum
FWM	Four wave mixing
GSD	Ground state depletion
HWP	Half wave plate
IC	Internal conversion
IPSF	Illumination point spread function
ISC	Intersystem crossing
ISRS	Impulsive stimulated Raman scattering
LIA	Lock-in amplifier
LP	Long-pass filter
mSAX	Modulated saturated excitation
NA	Numerical aperture
NC	Nanocrystal
ND	Neutral density filter

NIR	Near-infrared
OPA	Optical parametric amplification
OPO	Optical parametric oscillation/oscillator
PBS	Polarizing beam splitter
PD	Photodiode
PMMA	Poly(methyl methacrylate)
PMT	Photomultiplier
PP	Pump-probe
PSF	Point spread function
QWP	Quarter wave plate
RESOLFT	Reversible saturable optical linear fluorescence transition
SAX	Saturated excitation
SBS	Stimulated Brillouin scattering
SE	Stimulated emission
SFG	Sum frequency generation
SHG	Second harmonic generation
SLG	Single layer graphene
SLM	Spatial light modulator
SNR	Signal-to-noise ratio
SP	Short-pass filter
SPP	Saturated pump-probe
SPPM	Structured pump-probe microscopy
SRG	Stimulated Raman gain
SRL	Stimulated Raman loss
SRS	Stimulated Raman scattering
STED	Stimulated emission depletion
SU	Scanning unit
SWNT	Single-walled carbon nanotubes
TAM	Transient absorption microscopy
THG	Third harmonic generation
TPA	Two-photon absorption
TPEF	Two-photon excited fluorescence
UV	Ultraviolet
VIS	Visible
VPP	Vortex phase plate
VR	Vibrational relaxation

PART ONE: THEORETICAL BACKGROUND

1. Light-matter interactions

Light is an important tool in our everyday life since it provides us with visual information about the world around us. Familiar optical phenomena like reflection, refraction, and absorption, which permit us to see the colors or to focus the light by a lens, are a consequence of the interaction of light with matter. They can be explained taking into account the wave-like nature of light and assigning a small set of optical parameters to the material. In normal conditions, these parameters are constant, independent on the intensity of the light used to observe optical phenomena. This is the realm of **linear optics**, which is valid when low intensities are used. With the advent of lasers in the 1960s, it became possible to focus the laser beam in a tiny spot of high local irradiance, which led to the generation of new optical phenomena. At such high powers, the optical parameters of the material cannot be considered constant anymore but become a function of the light intensity. This is the science governed by **non-linear optics**.

Both linear and non-linear optical effects can be understood considering the interaction of the electric field component of the electromagnetic radiation (i.e., light) with the charged particles (i.e., positive nuclei and negative electrons) which constitute the matter. In a dielectric (non-conducting) medium with neutral total charge, an applied oscillating electric field $\boldsymbol{E}(\boldsymbol{r},t) = \boldsymbol{E_0} \cdot \cos(\boldsymbol{k}\bullet\boldsymbol{r} - \omega t)$ ($\boldsymbol{E_0}$ amplitude, $\boldsymbol{k}$ wavevector, ω angular frequency) induces forced oscillations of the bound charges (i.e., dipoles) through the driving force exerted on the electrons. The result is the generation of a *microscopic* electric dipole moment

$$\boldsymbol{p}(t) = -e \cdot \boldsymbol{d}(t) \qquad \textbf{(1.1)}$$

where $\boldsymbol{e}$ is the charge of the electron and $\boldsymbol{d}(t)$ is its time-varying displacement from the equilibrium position.

If the external electromagnetic field oscillates at a frequency ω that coincides with a natural frequency of the atom, then a *resonance* phenomenon occurs and the atom can absorb energy from the light. The absorption strength is characterized by the **absorption coefficient** $\alpha(\omega)$. The atom jumps to an excited state and, once excited, it can return to the ground state via radiation-less transitions (heat conversion) or via luminescence transitions (light emission), as shown in the Jablonski diagram in **Figure 1.1**. If ω is not in resonance, the atom will not absorb and the medium will be transparent. In this case, the wave drives non-resonant oscillations of the atoms that will propagate through the medium with a phase lag, meaning that the wave will travel with lower velocity in the medium respect to free space. This velocity reduction is governed by the **refractive index** $n(\omega)$ of the material. $\alpha(\omega)$ and $n(\omega)$ are the main quantities that optically characterize the material.

The *macroscopic* electric polarization of the medium is the relevant quantity that couples with the radiation and it is defined as the net average dipole moment per unit volume

$$\boldsymbol{P}(t) = N\langle \boldsymbol{p}(t) \rangle \qquad \textbf{(1.2)}$$

where $\boldsymbol{N}$ is the number of microscopic dipoles per unit volume, and the angular brackets define the average operation over all the dipoles in the medium. In this way, any permanent dipole that does not oscillate at the external frequency is ignored [1]. $\boldsymbol{P}(t)$ can be expanded in powers of the electric field. In this way, linear and non-linear optical phenomena can be classified by looking at the power law dependence.

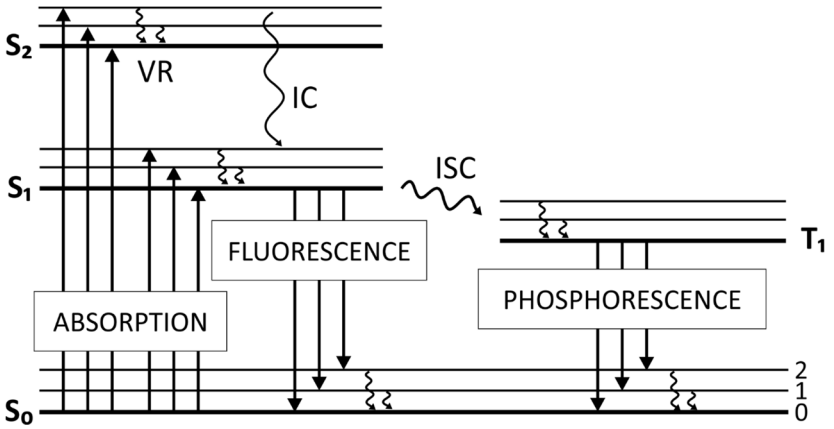

Figure 1.1 Jablonski diagram representing the main transitions between electronic (thick horizontal lines) and vibrational (thin horizontal lines) states. Radiative transitions (absorption, fluorescence emission and phosphorescence emission) are indicated by straight arrows. Non-radiative transitions (vibrational relaxation (VR) between vibrational states, internal conversion (IC) between electronic states, and intersystem crossing (ISC) between singlet and triplet states) are represented by wavy arrows.

1.1. Linear optics

In the limit of weak applied electric fields (compared to the field that binds the electron to the nuclei), the electron binding potential can be considered harmonic, and the dipoles can be modeled as damped harmonic oscillators. In this case, the displacement $\boldsymbol{d}(t)$ results to be proportional to the electric field, and so that the polarization which can be written as

$$\boldsymbol{P}(\boldsymbol{E}) = \varepsilon_0 \boldsymbol{\chi}^{(1)} \bullet \boldsymbol{E} \qquad (1.3)$$

where ε_0 is the electric permittivity of free space and $\boldsymbol{\chi}^{(1)}$ is the **(linear) electric susceptibility tensor** of the medium.

The susceptibility tensor has, in the most general case, nine independent components $\chi_{ij}^{(1)}$. In an *isotropic* medium, it reduces to only one independent, non-zero component and it can be written as a scalar quantity, $\chi^{(1)}$. The susceptibility is related to the **(relative) dielectric constant** ε_r of the material by the relation $\varepsilon_r = 1 + \chi^{(1)}$. Both ε_r and $\chi^{(1)}$ are complex and frequency-dependent quantities that can be derived as

$$\begin{cases} \sqrt{\varepsilon_r(\omega)} = n(\omega) + i\frac{\alpha(\omega)}{4\pi} \\ \chi^{(1)} = \chi_R^{(1)} + i\chi_I^{(1)} \end{cases} \qquad (1.4)$$

where subscript R stands for real and subscript I stands for imaginary part. The real part is governed by the refractive index $n(\omega)$, which characterizes the *dispersive* behavior of the material. The imaginary part is governed by the absorption coefficient $\alpha(\omega)$, which represents the *absorption* properties of the material, as previously introduced.

Linear optics describes many processes involving a weak incoming electromagnetic field propagating through an optical medium (**Figure 1.2**). The optical processes can be categorized as

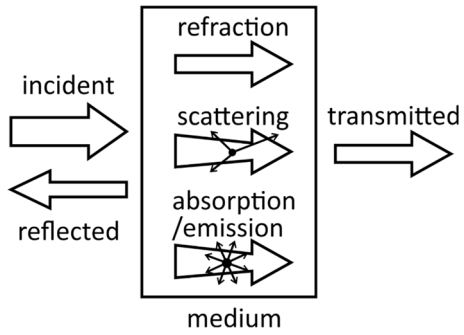

Figure 1.2 Representation of the main linear interactions involving a light beam incident on an optical medium: reflection, transmission, refraction, scattering and absorption (with possible consequent emission). Adapted from [2].

(i) **parametric**, if the light interacts instantaneously with the matter, without any net transfer of energy, momentum, or angular momentum between the field and the system.

Examples are *reflection*, *refraction*, *diffraction* and *elastic scattering*. These processes are governed by the real part of the susceptibility.

(ii) **non-parametric**, if they involve a change in the quantum states. Examples are *inelastic scattering*, *absorption* and *emission*. These processes are governed by the *imaginary* part of the susceptibility.

1.1.1. Reflection

The incident wave bounces off the interface with an angle $\theta_r = \theta_i$, where subscript i stands for 'incident' and subscript r stands for 'reflected'.

1.1.2. Refraction

The portion of light not reflected at the interface will propagate through the material with a velocity $v = c/n$, where c is the speed of light in vacuum and n is the refractive index. This velocity reduction leads to the bending of the light rays, governed by the *Snell's law* $n_i \sin\theta_i = n_t \sin\theta_t$, where subscript i stands for 'incident' and subscript t stands for 'transmitted'.

1.1.3. Diffraction

When a wave encounters an obstacle or an aperture, it bends around the object's corners. In classical physics, this phenomenon is explained as the result of *interference* of waves (i.e., wave superimposition), according to the *Huygens–Fresnel principle* that treats each point in the wavefront as a source, at a given instant, of secondary spherical waves. The diffraction results more pronounced when the obstacle's linear dimension is comparable to the wavelength of the radiation. The diffraction of light by small structures is the process governing image formation in a light microscope, as it will be better explained in **Chapter 1**.

1.1.4. Scattering

As a result of non-uniformities present in the material system, the light changes the direction of propagation (and, in some cases, also the frequency), leading to a decrease in the forward transmission intensity. Scattering events can be classified as:

(i) *elastic*, if the frequency of the scattered light does not change. Depending on the dimension a of the scattering centers (compared to the incident wavelength λ), scattering is called *geometric* ($\alpha \gg \lambda$), *Mie* ($\alpha \sim \lambda$) or *Rayleigh* ($\alpha \ll \lambda$). In Rayleigh approximation, the scattering efficiency is inversely proportional to the fourth power of the wavelength ($\propto 1/\lambda^4$).

(ii) *inelastic,* if new output frequencies appear after energy transfer with the medium. Components of the scattered light that are shifted to lower frequencies are known as

Stokes components, while those components that are shifted towards higher frequencies are known as *anti-Stokes* components (**Figure 1.3**). An example of inelastic scattering is *Raman scattering*, which involves the generation of vibrational quanta (i.e., phonons) in the material.

Scattering phenomena can also be classified as:

(i) *spontaneous*, when the optical properties of the material remain unmodified by the incident light field. This is the description of a linear process.

(ii) *stimulated*, if the optical properties modifications that lead to scattering are induced by the presence of the light field. This is a non-linear process.

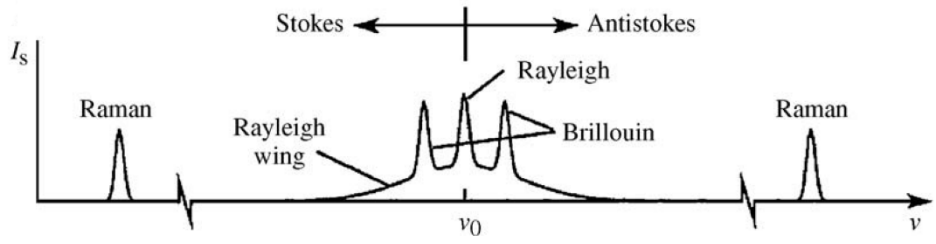

Figure 1.3 Typical observed spectrum from a spontaneous light scattering experiment, showing a peak at the incident frequency $\omega_0 = 2\pi\nu_0$ (elastic Rayleigh scattering), and additional peaks at lower (Stokes) and higher (anti-Stokes) frequencies, correspondent to Raman and Brillouin inelastic scattering processes. Taken from [3].

Finally, they can be characterized depending on the phase relationship between multiple scattered waves (**Figure 1.4**):

(i) scattering is *coherent* when the phases of the signals arising from different scattering centers are correlated, and interference phenomena between the different scattered paths may be taken into consideration to obtain useful structural information. This type of scattering is mostly forward-directed.

(ii) scattering is *incoherent* when no correlation exists between the phases, and the single scattering events may be considered independently.

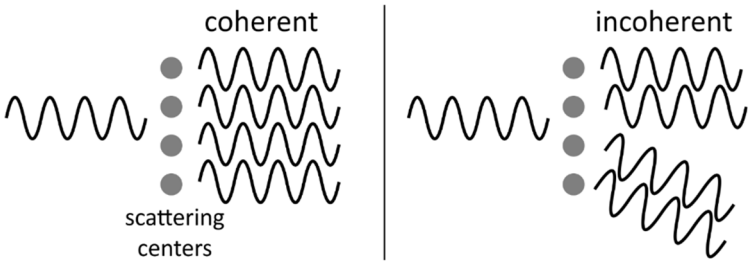

Figure 1.4 Comparison between coherent and incoherent scattering phenomena.

Spontaneous Raman scattering. Raman scattering is an *inelastic* type of linear scattering, discovered in 1928 by the Indian physicist Sir Chandrasekhara Venkata Raman. In this process, scattered light ends up containing frequencies different from the excitation ones due to the interaction of the incident field with vibrational quanta (i.e., phonons) of the material having a defined frequency (i.e., energy). The new frequencies that appear are $\omega_s = \omega_p - \omega_v$ (*Stokes frequency*) and $\omega_{as} = \omega_p + \omega_v$ (*anti-Stokes frequency*), where ω_p is the incident (or pump) frequency and ω_v is the vibrational frequency of the material (**Figure 1.5**). The anti-Stokes lines are typically much weaker than the Stokes ones because, in thermal equilibrium, the population of the vibrational level is smaller than the population of the ground state. Spontaneous Raman scattering is a weak process, with cross sections of the order of 10^{-30} cm^2, much smaller than the typical absorption ones (~10^{-18} cm^2).

Stimulated Raman scattering is the non-linear variant of this scattering phenomenon, where the molecular vibrations are induced by the incident fields, and it will be introduced in **Section 1.2.2**.

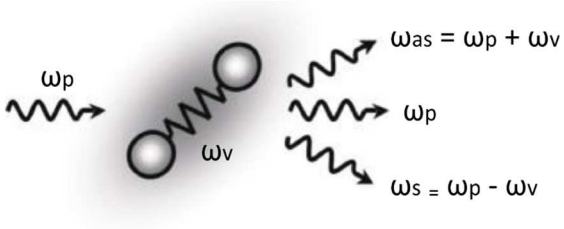

Figure 1.5 Representation of the spontaneous Raman scattering process. Adapted from [4].

1.1.5. Absorption/emission

Light absorption accounts for all the transmission losses not caused by reflection or scattering. It occurs when the incident light frequency matches a natural frequency of the molecules so that energy can be absorbed promoting electrons to an excited state. Generally, absorption of one-photon in the ultraviolet (UV) or visible (VIS) spectral range occurs.

Among all the possible de-excitation pathways (see **Figure 1.1**), *photoluminescence* can accompany the propagation of light in an absorbing medium. The light is emitted isotropically, and usually at a different frequency respect to the absorbed one. *Fluorescence* and *phosphorescence* are particular cases of photoluminescence. Fluorescence happens when the excited electron is found in a singlet state and hence the transition to the ground state is spin allowed. This transition occurs rapidly, within a time of the order of nanoseconds (10^{-9} s). On the contrary, phosphorescence persists in time (in the order of ms-s), because it involves an excited electron in a triplet state whose transition to the ground state is spin forbidden.

The emission rate of photoluminescence phenomena results to be linear to the excitation rate.

1.2. Non-linear optics

For stronger applied electric fields, comparable with the typical atomic electric field (~10^{11} V/m) [3], the electron is farther displaced from its equilibrium position and the binding potential can be no longer considered harmonic. When anharmonic effects start to appear, the dependence of the induced macroscopic polarization respect to the field is no more linear. In general, the applied electric fields are small compared to the interatomic forces, even when focused light is used, and so the non-linearity is weak. This permits to expand the function that relates $\boldsymbol{P}$ to $\boldsymbol{E}$ in a Taylor series about $\boldsymbol{E}$=0

$$\boldsymbol{P}(\boldsymbol{E}) = \varepsilon_0\left(\boldsymbol{\chi}^{(1)}\bullet\boldsymbol{E} + \boldsymbol{\chi}^{(2)}\bullet\boldsymbol{E}^{\boldsymbol{2}} + \boldsymbol{\chi}^{(3)}\bullet\boldsymbol{E}^{\boldsymbol{3}}+\ldots\right) \quad \textbf{(1.5)}$$

where $\boldsymbol{\chi}^{(n)}$ is the *n*th order susceptibility tensor. The high-order power dependence is transferred also in the refractive index $\boldsymbol{n}$ and in the absorption coefficient $\boldsymbol{\alpha}$ of the material.

Most of the non-linear phenomena involve the second- and the third-order susceptibilities, $\chi^{(2)}$ and $\chi^{(3)}$, respectively. For condensed matter, giving $\chi^{(1)}$ in the order of unity, $\chi^{(2)}$ is expected to be of the order of 10^{-12} m/V [3]. Moreover, $\chi^{(2)}$ must vanish in centrosymmetric media with inversion symmetry, since the function $\boldsymbol{P}(\boldsymbol{E})$ must have odd symmetry [5]. $\chi^{(3)}$, which is present in any media (liquid, gases, amorphous solids and even crystals with inversion symmetry) is expected to be in the order of 10^{-24} m^2/V^2 [3].

The non-linear coefficients result to be many orders of magnitude smaller than the linear one, which means that non-linear optical effects require high incident powers to become relevant. The advent of lasers in the 1960s made possible to achieve enough local irradiance in a tiny spot. Moreover, the development of more advanced ultrashort pulsed laser sources consisting of pico-/femto-second pulses permitted to achieve even higher peak powers while keeping a low average power to prevent sample damage.

Non-linear optical interactions deal in particular with non-linear frequency conversion (conversion of input light to light of other frequencies), with the non-linear variation of the refractive index, and with non-linear absorption processes. The main second- and third-order non-linear optical processes are reported in **Table 1.1**. The interactions that will be discussed in this thesis and exploited in non-linear optical microscopy are there highlighted in bold.

As can be seen, the attention will be focused on **third-order non-parametric processes**, which result from $\boldsymbol{E}^{\boldsymbol{3}}$ interactions and which lead to a total of 108 terms correspondent of all the possible permutations of three fields at frequencies ω_1, ω_2 and ω_3 [6]. The non-linear polarization occurs at frequencies given by $\omega_4 = \pm\omega_i \pm \omega_j \pm \omega_k$, for $i,j,k = 1,2,3$: a positive sign represents the absorption of a photon, while a negative sign represents the generation of a photon, and the energy is conserved. Important third-order mechanisms are

	Parametric	Non-parametric
Second-order, $\chi^{(2)}$	• Second harmonic generation (SHG) • Sum and difference frequency generation (SFG, DFG) • Optical parametric amplification and oscillation (OPA, OPO)	
Third-order, $\chi^{(3)}$	• Third harmonic generation (THG) • Four-wave mixing (FWM) • Coherent anti-Stokes Raman scattering (CARS) • Kerr effect	• **Non-linear absorption** / Two-photon absorption (TPA) • **Stimulated Raman scattering (SRS)** • Stimulated Brillouin scattering (SBS)

Table 1.1 Classification of the main second- and third-order non-linear optical processes. The interactions that will be discussed in this thesis and exploited in non-linear optical microscopy are highlighted in bold.

illustrated in **Figure 1.6**, where S_0 represents the ground state and $|1\rangle$, $|2\rangle$ and $|3\rangle$ represent intermediate (electronic, vibrational and/or virtual) states of the system:

(a) consecutive absorption of three photons and consequent emission of one photon, as in sum frequency generation (SFG) and, as a particular case, in third harmonic generation (THG) where $\omega_1 = \omega_2 = \omega_3$;

(b) absorption-emission-absorption-emission sequence (**Raman-type resonance**), as in difference frequency generation (DFG), four-wave mixing (FWM) and coherent Raman scattering (CRS), where $\omega_1 - \omega_2 = \omega_3 - \omega_4$;

(c) absorption of two photons (**two-photon resonance**) followed by an emission, as in two-photon absorption (TPA).

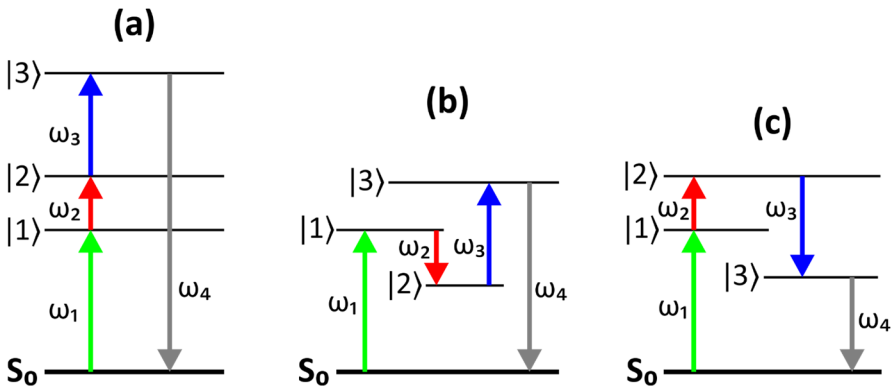

Figure 1.6 Transition diagrams of the main types of third-order non-parametric processes: **(a)** three-photon resonance, **(b)** Raman-type resonance, **(c)** two-photon resonance. S_0 represents the ground state and $|1\rangle$, $|2\rangle$ and $|3\rangle$ represent intermediate electronic, vibrational and/or virtual states. Three photons ω_1, ω_2 and ω_3 non-linearly interact generating a new photon at frequency ω_4. Adapted from [7].

These processes represent resonance conditions, governed by the imaginary part of the third-order susceptibility $\chi_I^{(3)}$. Two-photon and Raman-type resonances will be discussed in **Section 1.2.1** and **Section 1.2.2**, respectively.

1.2.1. Non-linear absorption

Non-linear absorption refers to the change in transmittance of a material as a function of the incident intensity. A subgroup of interactions consists of transitions due to a two-photon resonance (**Figure 1.6(c)**), such as *two-photon absorption* and *excited state absorption*, governed by the imaginary part of the third-order susceptibility $\chi_I^{(3)}$. As a consequence of high intensity fields, more complicated transitions may occur in the material, such as *saturable absorption* and *stimulated emission*.

Using two distinct ultrashort pulsed incident beams, commonly named **pump** and **probe**, different non-linear absorption mechanisms can be studied looking at the *probe difference absorption* signal, in the presence and in the absence of the pump beam. Pump-probe interactions can be studied as a function of pump wavelength, probe wavelength, and also delay time between the two pulses, and they can be implemented on a microscopy platform as it will be explained in **Section 3.3**.

Two-photon absorption (TPA). Two-photon absorption consists of the *simultaneous* absorption of two photons to match the (usual) one-photon transition between ground and excited state. The "simultaneity" is achieved within a time window of the order of 10^{-16} s [8,9], which is in the scale of molecular energy fluctuations. In this case, the intermediate state ($|1\rangle$ in **Figure 1.6(c)**) is a *virtual* one. Usually, the one-photon transition is achieved via the absorption of a UV-VIS photon, which means that longer wavelengths (smaller frequencies), towards the near-infrared (NIR) part of the spectrum, need to be used for a TPA process to happen.

Two situations can happen (**Figure 1.7(a,b)**):

(i) a *single field* is used and two photons at the same frequency ω_{2P} are absorbed. In terms of wavelengths, doubling the maximum single-photon excitation wavelength seems to be a good approximation in order to determine an optimal TPA wavelength. However, many molecules exhibit deviations from this rule because the selection rules for two-photon processes are different from single-photon ones [9]. This phenomenon was originally predicted by the German theoretical physicist Maria Göppert-Mayer in 1931 in her doctoral dissertation [10]. The absorption is proportional to the square of the excitation intensity and the proportionality coefficient, called *two-photon absorption cross-section*, is measured in Göppert-Mayer unit GM, where $1\,GM = 10^{-50}\,cm^4 s/photon$ [9].

(ii) *two different fields* (*pump* and *probe*) are used in the experiment so that two photons at different frequencies, ω_{pu} and ω_{pr}, are simultaneously absorbed if the transition is approximately resonant at $\omega_{pu} + \omega_{pr}$. The beams intensities are usually comparable, more often $I_{pr} \ll I_{pu}$. In case of negligible two-photon absorption by the single fields, the *decrease in the beams transmission* is proportional to the intensity product $I_{pr}I_{pu}$ [1].

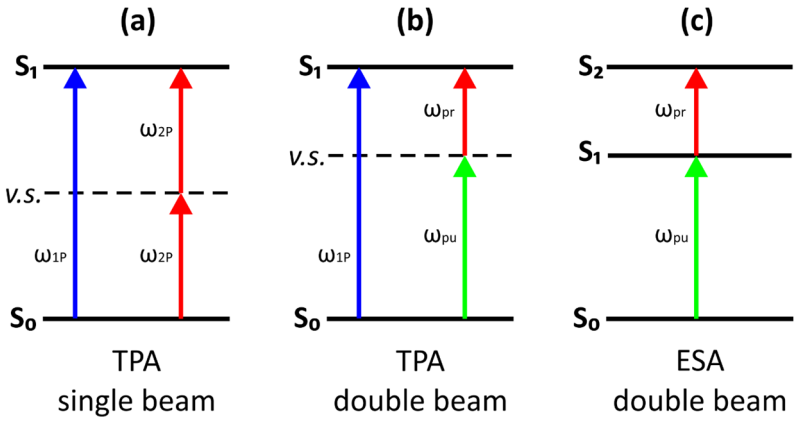

Figure 1.7 Two-photon absorption (TPA) transitions with **(a)** a single field at ω_{2P} and **(b)** two fields at ω_{pu} and ω_{pr}, compared with the linear one-photon absorption at ω_{1P}. **(c)** Excited state absorption (ESA) transition. S_0, S_1 and S_2 are electronic states, while *v.s.* is a virtual intermediate state.

Excited state absorption (ESA). Another non-linear absorption transition, shown in **Figure 1.7(c)**, involves a *real* S_1 intermediate state. A first *pump* beam (ω_{pu}) in resonance with the transition $S_0 \rightarrow S_1$ highly populates the excited state. Before the complete relaxation of the electrons to the ground state, a second *probe* beam (ω_{pr}) in resonance with the transition $S_1 \rightarrow S_2$ can be absorbed by the excited state, undergoing a *decrease in its transmission*. The change in probe transmission ΔT_{pr} can be described by the equation [11,12]

$$\Delta T_{pr} = -\int \frac{N_0 \sigma_{pu}[\sigma'_{pr} - \sigma_{pr}] I_{pu} I_{pr} exp(-\Delta t/\tau)}{\hbar \omega_{pu}} dz \qquad \textbf{(1.6)}$$

where N_0 is the molecular concentration of the ground state S_0, σ_{pr} and σ'_{pr} are the linear absorption cross sections of ground and excited state for the probe beam, respectively, Δt is the time delay between pump and probe pulses, and τ is the lifetime of the excited state. Only at $\Delta t = 0$ ΔT_{pr} has the maximum value, while, increasing Δt, ΔT_{pr} exponentially decreases according to the lifetime τ of the excited state.

Absorption saturation. Absorption saturation is an example of a *"cascaded linear process"* [6], caused by a high-intensity excitation beam in resonance with the $S_0 \rightarrow S_1$ transition. As the intensity increases, the upper level becomes more and more populated, leading to a decrease of available states and a consequent decrease of the absorption coefficient. Since the reduction of the absorption directly depends on the excitation power, the saturation process

behaves like a third order non-linearity [6]. The dependence of the measured absorption coefficient α on the intensity I is given by the formula [3]

$$\alpha = \frac{\alpha_0}{1+I/I_s} \qquad \textbf{(1.7)}$$

where α_0 is the low-intensity absorption coefficient and I_s is a parameter characteristic of the sample known as *saturation intensity*.

In addition, this population redistribution induced by intense incident beams may lead to

(i) a reduction of the absorption of another beam (*probe*) in resonance with the same transition, known as **ground state depletion (GSD)**. The *transmission increase* can be described by an equation similar to **equation 1.6** [11]

$$\Delta T_{pr} = -\int \frac{N_0 \sigma_{pu} \sigma_{pr} I_{pu} I_{pr} exp(-\Delta t/\tau)}{\hbar \omega_{pu}} dz \qquad \textbf{(1.8)}$$

where the *pump* beam is the beam that depletes the ground state. Also in this case, the strongest signal is achieved when $\Delta t = 0$, while an exponential decrease is achieved delaying the probe pulse from the pump pulse.

(ii) **stimulated emission** transitions, if the short-lived excited state is dipole coupled to the ground state and if it is interrogated with a *probe* beam in resonance with the transition $S_1 \rightarrow S_0$ [13]. As a consequence, the excited state is stimulated to emit at the same frequency of the probe. The equation describing the *transmission increase* of the probe beam under these conditions is the same as **equation 1.8**, except for the probe wavelength choice which, in this case, is selected away from the absorption peak.

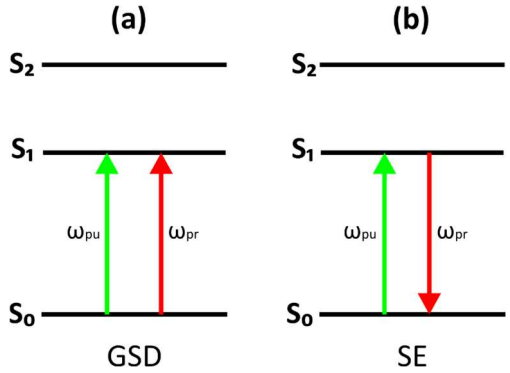

Figure 1.8 Transitions induced by absorption saturation: **(a)** ground state depletion (GSD) and **(b)** stimulated emission (SE).

1.2.2. Stimulated scattering

Signal coming from light scattering can be used to obtain useful spectroscopic information about the sample, at frequencies different from absorption and emission resonances. Spontaneous scattering processes were previously introduced in **Section 1.1.4** as linear light-

matter interactions involving a single incident beam. In the presence of sufficiently intense laser beams, the optical properties of the material are modified and these scattering processes can be strongly amplified, resulting in *stimulated scattering*. The various stimulated scattering mechanisms are classified as third-order non-linear optical processes.

In **Figure 1.6(b)**, the *Raman-type* resonant processes are described, which are based on the frequency mixing of three waves to produce a fourth one. This type of processes is responsible for the *stimulated Raman transitions*, like **coherent anti-Stokes Raman scattering (CARS)** and **stimulated Raman scattering (SRS)**. These techniques are also denoted as **coherent Raman scattering (CRS)** techniques because the vibrational motions ω_v are coherently driven by two external fields, ω_1 (called *pump* ω_p) and ω_2 (called *Stokes* ω_s, with $\omega_s < \omega_p$), tuned such as $\omega \equiv \omega_p - \omega_s = \omega_v$ in order to achieve a signal enhancement (see **Figure 1.9(a)**).

The third-order non-linear susceptibility of the interacting material can be represented as

$$\chi^{(3)}(\omega) = \chi^{(3)\ res}(\omega) + \chi^{(3)\,nres} \qquad \textbf{(1.9)}$$

$\chi^{(3)\ res}(\omega)$ is the frequency-dependent *imaginary* term describing the *resonant* effect at $\omega = \omega_v$, which can be derived as [14]

$$\chi^{(3)\ res}(\omega) = \frac{2Nc^4}{\hbar\omega_s^4}\left(\frac{\partial\sigma_{Raman}}{\partial\Omega}\right)\frac{\omega_v\,\Delta N}{\omega_v^2-\omega^2-i\Gamma\omega} \qquad \textbf{(1.10)}$$

where N is the molecular number density, $\partial\sigma_{Raman}/\partial\Omega$ is the normal Raman scattering differential cross-section, ΔN is the population difference between ground and excited state ($\Delta N = 1$ means that all the molecules exist in the ground state), and Γ is the bandwidth of the Raman line centered around ω_v. $\chi^{(3)\,nres}$ is the constant *real* term describing *non-resonant* effects generated by four wave mixing processes in all the spectrum.

Compared to spontaneous Raman scattering, CRS possesses different advantages:

(i) it provides much stronger signals, which account for its popularity in optical microscopy
(ii) it offers a more detailed control of the Raman response, allowing the probing of selected resonances by proper tuning of the input wavelengths
(iii) when using ultrashort pulses, it provides information about the temporal evolution of the Raman coherences by tuning the temporal delay of the two input pulses.

Stimulated Raman scattering (SRS). SRS was first observed in 1962 by E. J. Woodbury and W. K. Ng while introducing a nitrobenzene cell within a ruby laser cavity [15]. After that, the same effect has been observed on various physical and chemical systems, both liquid and solid.

The differences between CARS and SRS are in the number and location of intermediate levels, and in the detected signal (see **Figure 1.9Figure 1.9(a,b)**). CARS is a parametric process in which input and output photons exchange energy leaving the quantum state of the molecule unchanged, because the difference energy between pump and Stokes photons is carried away

by the anti-Stokes field, detected at the frequency $\omega_{as} = 2\omega_p - \omega_s$. CARS can also occur when there are no resonant molecules in the interaction volume, generating a *non-resonant background* ($\chi^{(3)\,nres} \neq 0$) that can limit the sensitivity and alter the spectra from what expected with the spontaneous Raman technique.

SRS is obtained when the intermediate levels are degenerate, and as a result the pump beam experiences an intensity loss ΔT_p (stimulated Raman loss, **SRL**) while the Stokes beam experiences an intensity gain ΔT_s (stimulated Raman gain, **SRG**). These intensity changes are detected. SRS is a dissipative (non-parametric) process in which the energy difference of the input beams is transferred into the molecular vibrations. SRS is free of non-resonant background ($\chi^{(3)\,nres} = 0$) and provides spectra that are nearly identical to the ones obtained with the spontaneous Raman process. Moreover, the SRS intensity is linearly dependent on the molecular concentration and it can be written as [4]

$$\Delta T_{p,s} \propto \mp N\, \sigma_{Raman}\, I_p\, I_s \qquad (1.11)$$

where N is the number of molecules in the probe volume, σ_{Raman} is the molecular Raman scattering cross-section, I_p and I_s are the pump and the Stokes incident intensities, respectively. Being a non-parametric process, SRS is governed by the imaginary part of the third-order susceptibility, which corresponds to the imaginary part of the resonant term ($\chi_I^{(3)res}$). Therefore, the SRS intensity can also be described following **equation 1.5**

$$\Delta T_{p,s} \propto \mp \chi_I^{(3)res}\, I_p\, I_s \qquad (1.12)$$

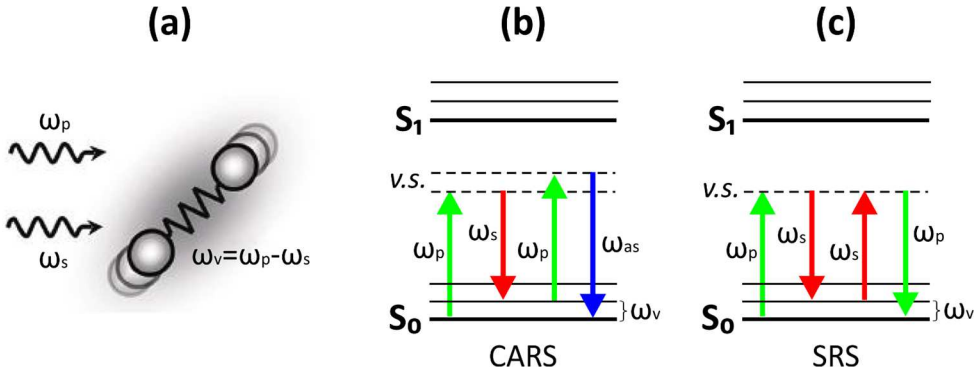

Figure 1.9 Coherent Raman scattering transitions. **(a)** Representation of the two input pump and Stokes fields, driving the molecular vibration at ω_v. Adapted from [4]. **(b)** Coherent anti-Stokes Raman scattering (CARS) transition diagram. **(c)** Stimulated Raman scattering (SRS) transition diagram. Electronic states are represented by thick solid lines, vibrational states by thin solid lines, and virtual states by dashed lines.

Saturation of the Raman scattering process. The saturation of CARS was first experimentally observed in 1981 as a spectral broadening [16], and it was attributed to the effect induced by a perturbation due to SRS which occurs simultaneously and reduces the population difference between ground and excited state (ΔN) through a pumping process

[16,17]. In principle, it can be said that, at high intensity levels, CARS and SRS are competing processes.

The rate of change of ΔN for monochromatic beams can be approximated as [16,17]

$$\frac{1}{\Delta N}\frac{\partial \Delta N}{\partial t} = -2\left(\frac{4\pi c}{\hbar \omega_S^2}\right)^2 \left(\frac{\partial \sigma_{Raman}}{\partial \Omega}\right) \frac{\Gamma}{4(\omega_v-\omega)^2+\Gamma^2}\, I_p\, I_s \equiv \frac{1}{\tau_{\Delta N}} \qquad \textbf{(1.13)}$$

The ground state depopulation is most pronounced at resonance conditions ($\omega = \omega_v$), while it rapidly decreases off-resonance. Moreover, this equation indicates that the depopulation exponentially decreases ($\propto e^{-t/\tau_{\Delta N}}$), and this is the cause of the saturation of the CRS signals.

2. Optical microscopy

The field of optical microscopy comprises a plethora of techniques which use light in order to magnify and view objects that cannot be seen with the naked eye. In particular, optical microscopy has become an indispensable tool in life science, because it provides non-invasive and versatile imaging approaches of (living) biological specimens, which are less destructive than other imaging approaches like electron microscopy.

The simplest form of an optical imaging system is the magnifying glass, which consists of a single lens made by a transparent refracting material (usually glass) that is interposed between the object and the eye. The light coming from the object is collected to form an enlarged *virtual* image, which is then projected onto the retina of the eye (**Figure 2.1**). This "*simple microscope*" achieved its highest performance with the work, in the 1670s, of the Dutch draper Antoni Philips van Leeuwenhoek, who was able to see microbes for the first time.

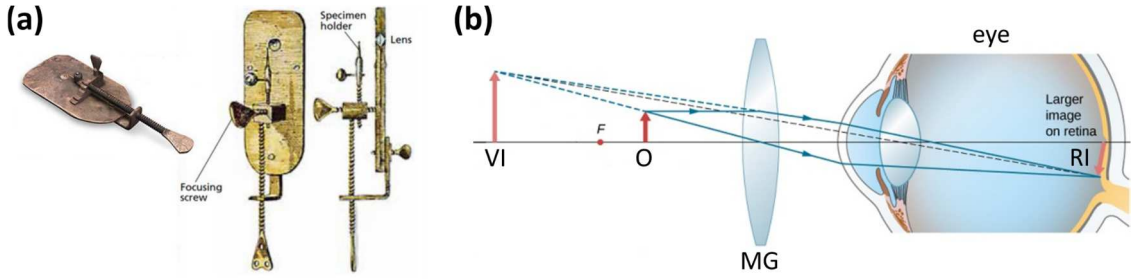

Figure 2.1 (a) Van Leeuwenhoek simple microscope (1672). **(b)** Ray diagram through a magnifying glass (MG): the object (O) is transformed in a magnified virtual image (VI) which is then projected as a real image (RI) on the retina of the eye.

More complex optical systems, known as *compound microscopes*, were developed in the 17th century thanks to the works of the Dutch spectacle-makers Hans and Zacharias Janssen, of the English natural philosopher Robert Hooke and of the Italian astronomer Galileo Galilei. In their simplest form, they consisted of two convex lenses, an *objective* closer to the object and an *eyepiece* closer to the observer's eye, aligned in series to obtain a higher two-stage magnification given by $M_{tot} = M_{obj} \times M_{eye}$.

During centuries, microscopes did not change so much their original optical architecture (see **Figure 2.2**). Innovations mainly concerned the mechanical part of the instrument, while their optical performances remained fairly poor. Starting from the first half of the 19th century, advancements in the microscope performances, and in particular in resolution, contrast, noise, sensitivity and specificity, were made possible thanks to:

(i) improvements in the optical components manufacturing, that permitted, for example, to correct for chromatic and spherical aberrations of lenses;

(ii) introduction of external adjustable and controllable illumination sources, from halogen lamps to the most recent lasers;

(iii) advancements in the detection systems, not only based on visual capturing, but also on the registration of real images by photosensitive devices (digital microscopy);

(iv) exploitation of various light-matter interactions, different from simple reflection or refraction of light, in order to increase image contrast, gain sample information and expand the applicability of the technique.

Significant developments led to various optical methods to provide contrast in live-cell imaging (phase and interference microscopy, fluorescence microscopy), techniques for dynamic imaging of live-cell cultures (time-lapse and video microscopy), optical techniques for three-dimensional (3D) imaging (confocal microscopy) and non-linear optical methods for label-free imaging (multiphoton, harmonic generation and coherent Raman microscopy).

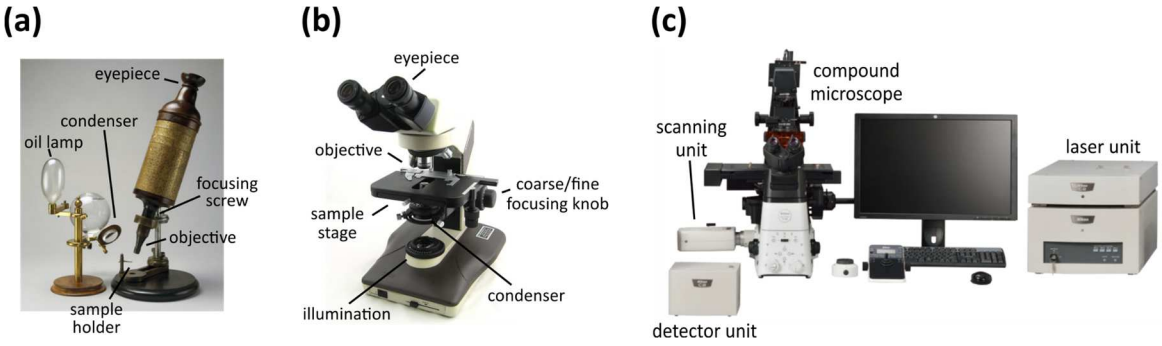

Figure 2.2 Evolution of the microscope: **(a)** Hooke microscope (1670), **(b)** modern compound microscope, **(c)** advanced microscopy platform with laser sources and digital detectors.

2.1. From fluorescence to label-free optical microscopy

The phenomenon of *fluorescence* (see **Section 1.1.5**) has been known since the 19th century as the emission of light by a substance (called *fluorophore*) that has previously absorbed electromagnetic radiation. Fluorophores can be used to specifically target molecules of interest. The development of specific dyes, of physiological and molecular probes (intrinsic and extrinsic), of genetically expressed fluorescent proteins and of quantum dots stimulated the widespread use of fluorescence in optical microscopy to achieve higher specificity in imaging biological systems. Usually, fluorophores absorb one photon in the UV-VIS spectral range, while their fluorescence emission has longer wavelengths (lower energies) because non-radiative processes contribute to the relaxation to the ground state (see **Figure 1.1**). This wavelength shift, known as *Stokes shift*, permits to easily separate the fluorescence signal from the excitation and from other background light using proper filters and dichroic mirrors, increasing in this way the image contrast. The invention of the laser in the 1960s supported the development of numerous light sources for the fluorescence microscope, which contributed to the increase in image quality. Lasers offered a high degree of spatial and temporal coherence, together with the possibility of focusing the beam in a tiny spot of very high local irradiance. The spot can then be scanned throughout the focal plane and the signal can be acquired point-by-point (*laser-scanning* microscope), differently from a *wide-field* approach where the sample is illuminated all at once and the signal is collected from all the volume (**Figure 2.3(a)**). Adding a small aperture (pinhole) in a conjugate focal plane in the detection path, out-of-focus photons are better rejected, image blurring is reduced, and higher signal-to-noise ratio (SNR) and optical sectioning capabilities are achieved (*confocal* microscope, **Figure 2.3(b)**) [18].

Fluorescence signal permits not only to collect images, but also to visualize and analyze more complex events happening in the system under study. Advanced techniques like fluorescence recovery after photobleaching (FRAP) [19], fluorescence resonance energy transfer (FRET) [20], fluorescence lifetime imaging microscopy (FLIM) [21], and fluorescence correlation spectroscopy (FCS) [22] were introduced to monitor dynamics, interactions and diffusion properties of the molecules of interest.

Despite their well-established benefits, conventional fluorescence microscopy techniques possess some drawbacks and limitations:

(i) they rely on external labeling procedures with exogenous dyes or with gene-modified endogenous labels, whose introduction may alter the functions and the physical properties of a biological molecule or structure. Moreover, the labeling approach offers limited capability of discovery because it is only applicable to known species, the label delivery may be difficult, especially under *in vivo* conditions, and labels may be too bulky.

(ii) they suffer from fluorophore photobleaching, the permanent loss of the ability to fluoresce due to photon-induced chemical damage or irreversible covalent modifications, and they may induce photodamage effects, especially if using UV exposure which is strongly absorbed by endogenous biological components. These effects can be reduced by limiting the exposure to the excitation source but at the cost of the fluorescence signal detection.

(iii) they rely on a confocal pinhole to achieve optical sectioning capabilities. The smaller the pinhole, the better the sectioning, but at the cost of image brightness and SNR.

(iv) they achieve a limited penetration depth while imaging thick specimens (like tissues), due to the use of UV-VIS excitation photons which are scattered more (see **Section 1.1.4**).

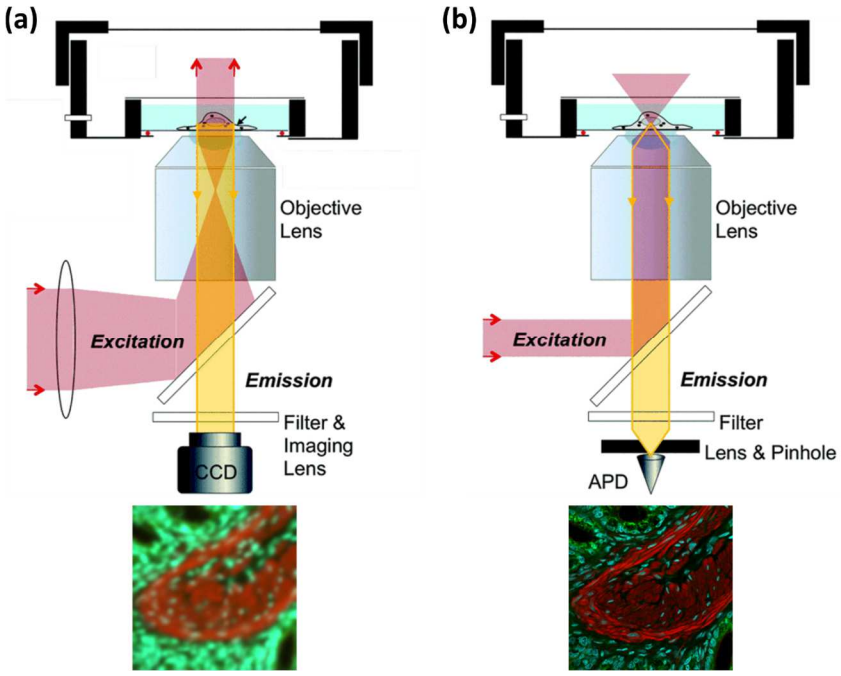

Figure 2.3 Comparison between fluorescence microscope configurations. **(a)** *Wide-field* microscope, where the whole sample is illuminated at once and the fluorescence is detected with a camera, like a CCD (charge-coupled device). **(b)** *Point-scanning* microscope, where the excitation beam (usually a laser) is focused in a small spot and scanned throughout the sample. The fluorescence signal is collected point-by-point by a single-point detector, like an APD (avalanche photodiode). Moreover, the *confocal* modality is achieved by placing a pinhole in front of the detector, in order to reject out-of-focus photons. Excitation pathway in pink, emission pathway in orange. Fluorescence images of a stained thick tissue sample obtained with the two modalities are compared (adapted from http://zeiss-campus.magnet.fsu.edu/).

As introduced in **Chapter 1**, the advent of laser sources permitted to explore novel non-linear light-matter interactions. These processes have in general less probability to occur than linear ones, thus they require higher excitation photon densities, which means higher incident powers. For this reason, it did not seem possible to use such sources in optical microscopy without damaging biological samples. The problem was solved with the development of a proper optical setup, which is based on a laser scanning microscope combined with an *ultra-short pulsed laser*. The implementation of non-linear microscopy approaches allowed to

overcome some limitations given by the conventional fluorescence techniques, and to access a wider range of functional and structural information of the specimens under study [9,23–25].

In these techniques, the detected signal is generated via the interaction, in the focus, of two or more photons with the sample, and its strength is typically proportional to I_{exc}^{n}, where I_{exc} is the excitation intensity and n is the number of interacting photons. With the introduction of NIR pulsed laser sources (indicatively between 700 and 1400 nm), techniques like two-photon excited fluorescence (TPEF), second harmonic generation (SHG), and coherent Raman scattering (CRS) microscopy have become routinely used for imaging (living) biological samples.

With TPEF microscopy, *autofluorescence* resulting from two-photon absorption of NIR radiation by endogenous biological molecules, such as coenzymes NADH and flavins found in mitochondria, or pigments like melanin, can be efficiently collected in cells and tissues without adding any exogenous fluorescent label (**Figure 2.4(a,c)**).

TPEF microscopy is usually combined with SHG microscopy, which adds complementary structural information to the system [26]. SHG is a non-linear coherent scattering process which results in photons at exactly half the incident wavelength (twice the incident frequency). It arises from non-centrosymmetric structures, like collagen fibers, myosin and microtubules (**Figure 2.4(b,c)**). Both signals have a quadratic dependence on the incident laser power.

With CRS microscopy, two beams are used to drive molecular vibrations and map the typical vibrational Raman spectra of biomolecules inside cells and tissues, providing a characteristic fingerprint of the chemical composition of the system at the molecular level (**Figure 2.4(d-f)**).

The field of non-linear microscopy includes many other techniques, and some of them will be extensively explained in **Chapter 3**.

Non-linear optical microscopy techniques permit to [9,23–25]:

(i) obtain label-free imaging, taking the contrast from intrinsic properties of the sample (autofluorescence, scattering, …), without the need of external labeling;

(ii) reduce photobleaching and photodamage, increasing the viability of biological specimens. Non-linear processes are limited to small focal volumes, where sufficient energy densities are achieved, thus damage effects are confined. Outside the focal volume, the probability of single-photon absorption and energy deposition in the sample is very low as biomolecules typically do not absorb in the IR range but at shorter wavelengths. Moreover, scattering processes do not involve absorption transitions and scattering signal is not degraded by photobleaching;

(iii) achieve intrinsic optical sectioning, thanks to the confinement of the multiphoton interaction in a small focal volume and the consequent improvement in the axial resolution. This means that the pinhole used in confocal microscopy to reject out-of-

focus photons can be removed, maximizing the signal collection and the SNR in 3D imaging;

(iv) increase the penetration depth while imaging thick samples, due to the use of longer wavelengths that are less attenuated;

(v) gain new sample information, like structural, dynamical and chemical, due to the exploitation of novel non-fluorescent-based contrast mechanisms.

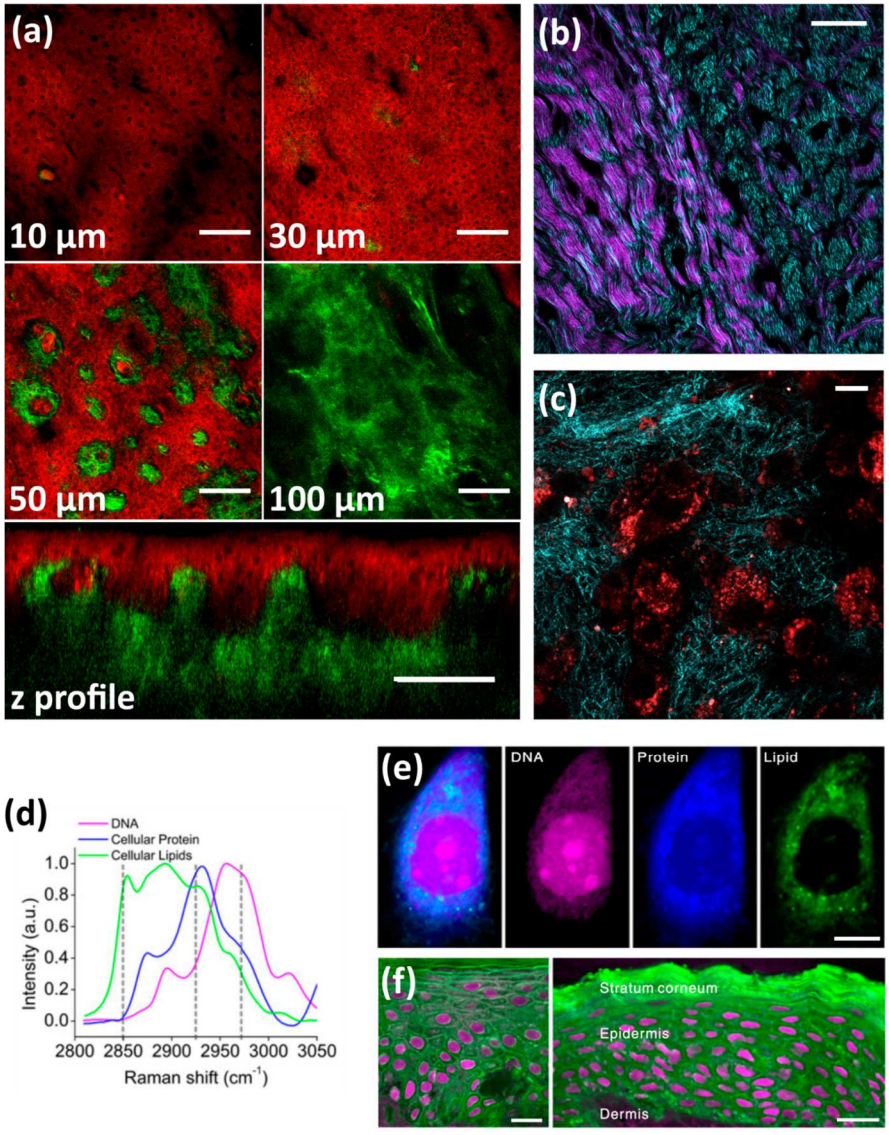

Figure 2.4 Non-linear microscopy images. **(a)** Human skin tissue imaging performed *ex vivo* under a two-photon microscope. Cells autofluorescence is excited at 800 nm and shown in red. SHG from collagen fibers is generated with 990 nm excitation and shown in green [27]. Scale bar 100 µm. **(b)** Mouse tendon under 870 nm excitation, exhibiting strong SHG signal from collagen fibers (magenta, collected in backward direction) and myosin bundles (cyan, collected in forward direction). Scale bar 50 µm. **(c)** Unstained cells (autofluorescence in red) in a collagen matrix gel (SHG in cyan). Scale bar 10 µm. **(d)** Raman spectrum of the main cellular components (DNA, protein and lipids). CRS images of **(e)** live cells and **(f)** human skin tissue are shown, highlighting the DNA in magenta, the proteins in blue and the lipids in green. Scale bar **(e)** 10 µm and **(f)** 20 µm. **(d-f)** adapted from [28].

2.2. The diffraction limit

In **Section 1.1.3**, the phenomenon of *diffraction* was briefly presented as the bend of a traveling electromagnetic wave when it encounters an obstacle or an aperture, which can be explained as an interference effect. Diffraction is at the basis of the image formation process in an optical microscope, and the cause of its limited resolving power, which does not permit to resolve details as smaller as we want.

In the optical microscope, image formation occurs through interference, at the image plane, between light waves diffracted by the sample and by the objective lens aperture. The image is conjugate with the specimen, meaning that each point in the specimen is represented by a corresponding point in the image. The image of a point source through an objective lens does not look like an infinitely small point in the image plane, but instead constructive and destructive interference produces a characteristic diffraction pattern in two dimensions. This pattern consists in a central bright spot (*Airy disk*), which contain about 84% of all the light [29], surrounded by concentric rings forming an *Airy pattern* (**Figure 2.5(a)**), named after the British astronomer Sir George Airy who first theoretically described the phenomenon [30].

The Airy disk dimension depends on the wavelength λ and on the angular aperture of the objective lens. For an infinitely distant source (as in the case of a telescope observation), the Airy disk radius r is given by

$$r = 1.22\lambda\frac{f}{D} \qquad \textbf{(2.1)}$$

where D/f is the aperture angle, f is the focal length and D is the lens diameter. In a microscope, the aperture angle of the objective lens is described by the *numerical aperture* $NA = n\sin\alpha$, where n is the refractive index of the medium between lens and sample and α is the half-angle of the cone of specimen light accepted by the objective. The Airy disk dimension can then be written as

$$r = 1.22\frac{\lambda}{2NA} \qquad \textbf{(2.2)}$$

The disk dimension decreases with decreasing wavelength and increasing numerical aperture (**Figure 2.5(b)**), but it always remains finite, pointing out that optical microscopy is a **diffraction-limited** technique.

The mathematical foundations for quantifying this concept were presented by the German physicist Ernst Abbe, who published, in 1873, the landmark paper containing the definition of the *fundamental resolution limit* described as the shortest distance d between two points that can still be distinguished with a microscope system [31]

$$d = \frac{\lambda}{2NA} \qquad \textbf{(2.3)}$$

This states that a specific detail in the sample can be resolved when the numerical aperture of the objective is large enough to capture the *zero*th order diffraction pattern (central Airy

disk) that is produced. Experimentally, this means that, for $NA = 1$ and visible wavelengths in the range 400-700 nm, the resolution limit is around 200 nm. Electron microscopes can achieve a much higher resolution than light microscopes because electrons, that are used to form the image, have a wavelength of the order of 0.005 nm.

The Abbe theory was later refined by the British scientist Lord Rayleigh, who proposed the *Rayleigh criterion* for the resolution limit (**Figure 2.5(a)**), stating that two Airy patterns are distinguishable if the center of one Airy disk falls on the first minimum of the other Airy disk, and he defined the resolution limit as [32]

$$d = 0.61\frac{\lambda}{NA} \qquad \textbf{(2.4)}$$

Experimentally, the resolution of the system is often calculated by acquiring a (3D) image of point-like (i.e., sub-resolved) radiation sources, such as fluorescent beads or quantum dots for a fluorescent microscope, and by measuring the full-width-at-half-maximum (FWHM) of the intensity profile. When looking at a point source in 3D; the Airy disk elongates in the axial direction, acquiring a typical intensity distribution called *point spread function* (PSF) (**Figure 2.5(b)**). Axial resolution is even worse than the lateral one, and it is given by the formula [29]

$$d_z = \frac{2\lambda n}{NA^2} \qquad \textbf{(2.5)}$$

With the confocal geometry and the use of a confocal pinhole in fluorescence detection, both lateral and axial resolutions are improved up to a factor $\sqrt{2}$ in the limit case of infinitely small pinhole size [29,33]

$$d_{xy} = 0.4\frac{\lambda}{NA}$$
$$d_z = 1.4\frac{\lambda n}{NA^2} \qquad \textbf{(2.6)}$$

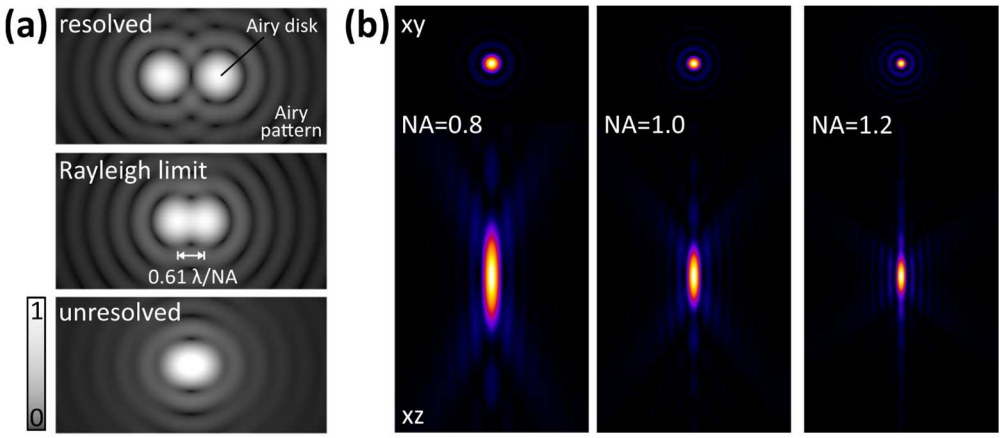

Figure 2.5 (a) Airy diffraction patterns generated by light from two points passing through a circular aperture. Points far apart (top) or meeting the Rayleigh criterion (middle) can be distinguished. Points closer than the Rayleigh criterion (bottom) are unresolved. **(b)** Lateral (xy) and axial (xz) PSFs simulated for different NAs, showing an increase in resolution with increasing NA.

In **non-linear microscopy**, the resolution is expected to be worse due to the use of longer illumination wavelengths, but this effect is compensated by a higher background signal suppression and by the spatial confinement of the multiphoton interaction [25]. Usually, the spatial resolution in non-linear microscopy is proportional to the *illumination point spread function* (IPSF) *to the power of j*, where *j* is the number of involved (equal) photons. The obtained effective PSF will have a considerably reduced excitation volume compared with that for one-photon imaging at the same NIR wavelength (**Figure 2.6**), and improved lateral and axial resolution (as FWHM of the PSF) are given by the formulae [9,29,34]

$$d_{xy} \sim \begin{cases} \frac{0.53\lambda}{\sqrt{j}NA}, & \text{for NA} \leq 0.7 \\ \frac{0.54\lambda}{\sqrt{j}NA^{0.91}}, & \text{for NA} > 0.7 \end{cases} \qquad \textbf{(2.7)}$$

$$d_z \sim \frac{0.89\lambda}{\sqrt{j}\left(n-\sqrt{n^2-NA^2}\right)}$$

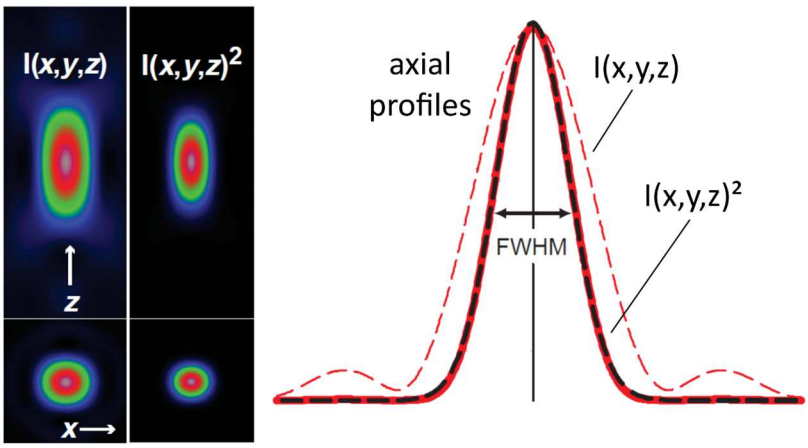

Figure 2.6 Two-photon excitation volume represented as the squared IPSF (right), and compared with the linear one (left). The axial profiles are also shown, exhibiting an increase axial resolution in the non-linear case. Adapted from [9].

2.3. Breaking the diffraction barrier

The improvement of the spatial resolution of optical microscopes has been a central challenge in the last decades, and a lot of effort has been put to circumvent this limitation, previously considered insurmountable, in order to better fit a vast number of applications in life sciences. The Abbe law still represents the fundamental limit, and, based on that formula, the only ways one can improve spatial resolution are: (i) decreasing the imaging wavelength, with the limitation that UV light interacts strongly with biological samples and leads to signal degradation due to photodamage and scattering; (ii) increasing the objective NA, which is practically limited by the lens dimensions and the available immersion media. Under ideal imaging conditions, using the most powerful objectives, lateral resolution results still limited to around 200 nm.

The introduction of confocal and non-linear optical microscopy techniques brought a slight increase in spatial resolution by suppressing the background signal [29]. Exploiting interference by two opposing high aperture lenses [35–38] or by structured illumination patterns [39], an isotropic two-fold resolution improvement down to 100 nm was demonstrated in fluorescence microscopy, but these techniques did not really "break" the diffraction barrier. As Hell wrote in [40], "breaking implies the potential of featuring an *infinitely* sharp focal spot". This concept can be achieved by introducing additional non-linearities, like the ones contained in **saturation phenomena**.

In fluorescence microscopy, taking into consideration the photophysical and spectroscopic properties of the fluorescent molecules, **reversible saturable optical transitions** between two specific molecular states can be identified and exploited

(i) to prevent the simultaneous emission of adjacent spectrally identical fluorophores by manipulating the volume that actually fluoresces, like in stimulated emission depletion (STED) microscopy [41] and in its generalized concept called reversible saturable optical fluorescence transition (RESOLFT) [42,43], discussed in **Section 2.3.1**, or

(ii) to generate high-frequency signal harmonics which give access to higher spatial frequencies in the sample, like in saturated excitation (SAX) microscopy [44], discussed in **Section 2.3.2**.

With these techniques, resolution down to tens of nanometers was achieved.

In principle, **any saturable optical process** between molecular states, not necessarily involving fluorescent transitions, is a potential candidate for breaking the diffraction limit in optical microscopy, opening the possibility to use these approaches in label-free microscopy.

2.3.1. The RESOLFT concept

The reversible saturable optical (fluorescence) transition (RESOLFT) concept is based on switching the target molecules between an *ON* state, which gives a detectable signal (e.g., fluorescence emission) and an *OFF* state, which is optically dark. In order to prevent the simultaneous signaling of adjacent identical target molecules, the volume that actually gives a detectable signal is manipulated.

First, the *OFF*→*ON* transition is achieved in a diffraction-limited focal spot, which in principle contains many sub-resolved molecules which want to be imaged as separate entities. Second, the *ON*→*OFF* transition (called *depletion*) is realized using a beam with a spatially controlled intensity distribution featuring a 'zero' in the center (i.e., with a doughnut shape). In this way, the signal of interest is switched off at the periphery of the focal spot and it can be detected only from an arbitrarily small volume at the center of the hole of the doughnut-shaped depletion beam by saturating the depletion transition. Collinearly scanning the beams, super-resolved images can be directly acquired.

The signal suppression due to the depletion beam depends exponentially on the depletion intensity [45], and this non-linear behavior is essential for breaking the diffraction barrier. The obtained resolution d results inversely proportional to the intensity of the depletion beam [42,45,46] as

$$d = \frac{\lambda}{2NA\sqrt{1+a\frac{I_{max}}{I_{sat}}}} \qquad (2.8)$$

where λ is the detected wavelength, NA is the objective numerical aperture, $a > 0$ is a parameter that takes into consideration the shape of the 'zero' of the depletion beam [45], I_{max} is the depletion beam intensity at the crest of the doughnut, and I_{sat} is the saturation intensity, a characteristic parameter of the depletion transition which scales inversely with the lifetime of the two states [40]. When the depletion is brought to **saturation** ($I_{max} \gg I_{sat}$), a narrow spatial confinement is achieved. Moreover, it can be noticed that in principle the resolution can be continuously and infinitely increased by increasing the depletion intensity, but the effective resolution enhancement is limited by the SNR and by damage effects.

The first implementation of the RESOLFT concept was achieved in 1994 in the Hell group, who introduced the stimulated emission depletion (STED) fluorescence microscopy technique [41] (see **Figure 2.7**). In this method, the *ON* state is the excited state, the *OFF* state is the ground state, the signal to be detected is the spontaneous fluorescence emission, the *OFF*→*ON* transition is the excitation via photon absorption, and the *ON*→*OFF* competing transition is stimulated emission induced by a doughnut-shaped red-shifted STED beam (see **Figure 2.7(a-d)**) Since the typical lifetime of the fluorescent states is of the order of nanoseconds, I_{sat} results to be of the order of 100 MW/cm^2 [47], and the STED beam can reach peak powers of the order of GW/cm^2 (see **Figure 2.7(e)**). Different STED developments have been proposed during the

years in order to increase the availability of the technique [48–50], like pulsed STED [51], gated STED [52], 2P-STED [53] and parallelized STED [54]. Resolution down to 20 nm was demonstrated in cellular imaging [55] (see **Figure 2.7(f)**).

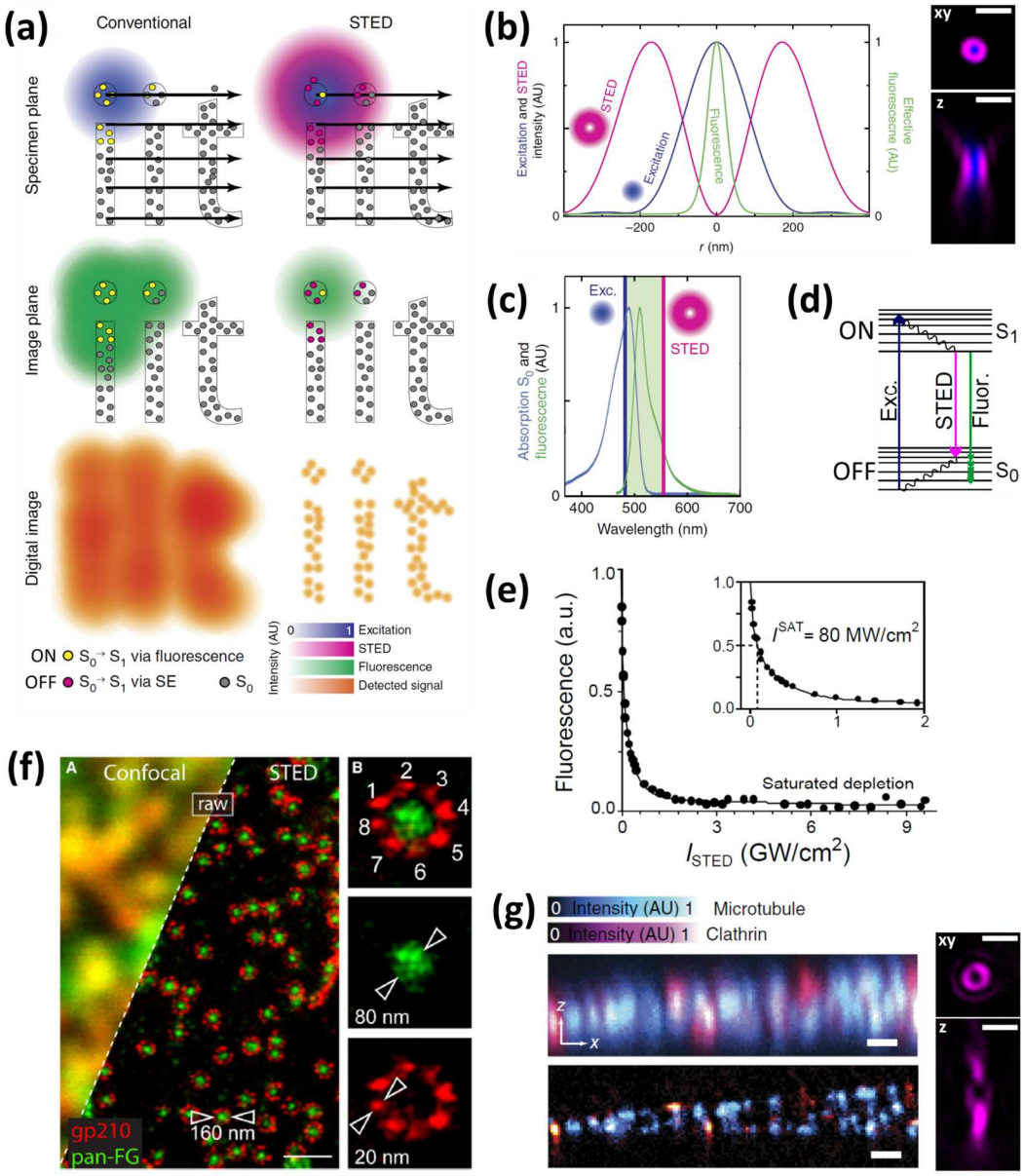

Figure 2.7 The STED principle. Adapted from [49]. **(a)** Comparison between conventional laser-scanning microscopy (left) and STED microscopy (right) image formation. **(b)** Simulated lateral beam profiles of excitation (blue) and STED (magenta) beams and their spatial superimposition to achieve fluorescence emission confinement (green). Experimental PSFs are also shown (scale bar 1 μm). **(c)** Absorption (blue) and emission (green) spectra of eGFP and wavelength choice for a STED experiment. The STED beam is red-shifted compared to the excitation, in order to avoid absorption. **(d)** Jablonski diagram indicating the OFF→ON and ON→OFF transitions in STED microscopy. **(e)** The exponential dependence of the signal suppression due to the depletion intensity. The inset graph shows the saturation intensity. **(f)** Dual-color confocal and pulsed-STED images of immunolabeled subunits in amphibian nuclear pore complex, showing 20 nm resolution [55]. **(g)** Dual-color 3D confocal (top) and STED (bottom) axial views of an immunolabeled fixed cell [49], showing axial resolution improvement. The experimental PSF of the particular STED beam used for this experiment is also shown: it is a bottle beam, providing 3D confinement of the fluorescence emission (scale bar 1 μm).

2.3.2. The SAX concept

The non-linearity of saturation was also directly exploited in the excitation-emission phenomena, and the concept of SAX (saturated excitation) was introduced for super-resolution fluorescence microscopy by Fujita et al. [44].

In conventional fluorescence microscopy, the fluorescence intensity shows a linear relationship with the applied excitation power. However, since the number of fluorescent molecules is limited in a given observation volume, when the excitation intensity is sufficiently high all the molecules will emit and the fluorescence signal will saturate (**Figure 2.8(a)**). The fluorescence signal saturation can be expressed as a sum of linear and non-linear terms, as

$$F(I_{exc}) = a_1 I_{exc} + a_2 I_{exc}^2 + a_3 I_{exc}^3 + \ \ldots = F_L(I_{exc}) + F_{NL}^{(2)}(I_{exc}) + F_{NL}^{(3)}(I_{exc}) + \ \ldots \qquad \textbf{(2.9)}$$

where $F_{NL}^{(n)}$ are the nth-order non-linear components of the signal which scales as the nth-power of the excitation intensity I_{exc}.

Usually, the saturation condition is avoided in microscopy because, apart from possible photobleaching and photodamage effects induced by high irradiances, saturation degrades the image performances deforming the effective PSF [56], which becomes wider and flatten, decreasing the resolution (see **Figure 2.8(b)**). However, since the saturation occurs first at the peak of the laser excitation, which for a Gaussian beam means at the center of the PSF, the saturated signal will arise from a smaller region and it will carry structural information on a scale that is smaller than the conventional PSF. This means that, if the saturated component is extracted, resolution can be improved in all three dimensions.

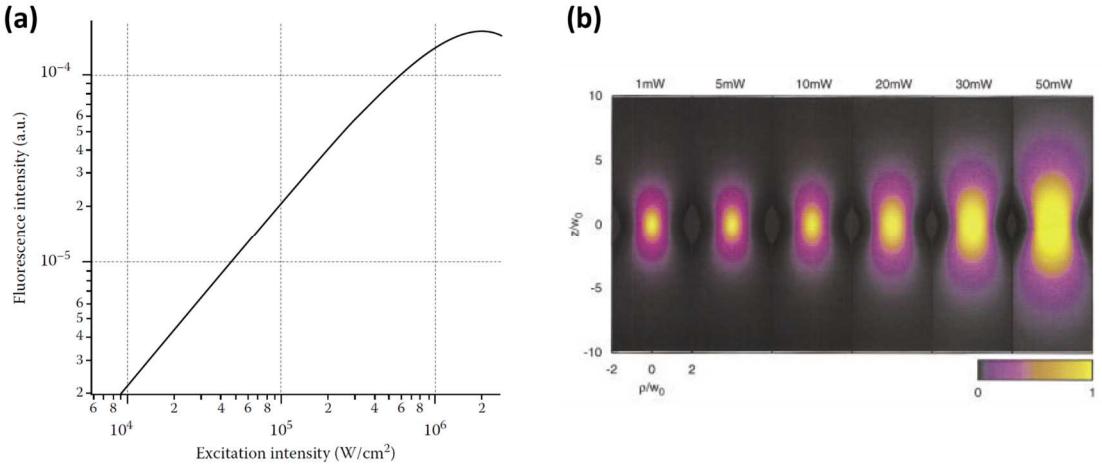

Figure 2.8 (a) Theoretical saturation response of Rhodamine 6G molecules in solution excited by 532 nm excitation. From [57]. **(b)** Calculated effective PSFs at different illumination powers, showing size increase and shape flattening. From [56].

The major limitation of this technique is due to the high excitation intensities required to saturate the signal, which may lead to photobleaching or photodamage of the sample, and may reduce the SNR of the image.

The extraction of the saturated component of the signal can be achieved (i) by temporally modulating the excitation and demodulating the signal at higher harmonics (modulated SAX), or (ii) by directly comparing the signal obtained under different degrees of saturation (differential SAX).

Modulated SAX (mSAX). This approach was first introduced in 2007 by Fujita et al. [44]. The saturated signal extraction is achieved by temporally modulating the excitation intensity at a frequency ω, and by demodulating the fluorescence intensity at the corresponding harmonic frequencies ($2\omega, 3\omega, \ldots$). Higher harmonics will appear when a non-linearity is present in the signal, for example when saturation effects occur at high excitation intensities, prominently in the center of the focal spot (**Figure 2.9(a)**). Each harmonic of the modulation frequency will have a corresponding increase in the order of the nonlinear response: the nth harmonic will have an nth-order non-linear response (**Figure 2.9(b)**). The demodulated harmonic signals can be used to form an image with higher spatial resolution.

Starting from **equation 2.9** and considering the modulated excitation as $I_{ex}(\omega) \propto \frac{1+\cos\omega t}{2}$, the fluorescence signal $F(\omega)$ can be written as

$$F(\omega) = F_L(\omega) + F_{NL}^{(2)}(\omega) + F_{NL}^{(3)}(\omega) + \ \ldots \tag{2.10}$$

$$\propto a_1 \frac{1+\cos\omega t}{2} + a_2 \left(\frac{1+\cos\omega t}{2}\right)^2 + a_3 \left(\frac{1+\cos\omega t}{2}\right)^3 + \ \ldots$$

$$= a_1 \left(\frac{1}{2} + \frac{1}{2}\cos\omega t\right) + a_2 \left(\frac{3}{8} + \frac{1}{2}\cos\omega t + \mathbf{\frac{1}{8}\cos 2\omega t}\right) +$$

$$+ a_3 \left(\frac{5}{16} + \frac{15}{32}\cos\omega t + \frac{3}{16}\cos 2\omega t + \mathbf{\frac{1}{32}\cos 3\omega t}\right) + \ \ldots$$

where the appearance of higher harmonics in the signal is explicitly derived. The second-order harmonics (2ω) accounts for $\frac{1}{8}$th of the total second-order non-linearity ($F_{NL}^{(2)}(\omega)$), while the third-order harmonics (3ω) accounts for $\frac{1}{32}$nd of the third order non-linearity ($F_{NL}^{(3)}(\omega)$). The higher the extracted harmonics, the higher the achievable resolution but also the lower the extracted signal intensity and the obtained image SNR (**Figure 2.9(c)**).

Practically, a SAX microscope can be realized with a simple modification in a conventional confocal microscope, which consists in introducing an intensity modulator (like an acousto-optic modulator (AOM)) in the excitation path and a lock-in amplifier (LIA) for the analysis of the harmonics components of the detected signal. A 3D spatial resolution improvement of this technique was demonstrated in biological samples [58–60] (**Figure 2.9(d-e)**).

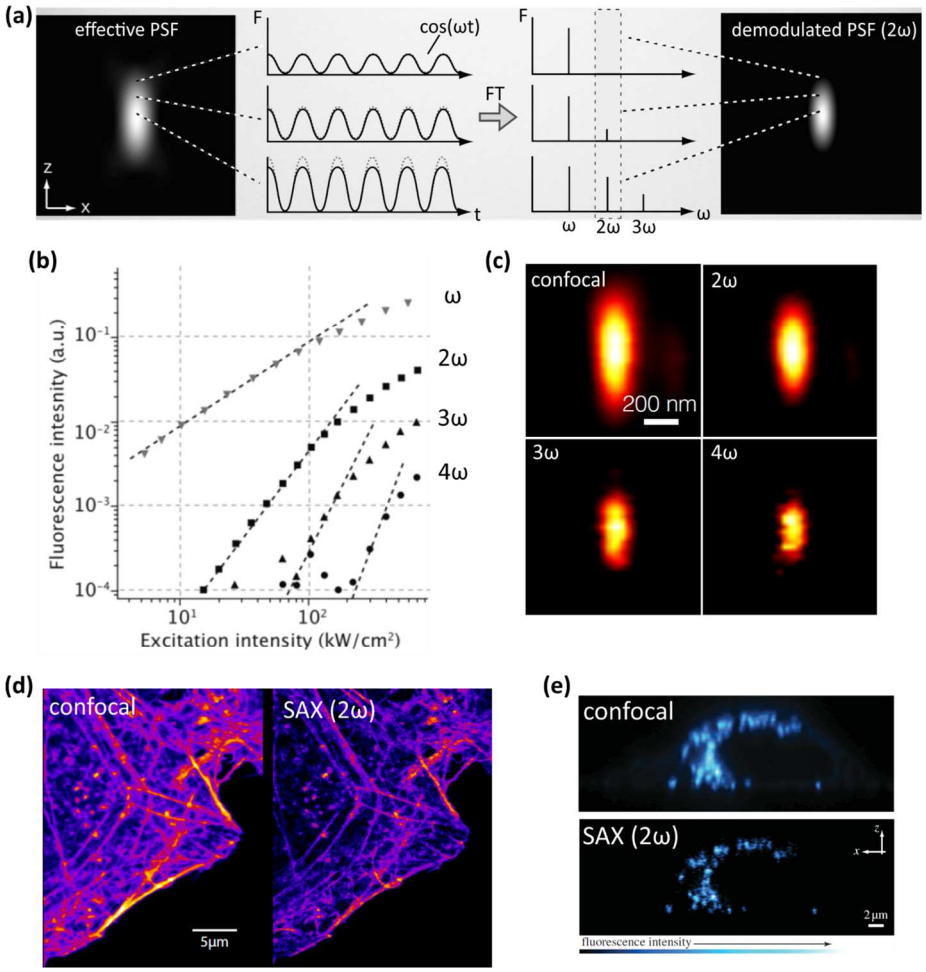

Figure 2.9 (a) Principle of mSAX. The modulated excitation generates a modulated fluorescence emission (F, solid line), whose modulation deviates from the excitation profile (dashed line) in the center of the PSF due to saturation phenomena. Fourier transform (FT) highlights the frequency components of the signal. The demodulated PSF is obtained extracting the second harmonic, which is predominant in the center leading to a smaller PSF. Adapted from [59]. **(b)** Experimentally measured relationship between demodulated fluorescence and excitation intensity (modulated at frequency $\omega = 10\ kHz$) obtained with fluorescent nanodiamonds [61]. **(c)** Demodulated images of a single nanodiamond, showing a decrease in SNR with increasing order of demodulation. Adapted from [61]. **(d-e)** Confocal and mSAX images of **(d)** microtubules stained with Atto488 [58] and **(e)** Golgi apparatus in Hela cell expressing EGFP [59], showing improved resolution both in lateral and axial directions.

Differential SAX (dSAX). An improvement in the detection efficiency of the non-linear fluorescence signal was achieved applying a differential technique, in which signals obtained at different saturation levels are compared. This method was proposed by Humpolíčková et al. [62], and it was recently applied to confocal [63,64] and two-photon microscopy [63,65] obtaining super-resolution imaging capabilities.

The differential method is sketched in **Figure 2.10(a)**. Given two signals F_1 and F_2, measured at two different excitation intensities I_1 and I_2 (with $I_2 > I_1$), the second-order non-linear component $F_{NL}^{(2)}(I_2)$ can be derived as

$$F_{NL}^{(2)}(I_2) = F_L(I_2) - F_2(I_2) = \left(\frac{I_2}{I_1}\right) F_1(I_1) - F_2(I_2) \qquad \textbf{(2.11)}$$

With a higher degree of saturation, the third-order non-linearity $F_{NL}^{(3)}(I_3)$ can be derived using three fluorescence signals obtained at three different excitation intensities $I_3 > I_2 > I_1$ [64]. Compared to the conventional mSAX method, the dSAX approach increases up to 8 and 32 times the detection efficiency of the second- and third-order non-linearities, respectively, increasing the SNR also in cells and tissue imaging (**Figure 2.10(b-c)**) [64].

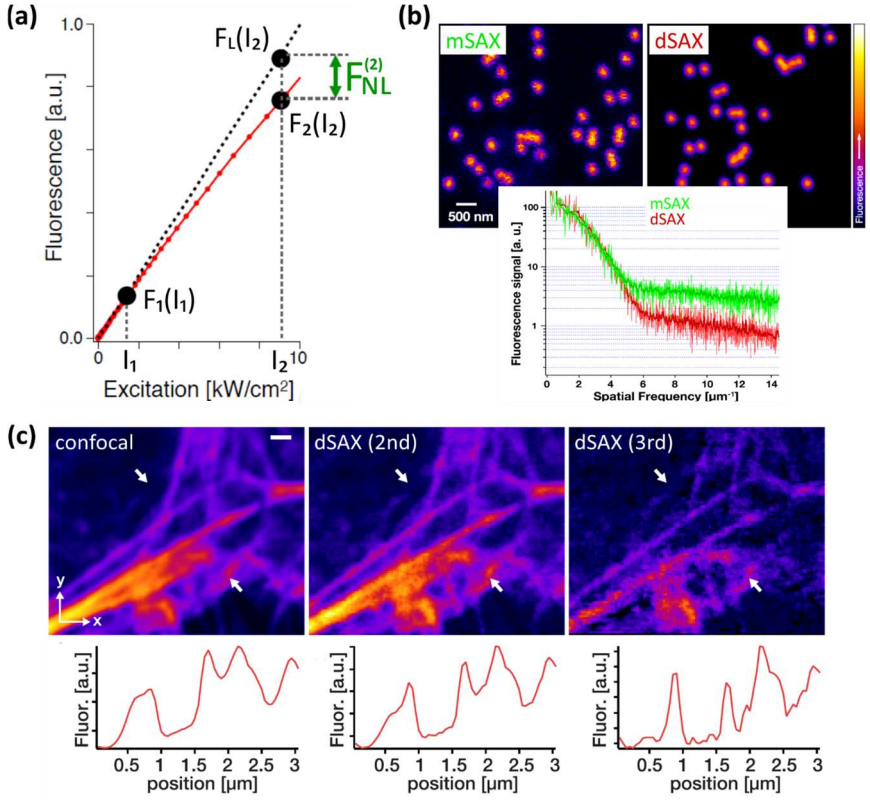

Figure 2.10 (a) Principle of dSAX. **(b)** Fluorescent beads images obtained with mSAX (left) and dSAX (right) extracting the second-order non-linearity. The Fourier transform of both signals are presented, and the dSAX approach exhibits a smaller noise level at high frequencies, correspondent to an almost 3-fold SNR improvement compared to the mSAX approach. Adapted from [64]. **(c)** Fluorescent images of actin filaments stained with Atto Rho6G in fixed Hela cells. A higher level of details is obtained with the dSAX approach at different orders. Scale bar 500 nm [64].

2.3.3. Super-resolution in label-free optical microscopy

Over the years, super-resolution approaches acquired an important and well-defined role in fluorescence microscopy, and they are responsible for many advances in life science research. On the contrary, the improvement of spatial resolution in non-linear label-free microscopy techniques has been more challenging, since the typical super-resolution strategies - based on the photophysical properties of fluorescent labels - are not directly applicable.

The use of optically transparent microspheres deposited on the specimen was proposed [66] and it was demonstrated to break the diffraction limit in reflection and in transmission white light optical microscopy [67,68], and in SHG imaging [69].

Differential approaches based on the intensity difference between two acquired images, a conventional one obtained with a Gaussian beam and one obtained with a doughnut-shaped beam giving a negative contrast (cf. [70] for the fluorescence application), were applied to reflection, SHG [71], pump-probe [72–74] and CARS [75,76] microscopy.

Structured illumination was successfully applied to Raman [77] and pump-probe [78,79] microscopy, providing up to 2-fold resolution enhancement in tissues and in nanomaterial imaging, without the use of fluorescence contrast.

The non-linearity of **saturation** was also exploited for other saturable optical transitions involved in label-free microscopy. Approaches based on the fluorescence STED architecture were theoretically and experimentally proposed for non-linear vibrational imaging [80–84] and transient absorption imaging [85,86], after identifying proper competing transitions to be saturated with an additional doughnut-shaped beam and to be effectively used to switch off the signal of interest at the periphery of the focal spot. The saturation of non-fluorescent-based interactions was also used to extract the non-linearity from the center of the focal spot, shrinking the effective PSF in a SAX-like way. This last approach was applied to CARS vibrational imaging of nanodiamonds [87], to plasmonic scattering from gold nanospheres [88], and to photoacoustic [89] and photothermal [90] microscopy.

The application of these strategies to label-free techniques is paving the way for a widespread availability of super-resolution label-free techniques in *in vivo* studies, circumventing bleaching and toxicity of dyes, and for monitoring nanomaterials and nano-optoelectronic systems.

This thesis will **explore saturation-based super-resolution approaches in non-fluorescence-based vibrational and non-linear absorption microscopy**, both theoretically (**Chapter 3**) and experimentally (**Chapter 4** and **5**).

3. Pump-probe microscopy

Among **non-linear** optical approaches, pump-probe methods were first introduced in *time-resolved spectroscopy* to resolve and monitor chemical and atomic ultrafast processes, which occur on a picosecond (or lower) timescale, much faster than the typical bandwidth of conventional detectors and electronics. Briefly, these methods involve the use of two illumination pulses. A first high-intensity *pump pulse* is used to perturb the system from equilibrium, while a second weak *probe pulse* is used to measure the photoinduced change by monitoring the probe transmission (or reflection) variations as a function of the time delay between pump and probe pulses (kinetic measurement) and/or of the probe wavelength (spectral measurement). In this way, the temporal resolution becomes dependent not on the detector speed, but on the temporal width of pump and probe pulses.

The pioneer work in this field is assigned to the British chemist George Porter, who, together with his professor at Cambridge University Ronald G. W. Norrish and with the German biophysical chemist Manfred Eigen, obtained the Nobel Prize in Chemistry in 1967 for the "studies of extremely fast chemical reactions, effected by disturbing the equilibrium by means of very short pulses of energy".

Porter's early experiments led to the development of *flash photolysis* spectroscopic techniques for monitoring photochemical reactions using flash lamps with pulses of the order of milliseconds [91]. After the laser development in the 1960s, this apparatus was equipped with nanosecond pulsed lasers able to study the absorption of excited singlet states [92,93].

The rapid development of ultrafast laser sources over the past two decades, towards shorter pulses and broader spectra, has driven advances in the field of ultrafast pump-probe spectroscopy, given access to instrumentation capable of monitoring events on a sub-100 fs timescale and on a spectrum from deep UV to mid-IR. These measurements have become of routinely use for the study of the relaxation pathways of radiative, non-radiative, and vibrational excited states, and for the optical characterization of a variety of materials, molecules, and biopolymers [34,94–98].

Moreover, the ultrafast pump-probe spectroscopy technique can be inserted in a non-linear microscopy platform [9,23–25] with a proper optical detection scheme in order to obtain not only temporal and spectral information, but also spatial maps of the ultrafast phenomena under study. Properly tuning pump and probe wavelengths, molecular specificity can be achieved, and, in this way, a wide range of dynamical properties can be provided on a microscopic scale with all the advantages of the most common non-linear microscopy techniques, as listed in **Section 2.1**.

Two types of non-linear optical interactions, already introduced in **Section 1.2**, can be exploited with a pump-probe approach to provide novel contrast mechanisms for label-free sample imaging:

(i) *non-linear absorption* (**Section 1.2.1**), used to study transient absorption phenomena and electronic kinetics, which is the contrast mechanism in **transient absorption microscopy (TAM)** (that will be presented in **Section 3.3**);

(ii) *stimulated Raman scattering* (**Section 1.2.2**), used to study vibrational kinetics, which is the contrast mechanism in **stimulated Raman scattering (SRS) microscopy** (that will be presented in **Section 3.4**).

3.1. General optical setup

A typical **pump-probe microscope** setup is shown in **Figure 3.1(a)**. It is based on a non-linear laser-scanning microscopy platform [9,23–25], where ultrashort pulsed laser beams with a proper spatial and temporal overlap are used in order to achieve highly sensitive non-linear imaging and, moreover, in order to follow ultrafast processes with sub-picosecond temporal resolution.

Pump and probe beams may be generated by two different ultrashort (pico- or femtosecond) pulsed laser sources synchronized with each other in order to have a precise control on the timing of the two pulse trains. More typically, the two beams come from the same laser source. If shorter pulses are needed, a mode-locked Ti:sapphire, tunable in the NIR wavelength range, with a pulse repetition frequency around 80 MHz and a pulse width of hundreds of femtoseconds, is typically used. High–repetition rate (around 76 MHz) picosecond pulsed lasers are also employed. The single laser output can be split into two beams, and one of them be frequency doubled in a non-linear beta barium borate (BBO) crystal in order to obtain a different wavelength in the visible range, at exactly half the initial value. A different approach consists of using the laser output to synchronously pump an optical parametric oscillator (OPO), a coherent light source based on the optical gain from parametric amplification in a non-linear crystal. OPOs are more versatile because their synchronized outputs can be tuned over a wide wavelength range, reaching wavelengths that cannot be provided by conventional lasers. Compared to the direct frequency doubling which always provides two wavelengths one half of the other, with the OPO different pump/probe wavelengths combinations may be exploited, also with the possibility to work only with NIR radiation.

The intensity of the beams may be controlled through variable neutral density filters or through a combination of half-wave plate and linear polarizer.

The temporal delay between pump and probe pulses is finely adjusted through a delay line (DL), usually made by a mechanical translational stage and placed in one of the two optical paths, in order to follow the dynamics of the interaction. Precision and range of the delay line need to be chosen in accordance to the time scale of the process of interest. The final system's temporal resolution is determined by pump and probe pulse widths, and by the spatial resolution of the delay line.

The pump-probe signal is recorded as the change in transmission (or in reflection) ΔT of the probe beam (usually) due to the perturbation caused by the pump interaction with the sample. Transmission experiments are mostly appropriate when dealing with highly transparent samples, while reflection detection is preferable with highly scattering specimens and in deep tissue imaging. The probe beam is chromatically separated from the pump beam using

appropriate filters (F) in front of the detector (DET), usually a photodiode. Since the beam intensity variations ΔT are usually very small, of the order of <1% of the total signal [99], a higher detection sensitivity is required to extract this signal from the background. This can be achieved introducing a high frequency modulation scheme, where the pump intensity is modulated at a high frequency (typically > 1 MHz [100]) and the detected probe is demodulated by a lock-in amplifier (LIA) to extract its modulation amplitude at the same frequency. Such high frequency modulation is not achievable with mechanical choppers, but acousto- or electro-optic modulators (AOM, EOM) need to be used in the pump optical path. With this approach, the low-frequency *1/f* laser intensity noise is circumvented and shot-noise-limited detection sensitivity is achieved (**Figure 3.1(b)**). Detection sensitivity down to $\Delta T/T = 10^{-7}$ (where T is the total detected probe intensity) was reported with such high-frequency modulation scheme, higher than the typical 10^{-4} value obtained with kHz modulation [101]. The modulation scheme is sketched in **Figure 3.1(c)**, where pump and probe beam behavior before and after interacting with the sample is presented. Depending on the type of interaction (TPA, ESA; GSD; SE, SRG), the probe beam undergoes a gain or a loss in transmission, equivalent to an in-phase or an anti-phase (180° out of phase) pump-probe signal, respectively.

After modulation and temporal adjustment, pump and probe beams are spatially overlapped with a dichroic mirror (DM) and collinearly focused onto a common focal spot in the sample through a high numerical aperture objective (O). Due to chromatic aberrations, pump and probe foci at the sample plane may differ. Adding two relay lenses with regulating distance in one of the two optical paths may help in adjusting the input divergence of the beam in the objective to match the other focus. In alternative, the focusing of the probe may be optimized, while the pump provides a larger uniform excitation volume of the locally probed area [102]. The focal spots are then raster-scanned throughout the sample in order to collect the pump-probe signal pixel by pixel. 3D imaging can be achieved with an axial piezo-stage with nanometer resolution.

The image acquisition speed is limited by the LIA time constant because the pixel dwell time has to be at least twice its value [103].

The dual-wavelength laser-scanning setup is the most common for pump-probe microscopy, but other variations have been proposed [101]. Single-wavelength pump-probe microscopy can be achieved, discriminating the probe beam in polarization or by a dual-frequency modulation. The latter approach consists in modulating both pump and probe beams at two different frequencies and detecting the sum- and difference-frequency components resulting from the non-linear mixing of the input frequencies. Moreover, an ultrafast optical widefield microscope was proposed [104], based on a 2D smart pixel array detector capable of acquiring images with high sensitivity, femtosecond time resolution, and sub-micrometer spatial resolution.

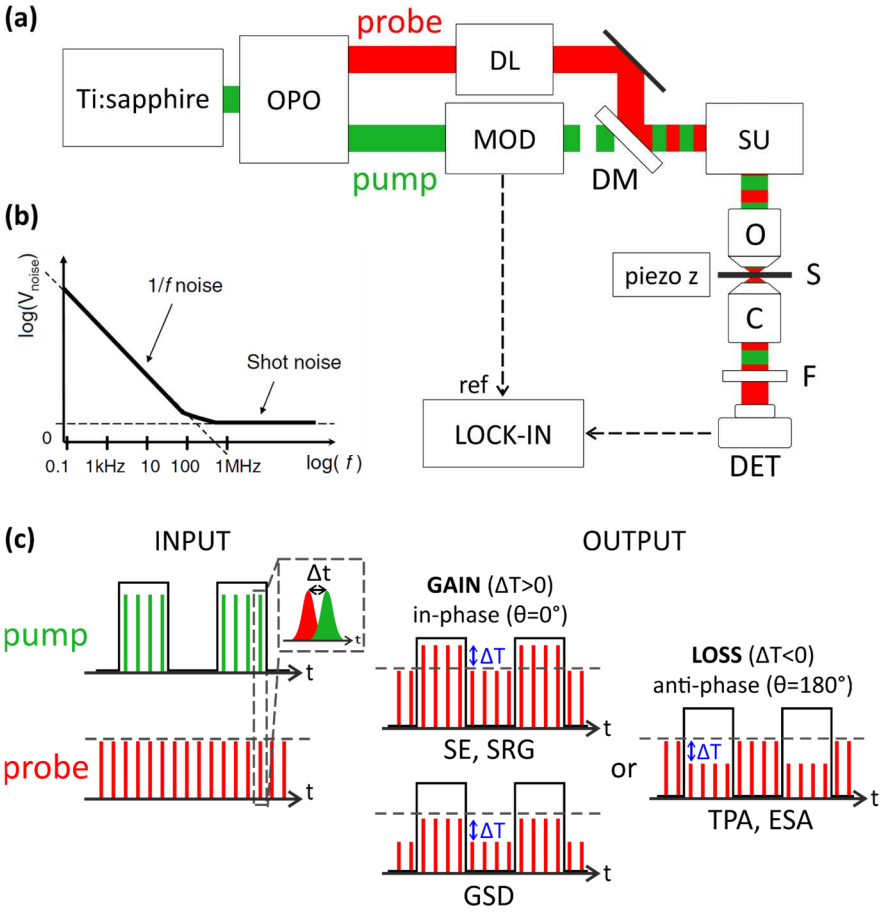

Figure 3.1 (a) Example of a two-beam laser-scanning pump-probe microscope setup. OPO: optical parametric oscillator, MOD: intensity modulator, DL: delay line, DM: dichroic mirror, SU: scanning unit, O: objective, S: sample, C: condenser, F: filter, DET: detector, ref: reference. The pump beam is shown in green while the probe beam in red. **(b)** Noise spectrum of a typical laser source as a function of frequency. In the low-frequency range (from DC to kHz), the noise follows the *1/f* behavior. In the higher-frequency range (> 1 MHz), the noise approaches the shot noise plateau [100]. **(c)** Temporal modulation behavior of input and output pulse trains before and after interacting with the sample. Depending on the light–molecule interaction, the probe beam can undergo either a relative gain (SE, SRG, GSD) or a loss (TPA, ESA) in its output intensity (ΔT), exhibiting in-phase and anti-phase modulation, respectively. The pump temporal modulation is shown as a black square wave. The input probe intensity is marked by a dashed grey line. The tunable temporal delay (Δt) of input pulses is shown in the inset graph.

3.2. Pump-probe signal information

The pump-probe signal ΔT can be extracted from the signal with a lock-in amplifier and its amplitude $R = |\Delta T|$ can be retrieved. With a more advanced two-phase lock-in amplifier also the phase difference θ of the demodulated signal with respect to the reference pump modulation can be recovered. Two outputs are obtained: $X = R\,cos\theta$ (in-phase component) and $Y = R\,sin\theta$ (quadrature component), which represent the signal as a vector relative to the lock-in reference oscillator. The amplitude can be calculated as $R = \sqrt{X^2 + Y^2}$ and the phase as $tan\theta = Y/X$.

Depending on the type of interaction, two situations may occur (see **Figure 3.1(c)**). The probe beam can experience a gain in its transmission (or reflection), equivalent to an in-phase pump-probe signal with $\Delta T > 0, \theta = 0°, X = R, Y = 0$. This is the case of ground state depletion (GSD) and stimulated emission (SE) non-linear absorption phenomena, and of stimulated Raman gain (SRG) in coherent Raman scattering. The probe beam can also experience a loss, equivalent to an anti-phase pump-probe signal with $\Delta T < 0, \theta = 180°, X = -R, Y = 0$. This is the case of two-photon absorption (TPA) and excited state absorption (ESA). This means that the type of interaction can be distinguished by looking at the phase of the signal or at the sign of the X component.

Varying the delay between pump and probe pulses (Δt in **Figure 3.1(c)**), the pump-probe signal intensity will vary according to the (electronic or vibrational) excited state relaxation dynamics of the involved species. The obtained time-resolved spectra will feature a maximum pump-probe signal when pump and probe pulses are overlapped, and an exponential decrease with increasing delay. The extrapolation of a single or multiple decay constants increases the molecular specificity of the technique, and may help in the discrimination of different sample components. The time traces can be analyzed in the time domain, performing multi-exponential fitting to derive the characteristic decay constants. Alternatively, time-resolved spectra can be analyzed in the frequency domain with the phasor analysis, first introduced for fluorescence lifetime imaging [105], which provides an intuitive graphical view of the lifetimes without any *a priori* assumption. This method permits also to avoid the fitting procedure which typically requires high signal-to-noise ratios for a reliable separation of the different components.

3.3. Transient absorption microscopy (TAM)

Transient absorption microscopy (TAM) is a pump-probe technique based on the detection of probe absorption changes induced by non-linear absorption processes. Non-fluorescence-based contrast from highly absorbing chromophores can be achieved. Absorption-based measurements are advantageous because they permit to investigate non-emissive and dark states, broadening the range of available targets and increasing the chemical specificity, and because, compared to scattering techniques, they are less dependent on the particle size and can be used to study smaller structures [11,106].

In this approach, the pump beam should have a higher intensity than the probe one, because it needs to be absorbed inducing a measurable change in the carrier population, while the probe should directly monitor this perturbation, without any additional effect and avoiding multiphoton processes during the probing. In this way, the pump-probe signal will exhibit a "weak" non-linearity and its intensity will result proportional to the product of pump and probe intensities, I_{pu} and I_{pr} respectively, and to the analyte concentration c [100,101]

$$|\Delta T| \propto c\, I_{pu}\, I_{pr} \qquad (3.1)$$

The overall quadratic dependence on the incident intensity marks the non-linearity of TAM, while the linear concentration dependence permits quantification.

The main non-linear absorption interactions were presented in **Section 1.2.1** and their transition diagrams are sketched in **Figure 1.7** and **Figure 1.8**. In **Figure 3.1(c)** and in **Section 3.2** it was presented how these interactions produce signals with opposite phase. Varying the delay between pump and probe pulses, the excited state relaxation dynamics can be followed, providing additional molecular specificity. Typical time traces for the different non-linear absorption processes are shown in **Figure 3.2**. As expected, GSD exhibits a signal that is opposite in sign compared to TPA and ESA. Moreover, TPA and ESA processes can be easily distinguished by looking at their temporal behavior, which indicates that TPA is an instantaneous process exhibiting a symmetric cross-correlation trace, while ESA shows an instantaneous rise followed by a decay reflecting the characteristic lifetime of the excited state.

The first pump-probe microscope was realized by Dong et al. in the 1990s to measure the fluorescence lifetime through SE detection [107,108]. Their approach relied on the use of two ultrafast pulsed lasers characterized by slightly different repetition rates and a consequent variable delay between their pulses. In this way, the probe pulse, tuned to induce stimulated emission in the fluorophore, was repeatedly sampling the excited population at different delays, providing dynamic information with superior spatial and temporal resolution without any amplitude modulation and delay line. In 2007, the Warren group proposed the first pump-probe microscope based on a high-frequency modulation scheme to detect TPA- and ESA-based signals from melanins in cells [109]. Since then, transient absorption microscopy has

started to be explored more in different research fields, from *material* to *biological* till *art* sciences.

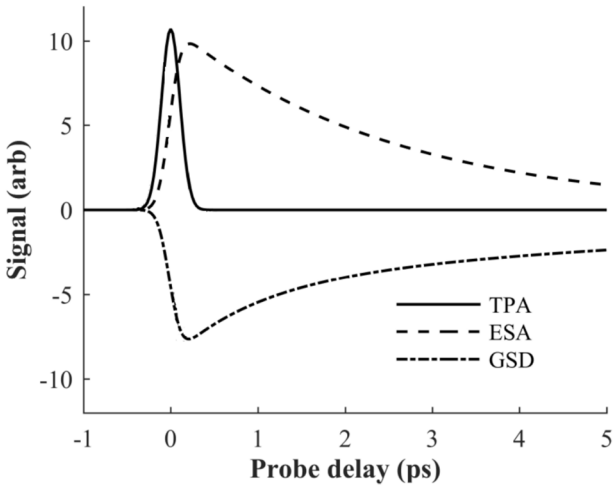

Figure 3.2 Typical time traces (signal ΔT as a function of probe delay Δt) for various non-linear interactions: two-photon absorption (TPA), excited-state absorption (ESA), and ground state depletion (GSD) [101].

Because of its non-fluorescent-based contrast, its high single-particle sensitivity and its high temporal resolution, pump-probe microscopy is extensively used in imaging and characterizing the carrier dynamics of metallic and semiconducting nanostructures for studying their optoelectronic properties [34,106,110–120]. The Cheng group studied the properties of single-walled carbon nanotubes (SWNTs), and it was able to distinguish semiconducting from metallic SWNTs looking at the phase of the pump-probe signal [119]: semiconducting SWNTs exhibit an in-phase signal due to an SE transition, while metallic ones show an anti-phase signal which corresponds to an ESA interaction. Moreover, pump-probe techniques have acquired importance in mapping weakly or non-fluorescent nanostructures - used as biorthogonal labels and for biomedical applications - in living cells and tissues [121–125]. Tong et al. [121] monitored the cellular uptake and the circulation of functionalized SWNTs in cells and tissues with high speed and submicrometer resolution. Chen et al. [122,123] studied the internalization of raw nanodiamonds and of gold nanorods in living cells with ESA microscopy. Zhang et al. [124] succeeded in colocalizing molybdenum disulfide (MoS_2) nanosheets inside lipid-rich cellular organelles with a dual-modal transient absorption/SRS microscope, studying the uptake and the photocarrier dynamics. Liu et al. [125] proposed an approach to quantify mRNA in cells and tissues at single copy sensitivity by utilizing gold nanoparticles as orthogonal probes with the transient absorption imaging modality. Further studies in material science and nanostructures characterization by pump-probe microscopy can be found in relevant reviews [34,106].

Among nanomaterials, graphene started to be intensively studied - after its discovery and its first successful isolation in 2004 [126] - for the development of novel electronic and

optoelectronic devices [127]. Graphene possesses a large third-order susceptibility, only weakly dependent on the wavelength in the NIR frequency range [128], thus it results to be an ideal target for pump-probe studies. The carrier dynamics was extensively explored with transient absorption spectroscopy in different configurations of this material, like few-layer epitaxial graphene [129], single- and multi-layer exfoliated graphene [130–132], single-layer graphene grown via chemical vapor deposition (CVD) [133], graphene suspensions [132,134], and graphene oxide [135]. The interplay between local structure and carrier dynamics was significantly explored using pump-probe approaches. In 2010, Huang et al. [136] first obtained pump-probe microscopy imaging of multi-layer epitaxial graphene grown on a silicon substrate, and showed the linear dependence of the pump-probe signal intensity on the pump power and on the number of layers. After that, many other works reported the use of pump-probe microscopy for rapid and highly-sensitive imaging of graphene, achieving the mapping of the local excited state dynamics, the characterization of nanodefects towards a real-time non-destructive approach for manufacturing applications, and the real-time quantitative imaging of graphene oxide *in vitro* and in circulating blood [86,137–141].

Transient absorption microscopy also started to be used in biological research for imaging of highly absorbing chromophores which, due to their fast non-radiative relaxation, do not produce any detectable spontaneous fluorescence. Min et al. [142] employed SE microscopy to visualize chromoproteins and hemoglobin, and to map transdermal drug distribution, extending the fundamental depth limit of two-photon microscopy [143]. SE microscopy was also used, as in its first implementation in 1995 [107], for fluorescence lifetime imaging of selected fluorophore [144,145], taking advantage of signal and SNR enhancement [146]. Eumelanin and pheomelanin were also studied and differentiated using their strong transient absorption signals [109], and this contrast was implemented for skin cancer diagnosis both *ex vivo* an *in vivo* [147,148]. Another strong endogenous absorber is hemoglobin, which offers an ESA-type contrast in imaging microvasculature [12] and red blood cells flow [149,150], and its excited state lifetime is a useful indicator of the oxygenation level [12].

Apart from biological pigments studies, pump-probe microscopy was also employed in the identification of historical art pigments and pigment mixtures, in the study of their 3D layer structure and of the method of application [151,152].

3.3.1. Super-resolution approaches in TAM

As introduced in **Section 2.2,** in non-linear microscopy the spatial resolution is proportional to the illumination point spread function (IPSF) elevated to the number of involved photons, getting a considerably reduced excitation volume. In particular, in pump-probe microscopy the spatial resolution is related to the product of the IPSFs of pump and probe beams. In the condition of pump and probe processes involving one-photon transitions, a resolution

improvement of $\sqrt{2}$ is expected compared to the resolution achieved by linear optical microscopy at the same wavelengths [34,107]. This improvement is comparable to the one obtained in confocal fluorescence microscopy [33].

As briefly introduced in **Section 2.3.3**, in recent years some super-resolution strategies were proposed and also demonstrated for label-free transient absorption microscopy.

Massaro et al. [78] developed a structured pump-probe microscope (SPPM) based on a spatially modulated pump field and a focused diffraction-limited probe field, and they used it to characterize the free carrier dynamics of silicon nanowires with ~114 nm sub-diffraction resolution.

Liu et al. [72] proposed a differential transient absorption (DTA) scheme based on the intensity subtraction between an image acquired with a Gaussian pump beam and an image acquired with a doughnut-shaped pump beam. The resolution improvement given by this approach was demonstrated imaging CdSe semiconductor nanobelts with $\sim\lambda/3.0NA$ resolution. This approach does not rely on saturation phenomena, and it can be applied to any absorber not exhibiting saturable transitions.

Regarding saturation-based methods, Silien et al. [73,74] theoretically proposed a vibrational depletion pump-probe scheme for IR absorption microscopy, where a resolution improvement down to $\lambda/10$ can be achieved by saturating the vibrational mode of interest with a vortex-shaped beam.

Wang et al. [85] applied the generalized RESOLFT concept (see **Section 2.3.1**) to GSD pump-probe imaging of graphite nanoplatelets, using a spatially-controlled saturation of the electronic absorption. Bianchini et al. [86] proposed a similar approach to image single layer graphene (SLG) folds.

This approach is based on the collinear superimposition, in a standard two-beam pump-probe configuration, of a high-intensity non-modulated doughnut-shaped pump beam, whose purpose is to transiently saturate the absorption at the periphery of the focal spot. The saturation prevents the absorption of the probe beam, which will be transmitted without any modulation, while the probe intensity variation induced by the absorption of the modulated pump will be detected only form the center of the focal spot (see **Figure 3.3(a)**). The saturation pump beam can be picked before the pump intensity modulator using a beam splitter. The doughnut shape can be generated by applying a 0-2π phase mask through a vortex phase plate (VPP) [86] or a spatial light modulator (SLM) [85]. The saturation pulses need also to be temporally aligned with the pump and probe ones using a dedicated delay line. In order to assure optimal performances, the circular polarization of the doughnut beam [50] needs to be maintained at the focal plane using a pair of half- and quarter-wave plates.

Wang et al. [85] demonstrated this technique to image graphite nanoplatelets, which are strong absorber and saturable materials. The suppression of the pump-probe signal results

exponentially dependent on the saturation pump power (I_{sat}), a behavior that is at the basis for achieving a reduction of the detection volume below the diffraction limit (see **Section 2.3.1**). By fitting the depletion curve with the function [85]

$$\frac{\Delta T}{T} = \frac{1}{1+\frac{I_{sat}}{I_0}} \qquad (3.2)$$

values of 0.43 MWcm^{-2} and 0.28 MWcm^{-2} were derived for the characteristic saturation power I_0 for graphite and graphene nanoplatelets, respectively. By setting the saturation power to 2.0 MW cm^{-2} and its temporal delay to 0.4 ps, sub-diffraction imaging of graphite nanoplatelets was achieved and features of 225 nm ($\sim\lambda/3.0NA$) were probed with an 830 nm probe beam (**Figure 3.3(b)**).

Bianchini et al. [86] reached a resolution of the order of $\sim\lambda/10$ in transient absorption imaging of SLG using wavelengths longer than 1000 nm (**Figure 3.3(c)**).

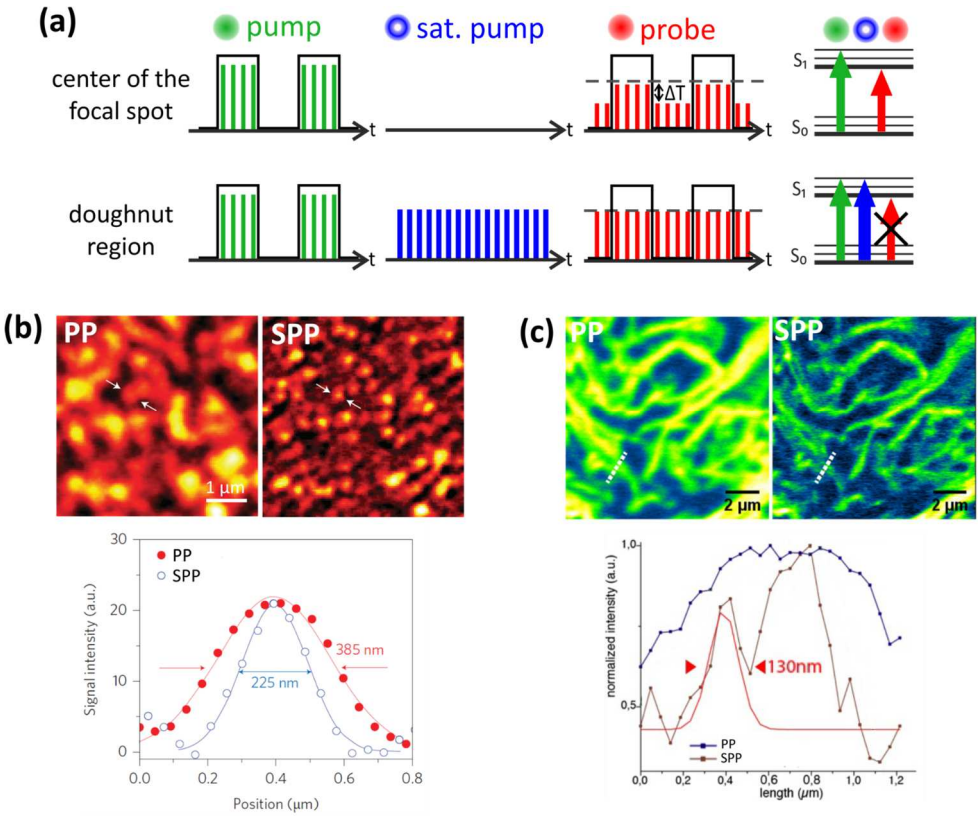

Figure 3.3 (a) Pulse sequence in saturated GSD-based transient absorption microscopy. At the center of the focal spot the same signal detection as presented in **Figure 3.1(c)** occurs. In the periphery, at the doughnut region, the high intensity non-modulated saturation pump beam saturates the absorption (as depicted in the transition diagram on the right) and leaves the probe beam unchanged. The pump temporal modulation is shown as a black square wave. The input probe intensity is marked by a dashed grey line. **(b-c)** Pump-probe (PP) and saturated pump-probe (SPP) images of **(b)** graphite nanoplatelets [85] and **(c)** SLG folds [86].

3.4. Stimulated Raman scattering (SRS) microscopy

Stimulated Raman scattering (SRS) microscopy exploits a pump-probe approach in order to coherently excite Raman-active transitions of intrinsic biomolecules and achieve label-free contrast in living cells and tissues at the molecular level. Intrinsic biomolecules possess specific vibrational spectra that can be measured with Raman scattering and that can provide a characteristic fingerprint of the chemical composition of the system. SRS is sensitive to the same molecular vibrations as the ones probed in spontaneous Raman scattering, but in addition it provides stronger targeted signals, it is proportional to the molecular concentration, and it has the ability to time-resolve molecular dynamics (see **Section 1.2.2**). These advantages have defined SRS as an important tool in chemistry, biophysics, and biomolecular imaging.

A typical SRS microscopy setup is based on a two-beam laser scanning pump-probe setup, as presented in **Section 3.1** and shown in **Figure 3.1(a)**. Picosecond pulsed lasers are normally used in order to increase the spectral resolution and thus the chemical selectivity. Femtosecond laser sources have also been used for SRS in order to increase the signal level and enhance the detection sensitivity and in order to facilitate the coupling with other single-beam non-linear optical microscopy modalities (TPEF, SHG, …) which require ultrashort pulses. Since SRS signal is free of non-resonant background, SRS contrast does not degrade due to the broadening of the pulse bandwidth [4].

As fully explained in **Section 1.2.2**, as a result of the interaction with the sample, the pump beam undergoes an intensity loss ΔT_p called stimulated Raman loss (SRL), while the probe beam (called Stokes beam) experiences an intensity gain ΔT_s, called stimulated Raman gain (SRG). Both complementary signals can be detected with a high-frequency modulation scheme: if the pump is modulated SRG can be filtered in detection, if the Stokes beam is modulated SRL can be detected. Both SRG and SRL scale linearly with the incident intensities and with the molecule concentration (**equation 1.11**). Being a scattering process, SRS interaction can be considered instantaneous and the signal is maximum at zero delay between pump and Stokes pulses. The temporal profiles of the demodulated SRG and SRL signals resembles the one of TPA, exhibiting a symmetric cross-correlation trace.

After its discovery in 1962 [15], SRS interaction resulted in being useful for shifting laser lines to different wavelengths by placing a Raman active medium outside the laser cavity. With the development of picosecond and femtosecond pulsed lasers, time-resolved SRS measurements started to be employed for ultrafast molecular spectroscopy and for studying lattice dynamics, with techniques like impulsive SRS (ISRS) and femtosecond SRS (FSRS) [153].

SRS imaging was first demonstrated in 2008 by Freudiger et al. [154], and in parallel by Nandakumar et al. [155], in different biomedical applications, like in the imaging of lipids in cells, brain and tissues, and in the monitoring of drug delivery through the epidermis, achieving

3D imaging capabilities and a detection sensitivity of $\Delta T_p/T_p < 10^{-7}$ (where T_p is the total transmitted pump intensity). In the same years, Ozeki et al. theoretically and experimentally demonstrated that SRS microscopy possesses a shot-noise-limited sensitivity [156]. These studies assessed the potentiality of the technique for highly-sensitive imaging of biological samples without adding perturbative labels, and with video-rate capabilities [157]. Notable label-free SRS applications can be found in the imaging of nucleic acids in vivo, in the delineation of tumor margins, in the imaging of intracellular drug distribution in living cells, and in the tracking of changes in lipid composition [158]. SRS microscopy started also to be employed as a biorthogonal chemical imaging platform for probing the dynamics of small biomolecules inside living systems, previously tagged with Raman-active vibrational probes like alkynes (C≡C) [159].

3.4.1. Super-resolution approaches in SRS microscopy

Exploiting non-linear optical processes, SRS and CARS microscopy offer sub-micrometer lateral resolution and ~1 μm axial sectioning [158], and the challenge of spatial resolution improvement is still open. The first attempts to improve the spatial resolution proved that resolution just below the diffraction limit is achievable due to the coherent nature of the non-linear interaction under tight focusing conditions [153]. Up to now, few techniques were theoretically proposed and experimentally demonstrated to overcome the diffraction limit in CRS imaging.

In CARS microscopy, super-resolution capabilities were achieved using a focal spot engineering technique and Si nanowires were imaged with 130 nm resolution [160]. A differential approach, based on the intensity difference between an image obtained with a Gaussian pump beam and an image obtained with a doughnut-shaped pump beam, was also applied to CARS microscopy, and lateral resolution between $0.36\lambda_p$ and $0.065\lambda_p$ was achieved [75,76]. The generalized RESOLFT concept (see **Section 2.3.1**) was theoretically proposed to break the diffraction barrier in CARS microscopy, exploiting phonon depletion [80], ground state depopulation [81] or a pre-population of the Raman state [82] with an additional doughnut-shaped beam. Moreover, the exploitation of saturation of the vibrational transition (see **Section 1.2.2**) allowed for spatial and spectral resolution improvement in CARS imaging of diamond samples employing a method similar to the modulated saturated excitation (mSAX) approach found in super-resolution fluorescence microscopy (see **Section 2.3.2**).

In SRS microscopy, just a few theoretically approaches for sub-diffraction imaging were proposed, based on the control of the Raman-active state population using a three-beam setup featuring a doughnut-shaped beam, in a STED-like way (see **Section 2.3.1**). Gong et al. [161] employed a doughnut-shaped Stokes beam to saturate the vibrational transition at the rim of the focal spot and switch off the SRS signal at the periphery of the focal spot. Silva et al. [83]

employed a doughnut-shaped decoherence beam in order to induce a different four-wave mixing de-excitation pathway to turn off the signal in the doughnut region. In a similar way, Kim et al. [84] reported the use of a competing SRS process induced by an additional doughnut-shaped Stokes pulse, in order to arbitrarily decrease the number of pump photons available for the SRS transition under investigation and shrink the PSF. Just as in STED, increasing the power of the doughnut-shaped beams in all these implementations will increase the probability to turn off the SRS transition at the rim of the focal spot, and to dramatically improve the spatial resolution of the experiment.

Up to now, there has been no demonstration of label-free super-resolution CRS imaging of biological samples. Since high peak powers are required for saturation-based experiments, sample damage may be a problem, and optimization of the imaging conditions is necessary.

PART TWO: EXPERIMENTAL RESULTS

4. Transient absorption nanoscopy @ IIT (Genova)

This research was carried out in the Nanoscopy group directed by Prof. Alberto Diaspro at Istituto Italiano di Tecnologia (IIT) in Genoa, Italy.

A custom microscopy setup, used to obtain the results presented inside this chapter, was entirely designed and realized at the Nikon Imaging Center at IIT (https://www.nic.iit.it/) by Dr. Kseniya Korobchevskaya (Nanoscopy, IIT), Dr. Paolo Bianchini (Nanoscopy, IIT) and me, under the supervision of Prof. Alberto Diaspro. Experiments and data analysis were planned and performed by me and Dr. Paolo Bianchini, under the supervision of Prof. Alberto Diaspro. Dr. Kseniya Korobchevskaya, Dr. Takahiro Deguchi (Nanoscopy, IIT) and Dr. Fumihiro Dake (Nikon Corporation, Japan) contributed to the results with useful discussions. Samples were kindly provided by Dr. Amira El Merhie (Nanoscopy, IIT), Dr. Silvia Dante (Nanoscopy, IIT), Dr. Giuseppe Vicidomini (Molecular Microscopy and Spectroscopy, IIT), and Dr. Antonio Esaù Del Rio Castillo (Graphene Labs, IIT).

These results were presented in national (SIBPA 2016, SIBPA 2018) and international (FOM 2017, OPJ 2017, ELMI 2018, ICTON 2018) conferences, and partially published in the Proceedings of the ICTON 2018 conference and inside the chapter "Label-free pump-probe nanoscopy" (Bianchini, Zanini, Diaspro) of the book "Label-free super-resolution microscopy" (ed. V. Astratov), Springer.

4.1. Aim

As presented in the previous chapters, the application of ultrafast pulsed laser sources and spectroscopic techniques are paving the way for non-linear, label-free, deep-tissue optical microscopy. However, the circumvention of the diffraction limit in this field is still an open challenge.

Among such approaches, pump-probe microscopy (see **Chapter 3**) is of increasing interest for the imaging of material and biological samples thanks to its highly specific non-fluorescent-based contrast mechanisms. When dealing with highly absorbing species, non-linear absorption phenomena (see **Section 1.2.1**) may be exploited in order to obtain a pump-probe transient absorption contrast (see **Section 3.3**). Moreover, if the absorption is saturable, the size of the effective focal volume can be controlled and shrunk beyond the diffraction limit exploiting the strong non-linearity contained in saturation processes.

This research aims at applying the RESOLFT approach (see **Section 2.3.1**), originally developed for super-resolution fluorescence microscopy, to label-free transient absorption microscopy exploiting transient absorption saturation with a doughnut-shaped saturation beam. Moreover, it aims at optimizing the imaging parameters in terms of temporal alignment and applied power of the saturation beam for graphene nanoscopy imaging.

The project was developed through the achievement of the following goals:

1. Implementation of a doughnut-shaped absorption saturation beam in a custom femtosecond-pulsed NIR pump-probe microscope (**Section 4.2**).
2. Characterization of the imaging capabilities of the pump-probe setup in terms of spatial and temporal resolution (**Section 4.2.3** and **Section 4.4.1**).
3. Characterization of graphene-based samples like single layer graphene (SLG) and few-layer graphene flakes under the pump-probe microscope, checking their signal dependence on the applied powers, on the sample structure and on the type of interaction, and studying their excited state dynamics (**Section 4.4.1**).
4. Evaluation of the pump-probe signal suppression efficiency induced by the absorption saturation beam in SLG samples, in order to define the optimal imaging conditions in terms of temporal overlap and applied power of the saturation beam (**Section 4.4.2**).
5. Super-resolved imaging of SLG defects using the doughnut-shaped saturation beam (**Section 4.4.3**).

Moreover, since the here presented technique deals with non-linear interactions and NIR illumination, the 3D and the multimodal imaging capabilities of the pump-probe setup were examined (**Section 4.4.4**).

Eventually, since NIR illumination is used, the presence of other non-linearities in the single pump and probe interactions was investigated in order to access an overall higher-order non-linearity of the pump-probe process and an intrinsic higher spatial resolution (**Section 4.4.5**).

4.2. Optical setup

The custom NIR pump-probe setup (**Figure 4.1**) is realized by coupling a tunable mode-locked femtosecond pulsed Ti:sapphire laser (680-1080 nm, 80 MHz, 140 fs, Chameleon Ultra II, Coherent) with a laser scanning Nikon C2 scan head and a Nikon Eclipse FN1 upright microscope body (Nikon Instruments). The Ti:sapphire laser pumps an optical parametric oscillator (Chameleon Compact OPO, Coherent) whose synchronized outputs (the pump at the Ti:sapphire wavelength in the range 740-880 mm, and the signal tunable in the range 1000-1600 nm) are locked at 80 MHz, and have a typical pulse width of 200 fs. The pump output is used as pump beam, and its intensity is modulated at 2 MHz by an electro-optical modulator (EOM, LM 0202, Qioptiq). The electronic synchronization between pulse rate and modulation is controlled and generated by a digital delay generator (DG645, Stanford Research Systems). The signal output is used as probe beam, and its pulses are temporally synchronized with the pump ones using a delay line realized with a motorized high-precision linear stage (M-521.PD, Physik Instrumente, delay up to 1.3 ns with 3 fs accuracy) equipped with a retroreflector (UBBR2.5-2I, Newport Corp.). The two laser beams are spatially combined with a dichroic mirror (DMSP950, Thorlabs), and focused by a 60x 1.27NA water immersion objective (CFI Plan Apo IR, Nikon Instruments). A pair of relay lenses in the probe optical path, with an adjustable position on the optical axis, is used to change the axial position of the focus at the sample plane. The typical wavelengths used for the experiments were **800 nm for the pump beam and 1030 nm for the probe beam.**

The probe beam is collected in transmission by a 40x 0.6NA objective (CFI S Plan Fluor ELWD, Nikon Instruments), filtered by two long-pass filters (RG850, Schott, and FEL1000, Thorlabs) to reject pump light, and detected by an amplified InGaAs detector (PDA20CS, Thorlabs). A phase-sensitive lock-in amplifier (HF2LI, Zurich Instrument) is used to demodulate the probe signal and extract the pump-probe signal at the pump modulation frequency. Both modulus (R) and in-phase component ($X = R\,cos\theta$, where θ is the phase difference respect to the reference modulation, see **Section 3.2**) of the demodulated pump-probe signal can be extracted from separate channels of the lock-in amplifier. The demodulated signals are then acquired by the Nikon controller and images are constructed using NIS-Element Advanced Research (AR) software (Nikon Instruments).

The saturation (pump) beam is picked before the EOM with a 50/50 beamsplitter (UT-800-50-45-UNP-CVI, CVI Melles Griot) and sent through a manual delay line (PT1, Thorlabs, delay up to 170 ps with 60 fs accuracy), which is used to adjust its temporal alignment with respect to pump and probe beams. A vortex phase plate (VPP-1a, RPC Photonics) is then used to obtain the doughnut shape, and the saturation beam is spatially superimposed with the others with a polarizing beam splitter (PBS, PBS203, Thorlabs). In order to assure optimal performances, the

circular polarization of the doughnut beam is maintained at the objective plane using a pair of half- and quarter-wave plates [50].

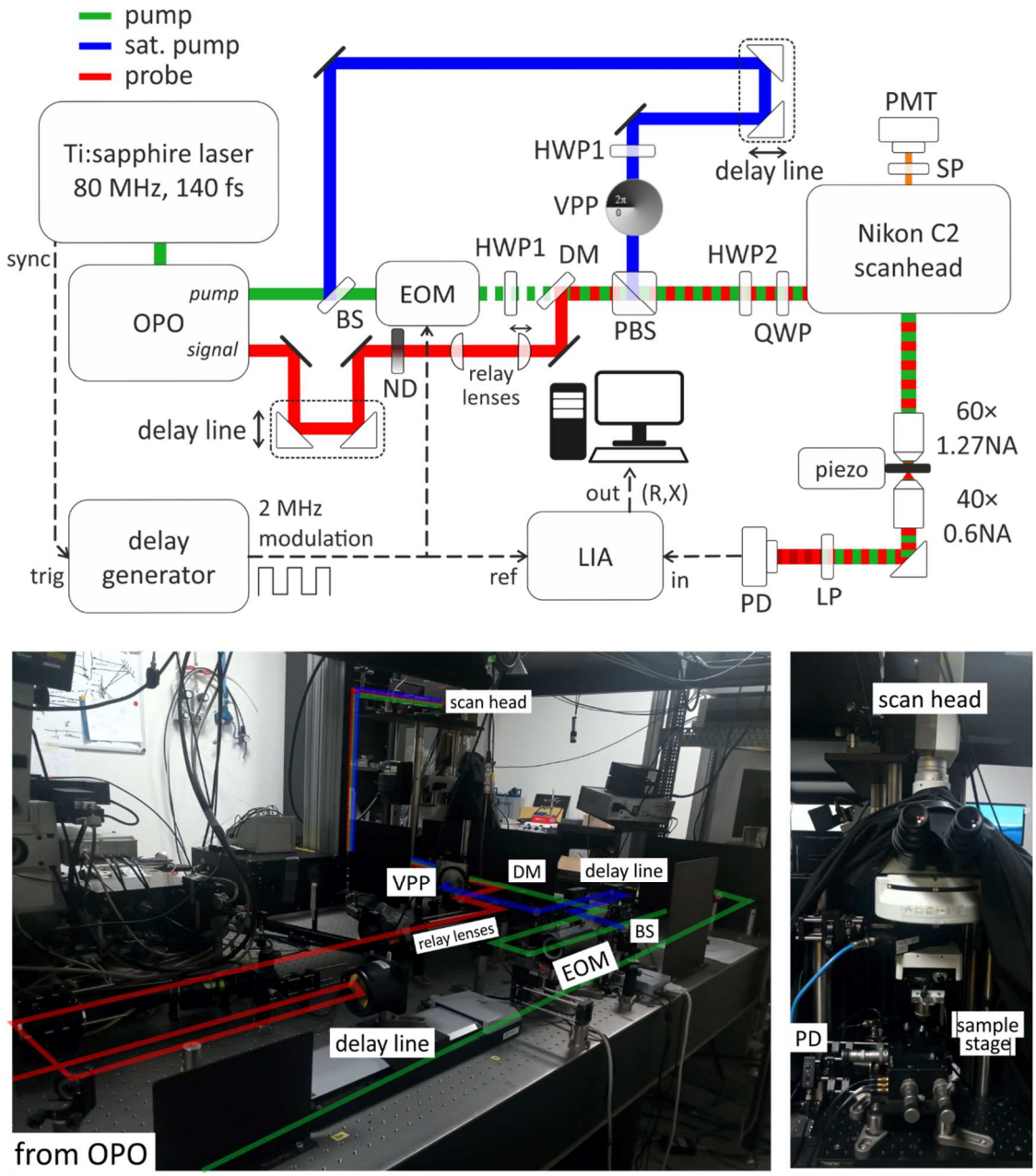

Figure 4.1 Custom NIR pump-probe optical setup built in the Nikon Imaging Center at IIT. The pump beam optical path is shown in green, the probe one in red, and the saturation pump one in blue. OPO: optical parametric oscillator with pump and signal outputs, BS: beam splitter, EOM: electro-optical modulator, DM: dichroic mirror, VPP: vortex phase plate, HWP: half-wave plate (#1 used for power adjustment, #2 used for polarization control), QWP: quarter-wave plate, PBS: polarizing beam splitter, ND: neutral density filter, PMT: photomultiplier tube, SP: short-pass filter, LP: long-pass filter, PD: photodiode, LIA: lock-in amplifier, NA: numerical aperture, sync: synchronization, trig: trigger, ref: reference, in: input, out: output, (R,X): modulus and in-phase component of the demodulated signal, respectively.

Pump and saturation pump laser powers are controlled by two half-wave plates, while probe power is controlled by a continuously variable neutral density filter (NDC-50C-4M, Thorlabs).

Two-photon excitation fluorescence (TPEF) is collected with a photomultiplier tube (PMT) of the Nikon detector unit, using a 680 nm short pass filter (FF01-680/SP-25, Semrock) and open pinhole.

The sample is placed on a 3-axis piezo-electric stage (P-611.3S NanoCube®, Physik Instrumente, travel range 100 µm × 100 µm × 100 µm, resolution 1 nm) which enables 3D image acquisition.

Image analysis is performed with ImageJ/Fiji (NIH) [162], and data is analyzed and graphed with Origin (OriginLab Corporation).

4.2.1. Pump modulation

The high-frequency modulation of the pump beam at 2 MHz is realized through an electro-optical modulator (EOM), which exploits the Pockels effect to achieve amplitude modulation of the transmitted beam. A delay generator, synchronized with the pulse repetition rate of the Ti:sapphire laser, is used to generate a square wave at 2 MHz which will drive the EOM. In **Figure 4.2(a)** the laser synchronization output, used as the trigger input to the delay generator, is recorded with an oscilloscope and exhibits the typical 80 MHz repetition rate of the Ti:sapphire laser. In **Figure 4.2(b)** the square wave at 2 MHz produced by the delay generator is shown. In **Figure 4.2(c)** the resulting transmitted beam modulation is detected with a fast photodiode (DET10A, Thorlabs) placed after the EOM. The single 80-MHz pulses are resolved, together with their 2-MHz intensity modulation. The delay generator parameters can be adjusted in order to optimize the output beam modulation, finding a compromise between pushing the minimum value to zero over half of the period and flattening the maximum value over the other half of the period.

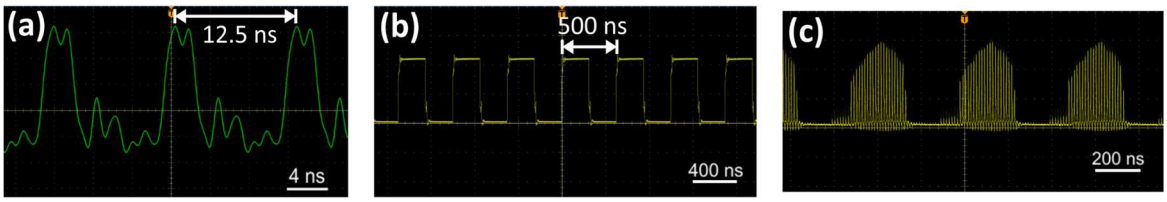

Figure 4.2 (a) 80-MHz synchronization signal coming from the Ti:sapphire laser and used ad trigger for the delay generator. **(b)** 2-MHz square wave generated by the delay generator and used to drive the EOM. **(c)** Modulated laser beam detected at the EOM output with a fast photodiode.

4.2.2. Spatial alignment

The spatial superimposition of pump and probe beams at the focus is a fundamental point for the confinement of the non-linear interaction volume and the optimization of pump-probe signal generation. A dichroic mirror (DM in **Figure 4.1**) is used to combine the beams in the xy

plane. The matching of the foci in the z-direction, which, as explained in **Section 3.1**, is not straightforward due to chromatic aberrations, can be achieved by adjusting the probe focus with a couple of relay lenses. Experimental results of pump and probe point spread functions (PSFs) obtained imaging 200-nm yellow-green fluorescent beads are shown in **Figure 4.3(a)**.

Moreover, the correct superimposition of the doughnut-shaped beam, with the hole centered with pump and probe excitation PSFs, can be achieved through a polarizing beam splitter (PBS in **Figure 4.1**), and it is fundamental for a successful shrinking of the detection volume under saturated condition. Experimental result of the doughnut PSF superimposition obtained in reflection is shown in **Figure 4.3(b)**.

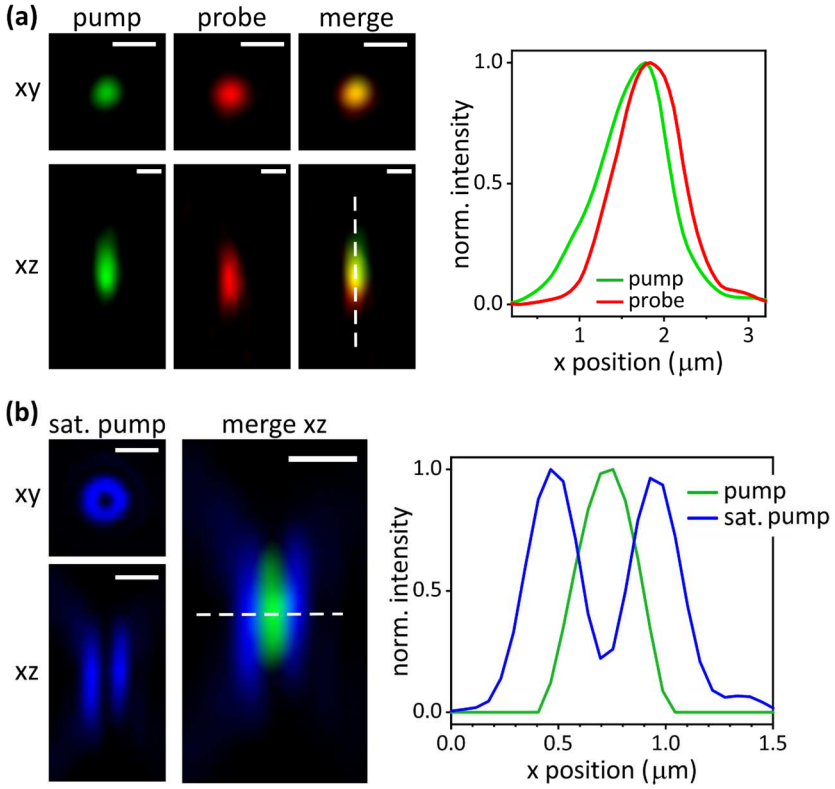

Figure 4.3 (a) Experimental pump and probe PSFs obtained imaging 200-nm yellow-green fluorescent beads. A slight foci displacement is still present, as it can be seen from the z profiles along the dashed line, and this is due to chromatic aberrations. Scale bar 500 nm. **(b)** Experimental doughnut-shaped PSF of the saturation pump beam obtained in reflection, imaging 150-nm gold beads (left), and PSF merge with the pump beam (right). The line profiles along the dashed line show the superimposition of the doughnut hole with the excitation beam. Scale bar 500 nm.

4.2.3. Temporal alignment and resolution

The pump-probe signal generation is strongly determined not only by the spatial alignment of pump and probe pulses at the focus but also by their temporal synchronization. The adjustment of the pulses delay is achieved with a delay line placed in the probe optical path.

In first approximation, the position of the pulses is checked and adjusted, before the scan head, with a fast photodiode (DET10A, Thorlabs) and an oscilloscope (**Figure 4.4(a)**). To increase the level of accuracy in the temporal alignment, the sum frequency generation (SFG) effect generated in a non-linear BBO (beta barium borate) crystal can be used. Focusing the two pulsed beams on the crystal, the SHG components at exactly half of their wavelengths are generated. If the pulses interact simultaneously on the crystal, also the SFG signal appears at the wavelength $\frac{1}{\lambda_{SFG}} = \frac{1}{\lambda_{pu}} + \frac{1}{\lambda_{pr}}$. Experimentally, when the SFG spot appears at the output of the crystal, it means that the pulses are overlapped, and this overlap can be tuned by maximizing the brightness of the SFG spot (**Figure 4.4(b)**).

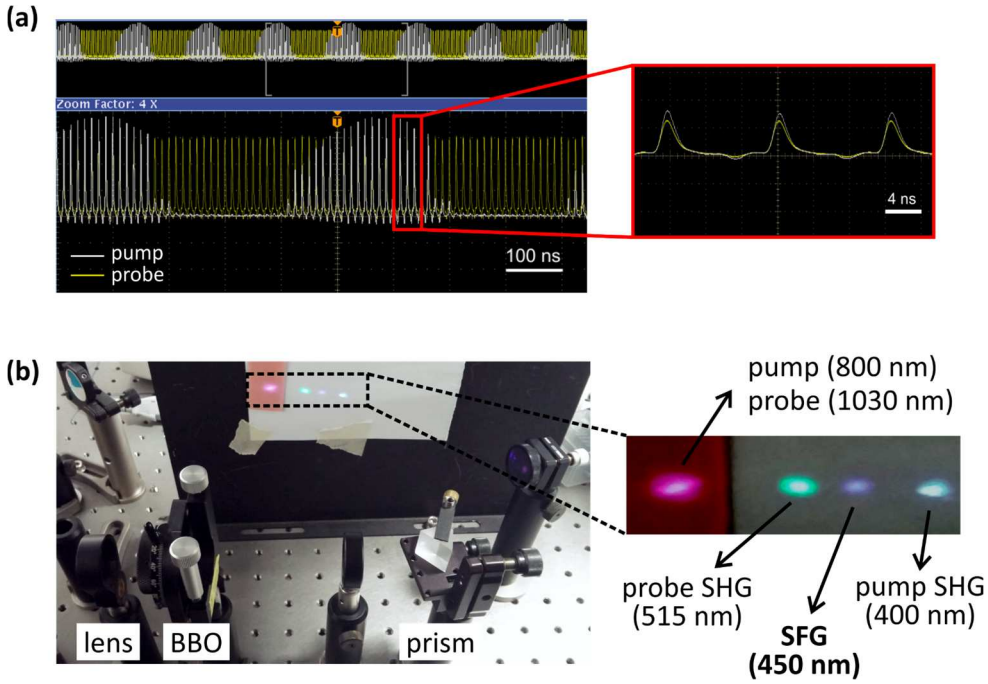

Figure 4.4 (a) Pump and probe pulse traces (in white and yellow, respectively) recorded with a fast photodiode and an oscilloscope. The zoom shows pulse overlapping. **(b)** The photo on the left shows the additional optical components inserted in the pump-probe setup for the temporal alignment of pump and probe pulses through SFG on a non-linear BBO crystal. A lens is used to focus pump and probe beams on the BBO crystal, while a prism is used to chromatically disperse the outputs and project them on a screen. The transmitted NIR input beams (in this case tuned to 800 nm and 1030 nm) are made visible using a NIR card and they appear like a red spot. Three new output beams appear. The violet and the green spots represent the SHG output beams at exactly half the input wavelengths (400 nm and 515 nm, respectively). The blue spot at 450 nm represents the SFG interaction of the two pump and probe pulses, which means that the pulses are synchronized.

In order to finely adjust the temporal alignment at the sample plane and evaluate the temporal resolution of the system, stimulated Raman scattering (SRS, see **Section 1.2.2** and **Section 3.4**) imaging of lipids was used. Being a scattering process, the SRS interaction can be considered instantaneous. The maximum signal is obtained when pump and probe (Stokes) pulses interact simultaneously on the sample (zero delay), while the temporal behavior of the

signal varying the time delay reflects the cross-correlation of the two pulses or, in other words, the system temporal response. Tuning pump and probe (Stokes) beams to 800 nm and 1036 nm respectively in order to excite the characteristic CH_2 vibrational resonance of lipids at 2845 cm^{-1}, an oil drop was imaged at different pump-Stokes delays (see **Figure 4.5(a)**). Plotting the average signal as a function of the delay, a temporal resolution of **(380 ± 10) fs** was obtained through a Gaussian fit of the data (see **Figure 4.5(b)**). This confirms the expected sub-picosecond temporal resolution of a pump-probe system, which permits to follow the ultrafast dynamics of the excited states.

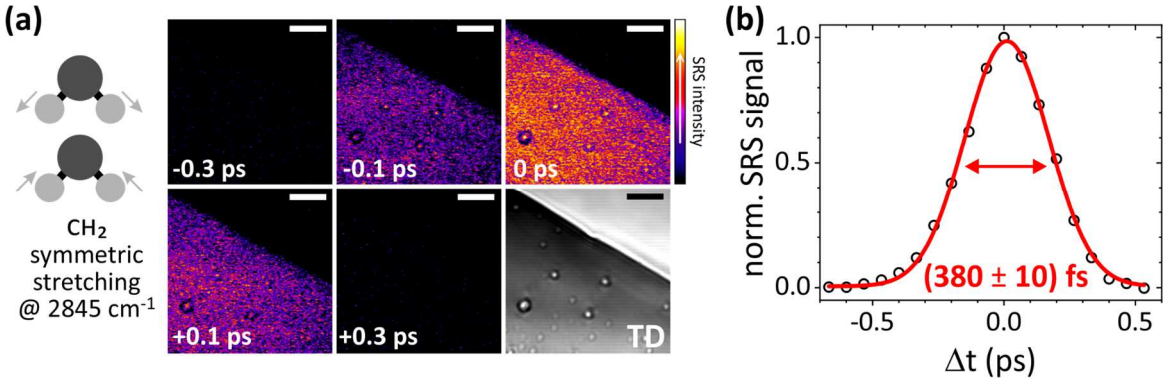

Figure 4.5 (a) Diagram of CH_2 vibrational resonance of lipids and SRS images of an oil drop at the interface with air. Images were acquired at different time delays between pump and Stokes pulses. The correspondent transmission image (TD) is shown for comparison. Scale bar 10 µm. **(b)** Plot of the normalized SRS signal as a function of delay between pulses. The Gaussian fit and its FWHM are shown in red.

4.3. Samples

4.3.1. Single layer graphene (SLG)

A single layer graphene (SLG) sample was purchased from Graphene Supermarket (Graphene Laboratories Inc.). It consists of a monolayer graphene film grown by chemical vapor deposition (CVD) processing onto copper foil [163] and then transferred onto a 0.7-mm thick glass substrate [164]. The side with the deposited SLG was mounted on a 0.17-mm coverglass to be placed under a water immersion objective. The graphene film is mostly continuous, with occasional holes and cracks, and has a polycrystalline structure, made of grains with different crystallographic orientations. The sample transmission is reported to be above 97% [165], which makes it suitable to collect the signal efficiently in transmission.

A second SLG sample was prepared via CVD processing at the Center for Nanotechnology Innovation@NEST (IIT) under the supervision of Dr. Camilla Coletti, and it was transferred on a glass substrate and then provided for the experiments by Dr. Amira El Merhie and Dr. Silvia Dante (Nanoscopy, IIT).

Some experiments were performed with SLG on top of which mouse neuroblastoma (N2a) cells were grown and fixed.

4.3.2. Graphene-based inks

Few-layer (<5) graphene and graphene oxide flakes dispersed in water were prepared in the Graphene Labs at IIT [166,167] and provided by Dr. Antonio Esaù Del Rio Castillo. The dimension of the flakes varies from few nanometers up to few micrometers, with a higher population around 500-nm size for the graphene sample, and around 1-µm size for the graphene oxide sample.

4.3.3. CdSe/CdS giant-shell nanocrystals (NCs)

Core-shell CdSe/CdS nanocrystals (NCs) were provided by Dr. Giuseppe Vicidomini and synthesized in the Nanochemistry Department at IIT. Their absorption and size-dependent photoluminescence properties lay in the visible range and are well reported in [168].

4.4. Results and discussion

4.4.1. Transient absorption imaging of graphene-based samples

As introduced in **Section 3.3**, pump-probe microscopy is extensively used to study optoelectronic properties of non-fluorescent nanomaterials, and among them, graphene recently gained a particular interest. Due to its particular linear electronic band structure, graphene shows a wavelength-independent, broadband optical absorption (~ 2.3% per layer [169]) in the NIR part of the spectrum [170]. This makes absorption-based pump-probe microscopy as an ideal technique for studying its carrier dynamics and for performing imaging using NIR wavelengths.

In this first part of results, graphene-based samples like **SLG**, **graphene ink** and **graphene oxide ink** were imaged in order to assess the imaging capabilities of this setup. Pump and probe wavelengths were tuned to 800 nm and 1030 nm, respectively. It is expected that both wavelengths are absorbed to the same extent and can be used to monitor the carrier population of graphene's excited state looking at the variation of the probe transmission due to the presence of the pump.

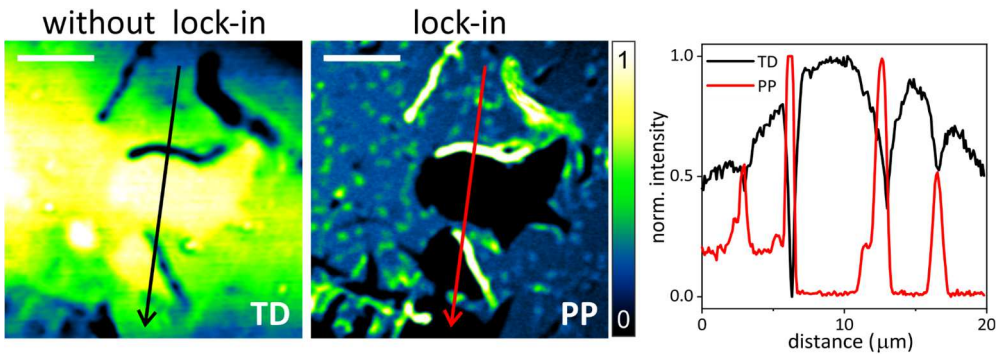

Figure 4.6 SLG imaged with the high-frequency modulation pump-probe scheme. The transmitted probe is detected without (left) and with (right) the demodulation of the lock-in amplifier. Without the lock-in, a transmission image is obtained (TD). Switching the lock-in on, the small modulated fraction of the transmitted probe beam can be extracted and a pump-probe image can be obtained (PP). Scale bar 5 μm. Intensity line profiles across the central hole are also shown.

In **Figure 4.6**, an example of **SLG** pump-probe image is shown, which aims at underlying the importance of the high-frequency modulation and lock-in demodulation scheme to extract the pump-probe signal. SLG is imaged with the 2-MHz modulated pump beam and the spatially and temporally aligned probe beam, and the transmitted probe signal is collected without (left) and with (right) the lock-in demodulation. Without the lock-in demodulation, a transmission image (TD) is obtained. Switching the lock-in amplifier on, the small modulated fraction of the transmitted probe beam can be extracted with high signal-to-noise ratio (SNR), and a pump-

probe image (PP) is obtained, showing high contrast and high level of sample detail. Single layer sensitivity is achieved, and SLG defects, folds and cracks can be appreciated. According to the drawn line profiles, TD and PP signals are almost complementary: for example, the central area exhibits the highest signal in the TD image while it results to be completely dark in the PP image, confirming the presence of a hole in SLG sample.

The pump-probe technique achieves large area imaging with single-layer sensitivity in short acquisition time and using low excitation powers. In **Figure 4.7**, two regions of a SLG sample previously laser-ablated in stripes are presented. Usually, Raman spectroscopy is used to check if the SLG transfer and the laser ablation were successful. Raman spectra require long acquisition times and for this reason they are acquired in a limited number of ablated and non-ablated regions, picked by looking at the sample with a white lamp. Raman peaks are then compared to the known graphene ones to check the quality of the graphene (in non-ablated areas) or the efficiency of the ablation (in ablated areas). However, this investigation is only punctual and doesn't give information from all the sample.

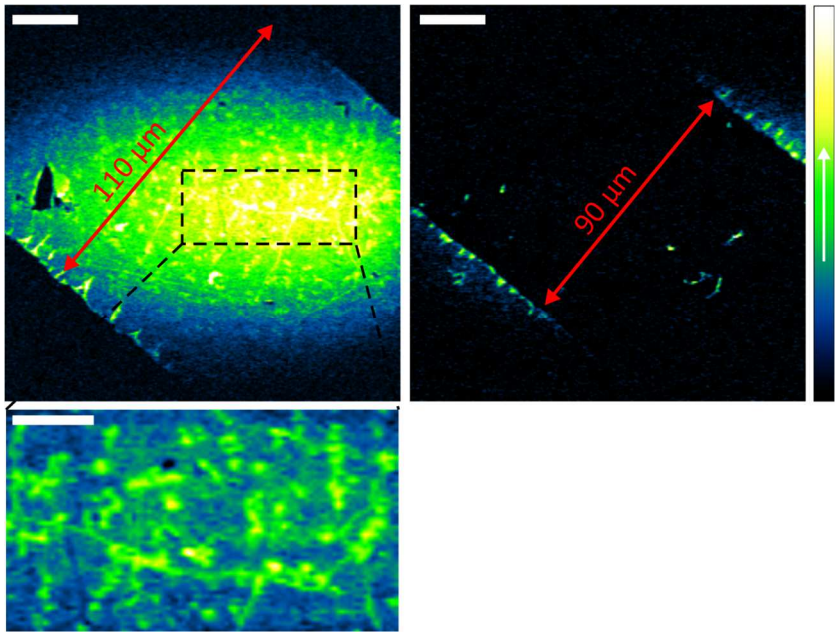

Figure 4.7 Pump-probe images of a laser-ablated SLG sample. A 110-µm wide stripe of SLG is compared to a 90-µm wide ablated area. Scale bar 20 µm. The dashed rectangle marked the evenly illuminated field of view, which is shown zoomed in the bottom row. Scale bar 10 µm.

With the pump-probe microscope, an area of 128×128 μm^2 can be imaged in 1.3 seconds using 2 mW of pump beam and 1.3 mW of probe beam. The sample structure can be checked live under the microscope using the translational stage, and further information can be accessed, like the width of ablated and non-ablated regions or the quality of the single graphene layer. From images in **Figure 4.7** it can be seen that the ablation was successful: the graphene stripe is well defined and in the ablated region only a few graphene residues are

present. The laser-machine parameters were set to obtain 100-µm wide ablated stripes separated by 100-µm wide graphene stripes. The resulting sample consists of 90-µm wide ablated regions and 110-µm wide non-ablated regions.

The graphene layer presents some holes and cracks, and the signal is not uniform. First of all, the non-uniformity of the signal in the whole field of view is due to spherical aberrations present in the microscope. A smaller area of about 50×30 µm^2 can be considered uniformly illuminated (see zoomed region in **Figure 4.7**) and inside it another signal non-uniformity is present which is related to the graphene structure, as explained below.

As described in the theoretical **Section 3.3**, the modulus of the pump-probe signal is proportional to the molecular density c, or more in general to the density of electronic transitions (see **equation 3.1**). This means that, for a regular bidimensional SLG sample, a uniform signal is expected. What is actually obtained is a certain level of non-uniformity in the recorded pump-probe signal, which is related to the presence of defects in the graphene structure. In particular, multilayer graphene regions will exhibit higher signal levels.

An example of this behavior is shown in **Figure 4.8**. A uniformly illuminated 30×30 µm^2 SLG area is presented. It was imaged using 4 mW of pump beam at 800 nm and 1 mW of probe beam at 1030 nm, and both fluorescence and pump-probe signals were collected.

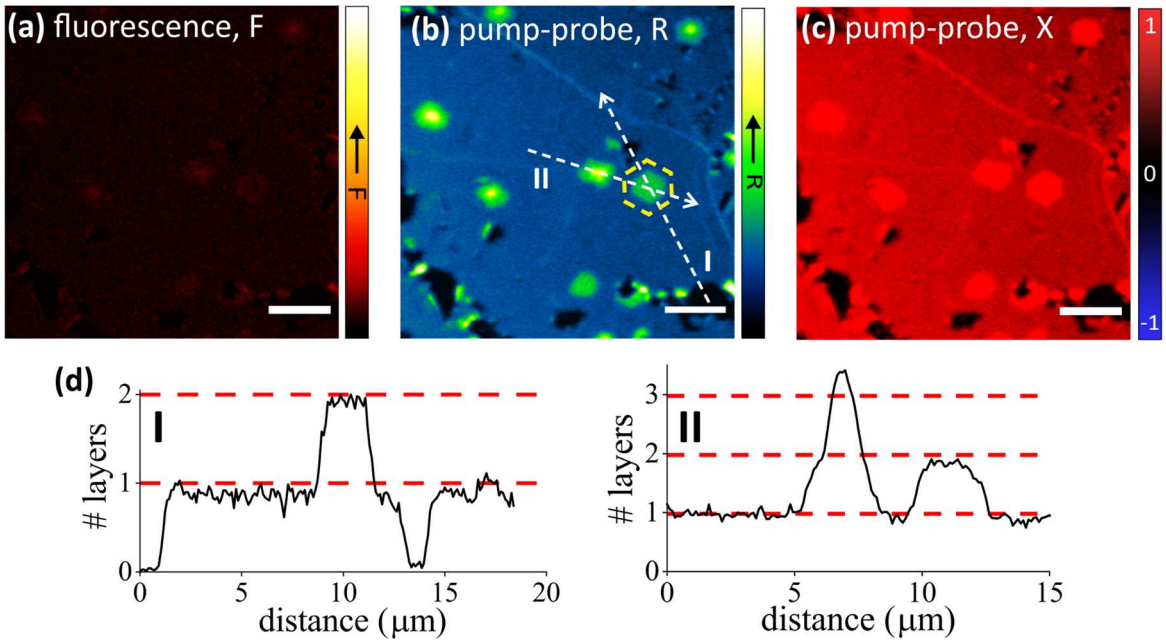

Figure 4.8 SLG imaging: fluorescence image **(a)**, pump-probe image demodulated in the modulus channel R **(b)** and in the in-phase channel X **(c)**. Scale bar 5 µm. **(d)** Line profiles along the white dashed arrows in the pump-probe image in **(b)**.

Graphene exhibits a low fluorescence quantum yield, as shown in **Figure 4.8(a)**, and just a few bright areas can be easily noticed. On the contrary, the non-fluorescence-based pump-

probe signal (**Figure 4.8(b)**) provides a uniform signal coming from the single layer covering the majority of the field of view (FOV), and exhibits the same brighter areas as found in the fluorescence image but with much higher SNR. The line profiles (I and II) along the dashed arrows are plotted in **Figure 4.8(d)**, and they show that the pump-probe signal intensity is quantized, and specifically that it is linearly proportional to the number of graphene layers. Along the line profile I a double layer defect with the characteristic hexagonal shape can be clearly distinguished (yellow contoured region in **Figure 4.8(b)**). The linearity of the signal intensity with respect to the number of layers is not fulfilled for a multilayer area along the line profile II, probably due to the presence of additional layers of sub-resolved lateral sizes whose real signal intensity is averaged down to smaller values.

As explained in **Section 3.2**, not only the modulus $R \equiv |\Delta T|$ of the pump-probe signal can be extracted with the lock-in amplifier, but also its phase θ and in particular the in-phase component $X = R\ \cos\theta$. **Figure 4.8(c)** is built with the X component of the demodulated signal, and exhibits positive values. The presence of such transient absorption contrast, together with the fact that the absorption coefficient of graphene is the same at both pump and probe wavelengths, suggests that the pump excitation causes an absorption reduction at the probe frequency, which can be attributed to a ground state depletion (GSD) interaction.

Looking at the **equation 3.1** in **Section 3.3**, the pump-probe signal should be proportional also to the incident pump and probe intensities. The experimental power curves acquired on SLG are shown in **Figure 4.9**. The linearity of the signal respect to the applied powers is fulfilled for both beams at relatively low-intensity regimes, and in both single layer and multilayer areas, giving slopes close to 1 in the log-log plots. In particular, the linear fits retrieve slopes of 0.80 ± 0.10 and 0.72 ± 0.03 for the pump power curves in **Figure 4.9(a)** (for single layer and multilayer defects, respectively), and slopes of 1.1 ± 0.1 in both probe power curves in **Figure 4.9(b)**.

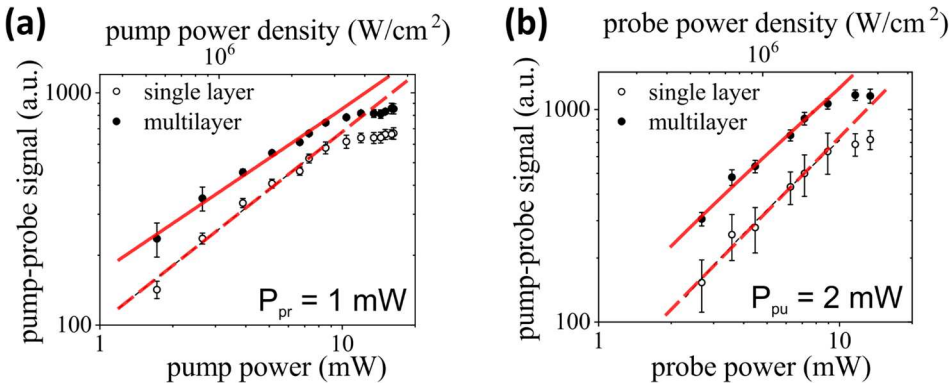

Figure 4.9 Log-log plots of the pump-probe signal from SLG and multilayer defects as a function of pump **(a)** and probe **(b)** excitation powers (and power densities), showing an initial linear behavior followed by signal saturation. The dashed and solid red lines show the linear fits at low powers for SLG and multilayer defects, respectively.

At higher incident powers, the state filling effect of the higher electronic states is expected to occur as a consequence of the Pauli exclusion principle, and the absorption will saturate [171]. Such broadband saturable absorption behavior of graphene-based materials have been previously investigated [172] and reported for single and multilayer graphene [173]. Looking at the graphs, signal saturation starts to appear around an average power density of 2 $MWcm^{-2}$ for both pump and probe beams, which corresponds to an applied power around 6 mW for the pump and 10 mW for the probe.

Pump-probe techniques were initially developed as spectroscopic approaches for monitoring ultrafast processes. Graphene exhibits an ultrafast excited state dynamics [129], with a lifetime that is much shorter (~ps) than the typical lifetime of a fluorescent molecule (~ns), and that can be retrieved with a system with enough temporal resolution. It was demonstrated in **Section 4.2.3** that the optical setup here presented possesses a sub-picosecond temporal resolution of about 400 fs, which allows to follow graphene dynamics.

Experimental time-resolved spectra of SLG and of its multilayer defects, acquired monitoring the pump-probe signal (modulus) at different pump-probe delays, are presented in **Figure 4.10**. Negative delays indicate when the probe arrives at the sample before the pump, positive delays when it arrives after the pump. As expected, the pump-probe signal is maximum at zero delay, when pump and probe pulses are temporally overlapped at the focus, while at larger probe delays it exponentially decreases following the typical dynamics of the excited state relaxation.

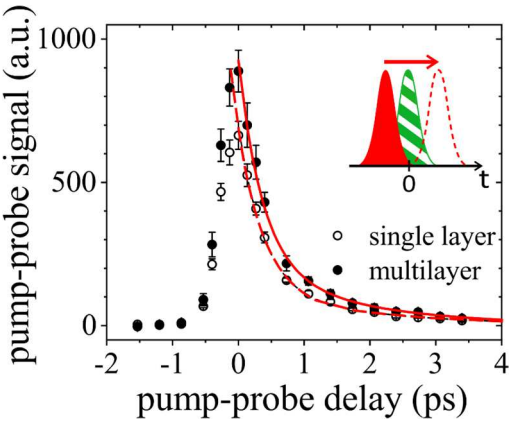

Figure 4.10 Time-resolved spectra of SLG and multilayer defects obtained at different delays of the probe pulse with respect to the pump pulse. The inset shows the pulse sequence sketch (pump pulse at t=0 in dashed green, probe pulse in solid red). The pump-probe signal was fitted with a double exponential decay and the outputs are shown as a dashed red curve for SLG and as a solid red curve for multilayer defects.

Double exponential fits were performed on these data. The solid fitted curve on SLG retrieves a fast component with (0.38 ± 0.03) ps lifetime and a slow component with (1.9 ± 0.2) ps lifetime. The dashed fitted curve on multilayer defects retrieves a fast component with

(0.40 ± 0.10) ps lifetime and a slow component with (1.6 ± 0.2) ps lifetime. The fast time constant cannot be correctly retrieved because it is beyond the temporal resolution of the system, while the slow component lies in the picosecond regime and shows a slightly faster behavior in the presence of multilayer defects. Few spectroscopic experiments on SLG are found in literature, but the hereby presented results are in good agreement with previously published works on other graphene-based nanostructures [85,136]. The slow decay component in the range 0.4-1.7 ps was attributed to carrier–phonon interaction and resulted inversely proportional to the crystal disorder, and the fast unresolved component in the sub-100 fs timescale was attributed to carrier-carrier recombination processes.

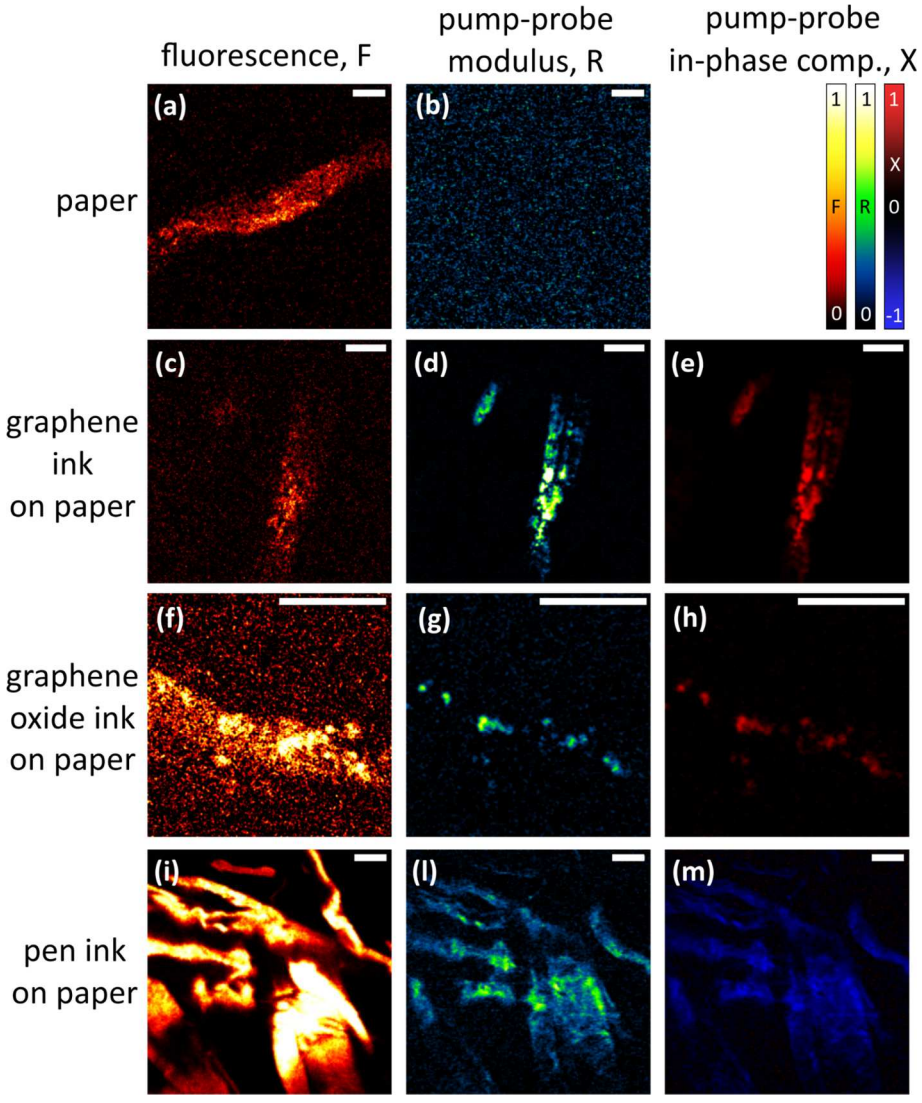

Figure 4.11 Fluorescence (F), pump-probe modulus (R) and pump-probe in-phase component (X) images of **(a-b)** paper, **(c-e)** graphene ink on paper, **(f-h)** graphene oxide ink on paper, and **(i-m)** black pen ink on paper. Scale bar 10 μm. Calibration bars are shown in the first raw.

Not only SLG was studied with the custom pump-probe setup, but the same experiments were performed to characterize **graphene** and **graphene oxide inks** composed by few-layer flakes dispersed in water.

In **Figure 4.11**, fluorescence **(c,f)**, pump-probe modulus **(d,g)** and pump-probe in-phase component **(e,h)** images of graphene-based inks deposited on paper fibers are presented. Pump and probe wavelengths were tuned to 800 nm and 1030 nm, respectively, as in the SLG experiments. As a comparison, fluorescence and pump-probe images of clean paper fibers are shown in **Figure 4.11(a-b)**: the fiber can be distinguished in the fluorescence channel while no pump-probe signal is detected. On the contrary, high contrast pump-probe signal is generated by graphene and graphene-oxide inks (**Figure 4.11(d,g)**). The fluorescence of the paper fiber is also detected when the inks are deposited (**Figure 4.11(c,f)**) together with some fluorescence directly emitted by the flakes, especially from graphene oxide which is known to be fluorescent and to be excited by two-photon absorption [174].

The in-phase component of the pump-probe signal (**Figure 4.11(e,h)**) is positive as found for the SLG sample (**Figure 4.8(c)**), suggesting that the in-phase GSD transition of graphene is occurring. As a comparison, black pen ink on paper was also imaged (**Figure 4.11(i-m)**) which exhibits an anti-phase pump-probe signal (negative signal in **(m)**), an indicator of excited state absorption (ESA) interaction as previously reported [175].

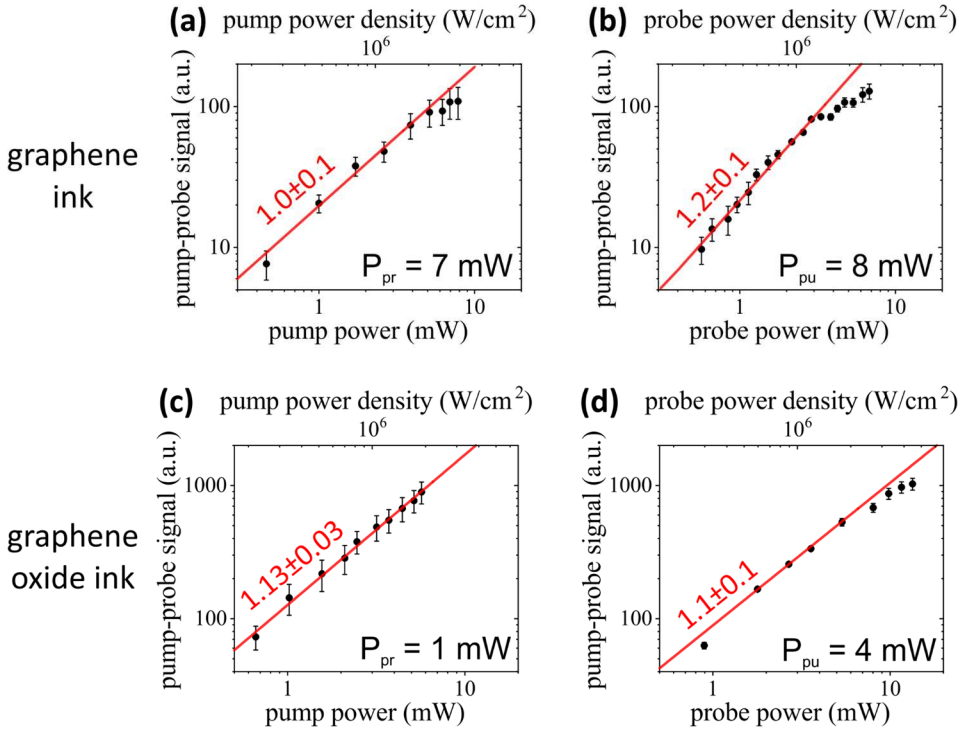

Figure 4.12 Log-log plots of the pump-probe signal from graphene ink **(a-b)** and graphene oxide ink **(c-d)** as function of pump **(a,c)** and probe **(b,d)** excitation powers (and power densities), showing an initial linear behavior followed by signal saturation. The linear fits at low powers are shown as solid red lines and their slopes are written in the graphs.

The linearity in the behavior of the pump-probe signal as a function of the applied powers is also retrieved for graphene and graphene oxide inks. As shown in **Figure 4.12**, the linear fits at low powers of the log-log pump power plots possess slopes of 1.0 ± 0.1 and 1.13 ± 0.03 for graphene ink (a) and graphene oxide ink (c), respectively. The linear fits at low powers of the probe power curves exhibit slopes of 1.2 ± 0.1 and 1.1 ± 0.1 for graphene ink (b) and graphene oxide ink (d), respectively. Moreover, saturation starts to appear below 10 mW, around a power density of 2 $MWcm^{-2}$ as found for SLG (see **Figure 4.9**).

The time-resolved spectra of the two inks, obtained monitoring the pump-probe signal modulus at different pump-probe pulse delays, are presented in **Figure 4.13**. The double exponential decay fits retrieve a fast decay component of the order of the temporal response of the system, and a slow decay component in the picosecond regime. Few-layer graphene ink possesses a slow component with a lifetime of (1.7 ± 0.5) ps, similar to the one obtained for multilayer defects in SLG (see **Figure 4.10**). The slow component of the graphene oxide results faster, with a lifetime of (1.2 ± 0.4) ps.

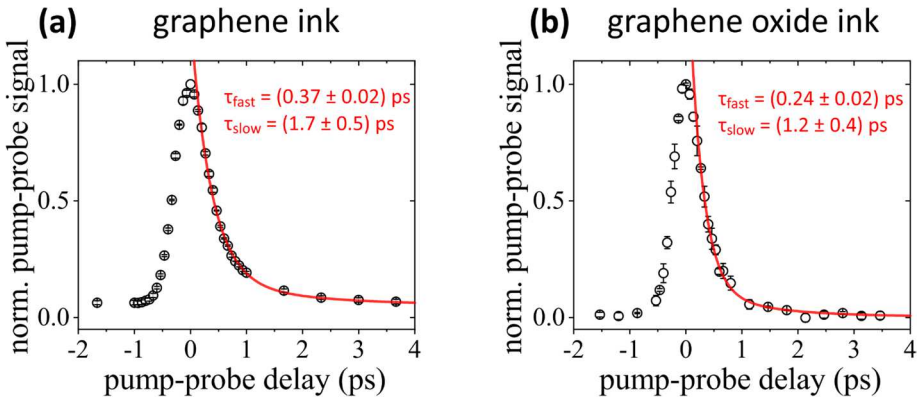

Figure 4.13 Time-resolved spectra of graphene ink **(a)** and graphene oxide ink **(b)** obtained delaying the probe pulse with respect to the pump pulse. The pump-probe signal was fitted with a double exponential decay and the output curves are shown in solid red. The retrieved fast and slow lifetimes are reported in the graphs.

4.4.2. Absorption saturation efficiency in SLG

As extensively presented in **Section 4.4.1**, the optical properties of graphene-based samples are characterized by a broadband saturable absorption, and an ultrafast carrier dynamics. These characteristics make graphene as a suitable candidate to explore saturation phenomena for super-resolution transient absorption imaging.

The non-modulated saturation pump beam is here introduced in the experiments. As shown in **Figure 4.9** and **Figure 4.12**, the state filling effect at high incident powers leads to saturation of the absorption in graphene-based samples, which is reflected in the decrease of the detected

pump-probe signal. If the saturation is caused by the additional non-modulated pump beam, the pump-probe signal is brought to zero because the lock-in detection will not identify any modulation of the probe. This effect can be exploited similarly to the STED microscopy principle (see **Section 2.3.1**), using the non-modulated saturation beam with a doughnut-shaped to reduce the PSF to sub-diffraction dimensions (see **Figure 3.3(a)**).

To evaluate the pump-probe signal suppression efficiency induced by the saturation beam, the commercial **SLG** sample was first imaged using the saturation beam with Gaussian shape by misaligning the vortex phase plate (VPP) in the setup (see **Section 4.2** and **Figure 4.1**). The effect was studied as a function of the temporal alignment of the saturation pulse respect to the pump one (whose temporal position defines the "time zero"), and as a function of the power of the saturation beam.

Temporal dependence. The temporal dependence was studied using two different signal acquisition modalities.

The first modality (**Figure 4.14**) investigates the non-saturated and saturated time-resolved spectra with the saturation pulse at three different time delays respect to the time zero (-0.4 ps, 0 ps, and +0.8 ps) in order to resolve the position of the saturation pulse in the dynamics of the excited states. The pulse sequence characterizing this experiment is sketched in **Figure 4.14(a)**. Negative delays indicate when the saturation pulse arrives at the sample before the pump pulse, positive delays when the saturation pulse arrives after the pump pulse.

The second modality (**Figure 4.15**) investigates the depletion efficiency delaying the saturation pulse while keeping the probe pulse at time zero, in order to find the optimal temporal alignment of the saturation beam. The pulse sequence characterizing this experiment is sketched in **Figure 4.15(a)**.

Results obtained with the first acquisition modality are shown as empty black data points in **Figure 4.14(b-d)** (○ for non-saturated and Δ for saturated conditions). Data was acquired in SLG with pump at 5 mW and probe at 1 mW. Saturation pump was kept at 10 mW when at -0.4 ps (**Figure 4.14(b)**), 5 mW when at 0 ps (**Figure 4.14(c)**) and 20 mW when at +0.8 ps (**Figure 4.14(d)**). Data was normalized with respect to the maximum of the non-saturated one. Data reported with full colored points represents the ratio of saturated and non-saturated signals at each delay, which shows the efficiency of the saturation beam in signal suppression.

Looking at the ratio at each delay, it is possible to determine the position of the saturation pulse with respect to the excited state dynamics. At the delay position where the signal suppression effect is the highest, and therefore the ratio has its minimum value, the saturation pulse is found. Its temporal position is highlighted by a shaded colored area, whose width is determined by the temporal resolution of the system (about 400 fs, as calculated in **Section 4.2.3**).

In the condition where the pump-probe signal generation is at its maximum, which is at time zero, the achieved signal suppression is demonstrated to be strongly dependent on the delay of the saturation pulse and on its power. Notably, 50% of the signal suppression is obtained using just half of the saturation power when moving the saturation pulse from -0.4 ps to 0 ps. Interestingly, at a longer delay of +0.8 ps such depletion efficiency cannot be reached even by quadrupling the saturation power.

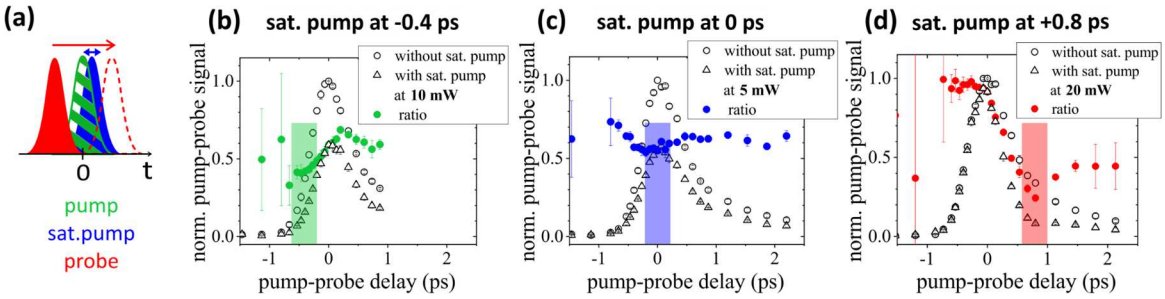

Figure 4.14 (a) Pulse sketch of the experimental acquisition modality to investigate non-saturated and saturated time-resolved spectra in SLG. The pump pulse is drawn in striped green, the probe pulse in red, and the saturation pulse in blue. The temporal position of the pump pulse defines the time zero. **(b-d)** Time-resolved spectra obtained without (○) and with (Δ) saturation pump at different time delays respect to the pump one and at different powers: **(b)** saturation beam at -0.4 ps and 10 mW, **(c)** saturation beam at 0 ps and 5 mW, **(d)** saturation beam at +0.8 ps and 20 mW. Pump and probe powers were kept at 5 mW and 1 mW, respectively. Data is normalized respect to the non-saturated one. The colored data points in each graph represent the direct ratio between saturated and non-saturated data sets. The shaded areas highlight the found position of the saturation pulse.

The dependence of the saturation efficiency on the saturation pulse delay was also studied using the second signal acquisition modality, and the results are shown in **Figure 4.15(b)**. The data represents the normalized pump-probe residual signal (at time zero) obtained at different delays of the saturation pulse and for saturation powers ranging from 5 to 20 mW. Pump and probe beams were kept at 5 mW and 1 mW, respectively.

It can be seen that the maximum depletion efficiency is always achieved when all three beams are temporally superimposed at time zero. The power dependence is more pronounced at time zero, where stronger depletion is achieved at higher power. Moving towards negative or positive delays the difference in depletion efficiency at different power gradually diminishes, highlighting a weaker power dependence.

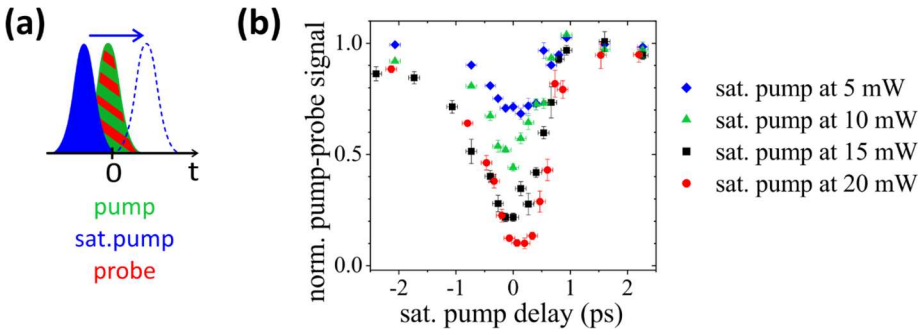

Figure 4.15 (a) Pulse sketch of the second experimental acquisition modalities to investigate the depletion efficiency at different saturation pulse delays in SLG. The pump pulse is drawn in striped green, the probe pulse in red, and the saturation pulse in blue. The temporal position of the pump pulse defines the time zero. **(b)** Pump-probe signal depletion obtained with the acquisition modality explained in **(a)**, and varying the saturation power from 5 to 20 mW, while keeping pump and probe powers fixed at 5 mW and 1 mW, respectively. The error bars on the x-axis reflect the error in moving and placing the manual delay line in the saturation pump optical path (see **Section 4.2**).

Power dependence. The power dependence of the saturation efficiency can be better understood by direct acquisition of the depletion curves at fixed delays of the saturation pulse (**Figure 4.16**), and fitting them with the function derived from Wang et al. [85]

$$\frac{\Delta T_{sat}}{\Delta T_{unsat}} = \frac{1}{1+\frac{P_{sat}}{P_0}} \qquad (4.1)$$

where $\Delta T_{sat}/\Delta T_{unsat}$ is the pump-probe signal fraction due to the saturation effect, P_{sat} is the power of the non-modulated saturation pump beam, and P_0 is the saturation power at which the pump-probe signal is dropped to half. P_0 is a characteristic parameter of the sample and can be used to evaluate the depletion efficiency of the process: the lower the value of P_0, the higher the saturation efficiency. Data was acquired keeping the pump beam at 5 mW and the probe beam at 1 mW.

By keeping the saturation pulse temporally aligned with pump and probe pulses at time zero (**Figure 4.16(b)**), a value of P_0 = (4.2 ± 0.2) mW was retrieved, corresponding to a pump average power density of 1.3 MW/cm^2. This value is comparable with the saturation power value we obtained from graphs in **Figure 4.9**.

With the saturation pulse delayed by -0.4 ps P_0 increases to (15 ± 1) mW (**Figure 4.16(a)**), while at 0.8 ps delay P_0 increases up to a value of (42 ± 2) mW (**Figure 4.16(c)**). Additionally, this confirms that the depletion efficiency is the highest when the saturation beam is superimposed with pump and probe beams, while it rapidly decreases with the saturation delay.

The absorption saturation due to the non-modulated pump beam proves to be efficient in the signal suppression only if it happens within the sub-picosecond lifetime of the excited state in order to avoid state relaxation and probe absorption. Therefore, the temporal alignment of

the saturation pulse at the time zero needs to be set with a precision of the order of the system temporal resolution to guarantee optimized saturation performances.

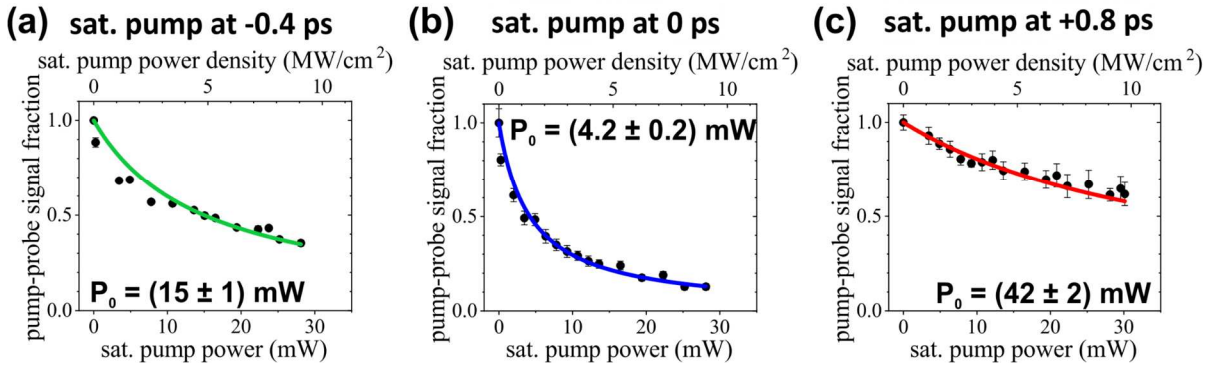

Figure 4.16 Absorption saturation depletion curves, which demonstrate the degree of signal suppression as a function of the saturation power and at different time delays between saturation and pump pulses: **(a)** -0.4 ps delay, **(b)** 0 ps delay, **(c)** +0.8 ps delay. The probe beam was kept temporally aligned with the pump one for maximum signal collection. The exponential decay of the depletion curves was fitted with **equation 4.1**.

To further demonstrate the temporal delay dependence of the saturation efficiency, pump-probe images of sub-resolved graphene defects were acquired with overlapped pump and probe pulses and with the superimposition of the **doughnut-shaped** saturation beam (**Figure 4.17(a-c)**). The pump beam was kept at 5 mW, while the probe beam at 1 mW. The saturation beam was kept at 5 mW and moved to different delays as shown in **Figure 4.17(f)**. The obtained images were compared with the conventional pump-probe data set acquired in the same conditions but in the absence of the saturation beam (**Figure 4.17(d)**). To evaluate the performance, the intensity line profiles for each condition were taken along the indicated arrows and they are shown in **Figure 4.17(e)**. When the saturation pulse is delayed with respect to the pump and probe pulses (**Figure 4.17(a,c)**) the saturation power is insufficient to saturate the absorption, in agreement with the depletion curves in **Figure 4.16(a,c)**, and the line profiles (green and red) do not show resolution enhancement. On the contrary, when the delay is at zero (**Figure 4.17(b)**), the saturation power is sufficient to induce saturation effects on the crest of the doughnut beam, which results in a narrowing of the intensity peaks (blue line profile in **Figure 4.17(e)**).

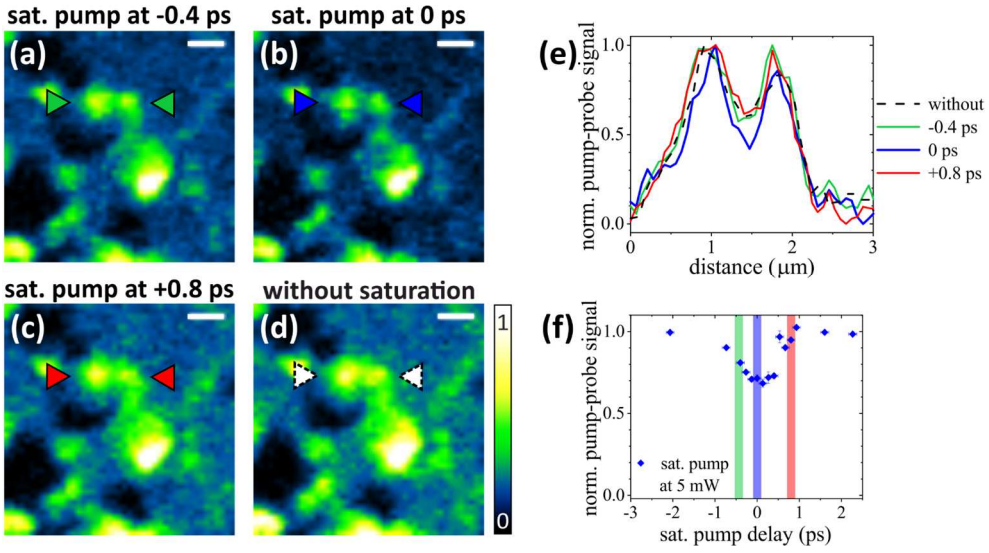

Figure 4.17 (a-c) Saturated images of SLG defects acquired with doughnut-shaped saturation pump beam at 5 mW and at different time delays (-0.4 ps, 0 ps and +0.8 ps) respect to the pump beam. The probe beam was kept temporally aligned to the pump one for maximum signal collection. **(d)** The same graphene defect imaged without the doughnut beam and in the same conditions as **(a-c)**. The calibration bar applies to all the images. Scale bar 1 μm. **(e)** Line profiles across the arrows in **(a-d)**. **(f)** Saturation efficiency graph at 5 mW, highlighting the experimental conditions used to obtain images in **(a-c)**.

4.4.3. Super-resolution imaging of SLG at single layer sensitivity

After defining the optimal conditions for absorption saturation and suppression of the pump-probe signal, super-resolved imaging of SLG defects was performed using the **doughnut-shaped** saturation beam.

The probe pulse was placed at time zero for maximum signal generation, and the saturation pulse was also placed at time zero to maximize signal suppression in the doughnut region.

The saturation power was kept around 15-20 mW to obtain a signal suppression of about 80-90%. No sample damage was observed using these powers.

Some examples of standard pump-probe images (PP) and saturated pump-probe images (SPP) of SLG samples are presented in **Figure 4.18**, and normalized line profiles along the direction of the arrows are compared.

Figure 4.18(a) was acquired with pump at 1 mW, probe at 2 mW and saturation pump at 20 mW. Two line profiles (I and II) along two graphene multilayer regions are presented and show an increase in the level of detail in the saturated case (red profiles).

Figure 4.18(b) was acquired with pump at 2 mW, probe at 0.4 mW and saturation pump at 14 mW. The SPP image permits to access more sample information, because it clearly shows that the bright graphene fold is composed by two parts that couldn't be distinguished in the conventional PP image.

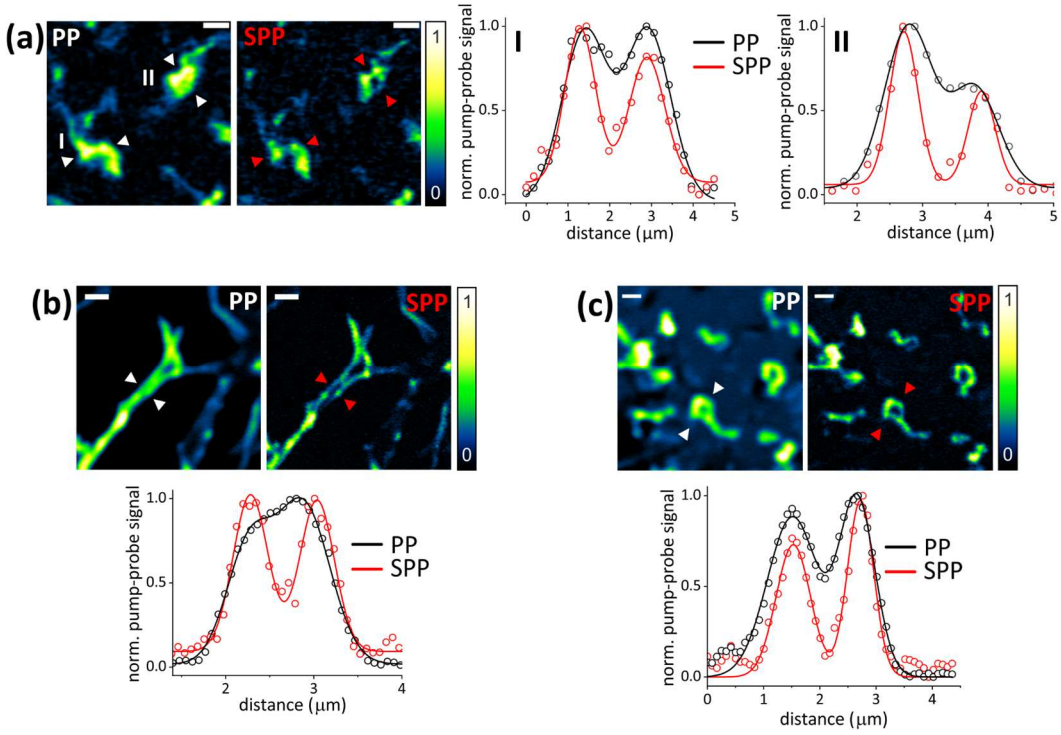

Figure 4.18 Normalized pump-probe (PP) and saturated pump-probe (SPP) images of SLG folds and defects. The normalized non-saturated (black dots) and saturated (red dots) line profiles across the arrows are compared, and the profiles retrieved through Gaussian fitting are shown (solid lines). Scale bar 2 μm. Acquisition parameters: **(a)** pump at 1 mW, probe at 2 mW, saturation pump at 20 mW; **(b)** pump at 2 mW, probe at 0.4 mW, saturation pump at 14 mW; **(c)** pump at 2.5 mW, probe at 0.4 mW, saturation pump at 20 mW.

Figure 4.18(c) was acquired with pump at 2.5 mW, probe at 0.4 mW and saturation pump at 20 mW. It shows a complex structure in the SLG, where a single layer covers the majority of the field of view with a uniform signal. Folds created by multiple graphene layers produce stronger signals throughout the sample, while no signal is detected from cracks and holes in the structure. Comparing PP and SPP images it can be noted that the saturated modality produces a decrease in the overall SLG signal intensity, together with significant resolution enhancement.

Other SLG imaging examples are shown in **Figure 4.19**.

In **Figure 4.19(a)** the single layer is imaged with high SNR using the pump beam at 5 mW and the probe beam at 1 mW. Two hexagonal-shaped multilayer defects are visible, together with holes and folds in the uniform signal. When applying the doughnut-shaped saturation beam at 20 mW (SPP image), the SNR diminishes but the single layer signal does not entirely disappear. Moreover, the outlines of the multilayer regions result more defined in the SPP image. The line profiles along the graphene fold highlight the increase in resolution reporting the FWHM of the Gaussian fits: (580 ± 30) nm in the PP image and (300 ± 30) nm in the SPP image.

Figure 4.19(b) was acquired with pump at 6 mW, probe at 1.5 mW and saturation pump at 15 mW. Through the saturation approach, a multilayer defect is resolved as composed of two subunits, as shown in the line profiles. Looking at the signal intensity along the line profiles, both curves exhibit zero signal in correspondence with the hole, a maximum signal (normalized to 1) in correspondence with the double multilayer defect, and an additional half signal (with 0.5 amplitude after the normalization). These regions are resolved with higher lateral resolution, and the quantization of the signal with respect to the number of layers is preserved. The spatial resolution enhancement was quantified through the FWHM of the Gaussian fits. A resolution improvement of almost two-fold is achieved for a graphene structure, which shows a width of (860 ± 40) nm when imaged with the conventional pump-probe approach (PP), compared with a width of (480 ± 40) nm obtained with the superimposition of the doughnut-shaped saturation beam (SPP).

Another achievement of the saturated technique was the improvement in the sensitivity of the number of layers, as shown in **Figure 4.19(b)**. Looking at the line profiles, the super-resolved image of the SLG defect (SPP) demonstrates an additional middle layer (red arrow), a detail that is completely hidden in the diffraction-limited image (PP). In **Figure 4.20** the quantification of the number of layers composing this additional structure was achieved.

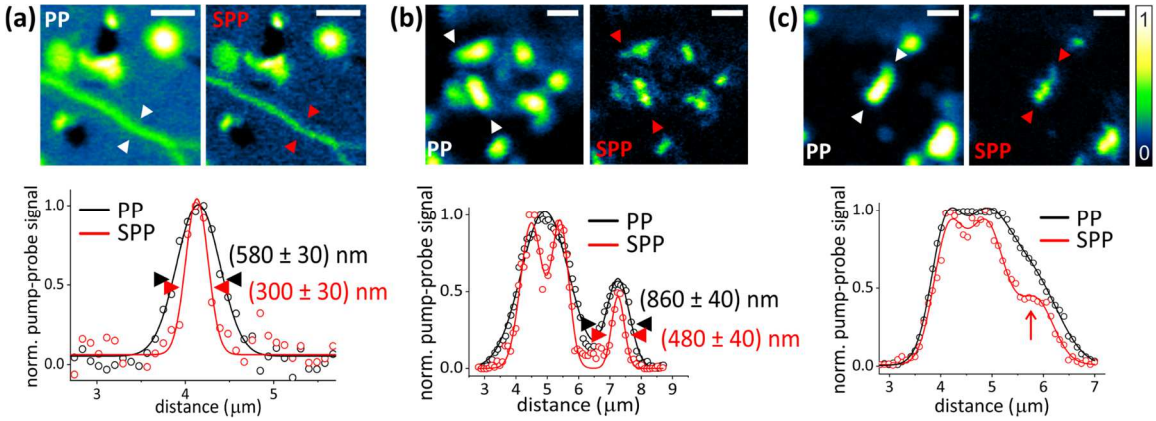

Figure 4.19 Normalized pump-probe (PP) and saturated pump-probe (SPP) images of SLG folds and defects. The normalized non-saturated (black dots) and saturated (red dots) line profiles across the arrows are compared, and the profiles retrieved through Gaussian fitting are shown (solid lines). Scale bar 2 μm. Acquisition parameters: **(a)** pump at 5 mW, probe at 1 mW, saturation pump at 20 mW; **(b-c)** pump at 6 mW, probe at 1.5 mW, saturation pump at 15 mW. In the graphs in **(a)** and **(b)** the FWHM values of the Gaussian fits are reported to highlight the resolution improvement. In the graph in **(c)** the arrow points the improvement in layer sensitivity with the saturated technique.

In order to count the number of layers, the signal intensity detected from the single layer needs to be first quantified. In fact, as previously discussed (**Section 4.4.1**) the pump-probe intensity is proportional to the number of graphene layers. In **Figure 4.20(a)** a larger view of the sample containing the details shown in **Figure 4.19(b-c)** is presented. The area zoomed in

Figure 4.20(b) is chosen to identify the signal correspondent to the single layer which surrounds the hole. The line profiles drawn across the hole border (along the dashed arrows) are fitted with a sigmoidal function and values of (500 ± 10) a.u. and (150 ± 10) a.u. are retrieved for the single layer signal intensity in conventional pump-probe imaging conditions (PP) and in presence of the doughnut-shaped saturation beam (SPP), respectively. Looking at the line profiles in **Figure 4.20(c)** (the same as the ones in **Figure 4.19(c)** but here non-normalized), the newly appeared middle layer (marked by the red arrow in the graph) exhibits a signal intensity of (820 ± 20) a.u. (horizontal red line in the graph). Dividing this value by the single layer intensity calculated from **Figure 4.20(b)**, the defect results to be composed by (5.5 ± 0.4) layers. If multiplying this number of layers for the signal intensity of the single layer in the PP image, the defect results to have a signal intensity of (2700 ± 200) a.u. which is shown in the graph as black horizontal lines (the solid line is the middle value while the dashed lines represent the error). This intensity appears to correspond to a small step in the line profile of the defect, marked by the black arrow.

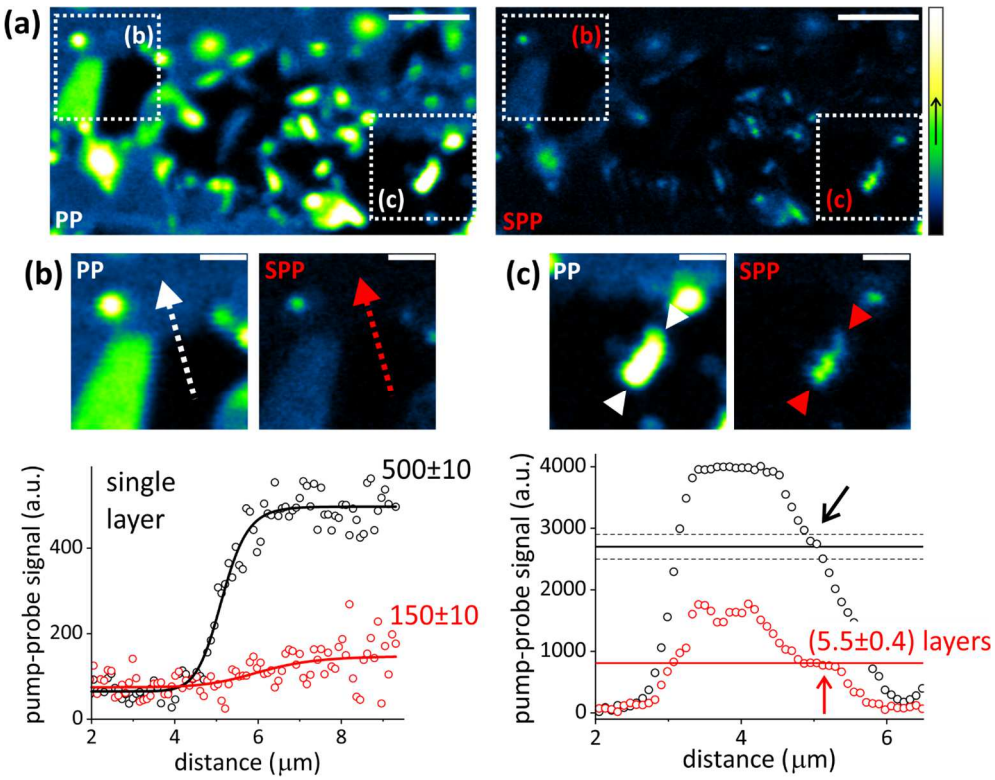

Figure 4.20 (a) Non-normalized large view PP and SPP images of the sample presented in **Figure 4.19(b-c)**. Scale bar 5 μm. The contoured areas are zoomed in **(b)** and **(c)**. Notice that **(c)** is the same region as in **Figure 4.19(c)**. **(b)** Calculation of the signal intensity of the single layer. The sigmoidal profiles across the hole border (dashed arrows) retrieve signal intensities of 500±10 (a.u.) and 150±10 (a.u.) for the single layer imaged in PP and in SPP configurations, respectively. Scale bar 2 μm. (c) The same region as in **Figure 4.19(c)**. Scale bar 2 μm. The non-normalized line profiles are compared and are used to quantify the number of layers.

4.4.4. Multimodality

The pump-probe optical system realized for these experiments also allows for 3D and multimodal imaging. Both fluorescence and pump-probe channels are available to have multiple contrast and multiple information, and the piezo stage permits the acquisition of volumetric stacks.

In **Figure 4.21** some examples are reported. Pump and probe wavelengths were tuned to 800 nm and 1030 nm, respectively. Fluorescence signal collected in a confocal geometry with open pinhole and over all the visible spectrum is shown in magenta, pump-probe signal collected and demodulated in transmission is shown in cyan.

In **Figure 4.21(a)** hair images are shown. On the top row, longitudinally images acquired on the surface and 10 µm deep are presented. The external cuticular cells exhibit a bright autofluorescence signal coming from keratin, and their arrangement in flakes is visible. The internal components of the hair can be clearly seen in the pump-probe channel. Probably the contrast is given by the highly absorbing pigment melanin which is contained in the elongated cortical cells which constitute the inner layers. The image of a transversal section of the hair, cut with a microtome, is also shown. Autofluorescence from the internal cells is also present in the magenta channel, together with the dotted pump-probe signal. On the bottom row, a volume of a small hair portion is rendered.

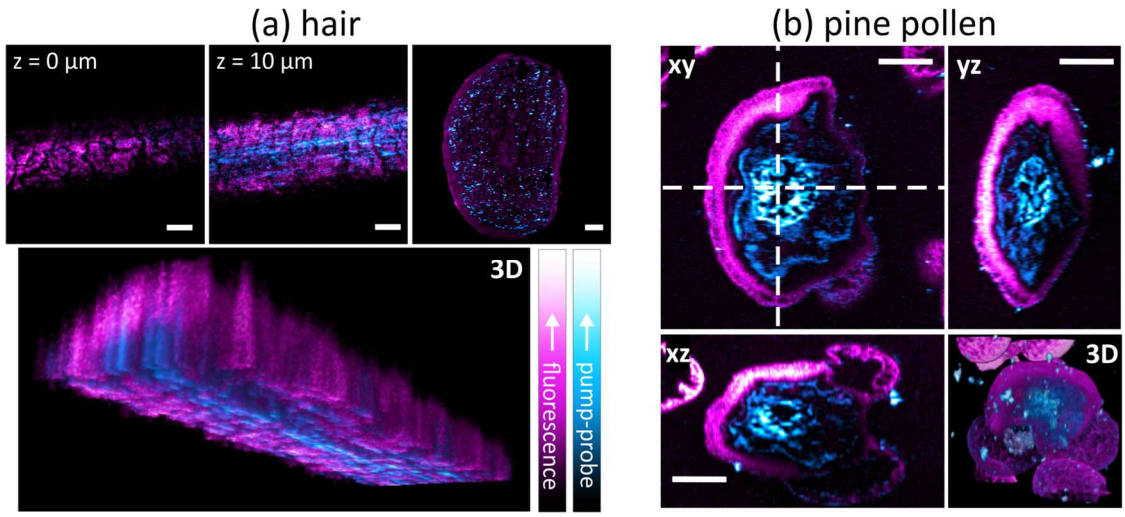

Figure 4.21 (a) 3D and multimodal images of a hair. Autofluorescence signal is shown in magenta, pump-probe signal in cyan. In the top row two longitudinal images acquired on the surface and 10 µm deep, and a transversal image of a hair section are presented. Scale bar 10 µm. In the bottom row the volume rendering of a small portion of the hair is shown. **(b)** 3D and multimodal images of a pine pollen grain. Autofluorescence signal is shown in magenta, pump-probe signal in cyan. The sections along the dashed lines and the total volume rendering are shown. Scale bar 10 µm.

In **Figure 4.21(b)** pine pollen grain images are shown. Transversal sections along the dashed lines and volume rendering (bottom right corner) are also presented. Endogenous autofluorescence in plant tissues arises from a variety of biomolecules, including lignins, chlorophyll, carotene, and xanthophyll. Highly absorbing species are present in the pollen body, giving a strong pump-probe contrast.

More interestingly, it was checked the applicability of this 3D multimodal setup for giving insights in the study of cells-graphene interactions, and in particular of neurons-graphene interactions for the development of neural prosthetics and biosensors [176,177].

Typically, in an ordinary experiment, Raman spectroscopy is used to check the correct transfer of the SLG on the coverglass: time-consuming Raman spectra are acquired in a limited number of regions of the sample and their peaks are evaluated. After that, cultured neurons are deposited on the SLG surface, they are stained with fluorescent labels and imaged under a fluorescence microscope in order to follow the growth of their neural network, to study their morphology or to check the neural activity with electrophysiological investigations [177]. Fluorescence signal will be generated only from the cells, while graphene will remain dark and no direct correlation between cells and graphene structure can be easily accessed. During the preparation and the transfer, SLG may result not perfectly homogeneous, but with a more complicated structure, with cracks, holes, multilayer defects and folds, as previously shown (see **Section 4.4.1**). It is impossible to have a complete understanding of the SLG structure just with Raman spectra acquired on a limited number of regions. Having a system in which both graphene and cells are imaged and monitored at the same time and in short time could on one side simplify and accelerate the experiments, and on the other access new correlative information.

With the pump-probe setup here presented, it is possible to achieve in short time high-contrast imaging of SLG, together with two-photon excited fluorescence imaging of cells. Being a multiphoton microscope, label-free contrast can be achieved and autofluorescence from endogenous cellular components, mainly NADH, can be collected when exciting with 800 nm. This permits on one side to shorten the time required for the full experiment avoiding the time-consuming staining protocols, and on the other to decrease the invasiveness.

Figure 4.22(a) shows fixed mouse neuroblastoma (N2a) cells, whose nuclei are marked with DAPI, imaged on top of a SLG. Pump and probe wavelengths were tuned to 800 nm and 1030 nm, respectively. Autofluorescence, mainly excited by the 800 nm beam and coming from the whole cell body, is also present in the fluorescence channel (green), together with the strong DAPI fluorescence. The pump-probe channel (red) highlights the graphene structure, which presents bright folds and dark cracks. Such a multimodal image, which covers a FOV of about 50×50 μm^2 can be obtained in roughly 5 seconds, and all the sample can be explored and rapidly imaged moving the translational stage.

In **Figure 4.22(b)** volumetric imaging of fixed unstained N2a cells on SLG is presented. The wavelengths were kept as the previous experiments and the powers were kept as low as possible, 6 mW for the pump and 1.5 mW for the probe. Only autofluorescence signal is collected in the green channel. The xy images are presented as average intensity projection (AIP) along the z-stack. In the first image on the left the xz section along the dashed line is presented. In the second image the maximum intensity projection (MIP) of the xz sections delimited by the dotted lines is presented, in order to highlight the dendrite (arrow). Finally, a volume rendering is shown. Also in this case the structure of SLG is well visible and in principle can be correlated with the cells distribution and growing behavior.

A 3D multimodal pump-probe microscope with multiphoton fluorescence detection capabilities results to be a useful tool for label-free correlative studies involving non-fluorescent SLG (or in general graphene-based materials) and cells. Such a non-linear setup allows for an additional channel (pump-probe) which broadens the available contrast mechanisms beyond fluorescence.

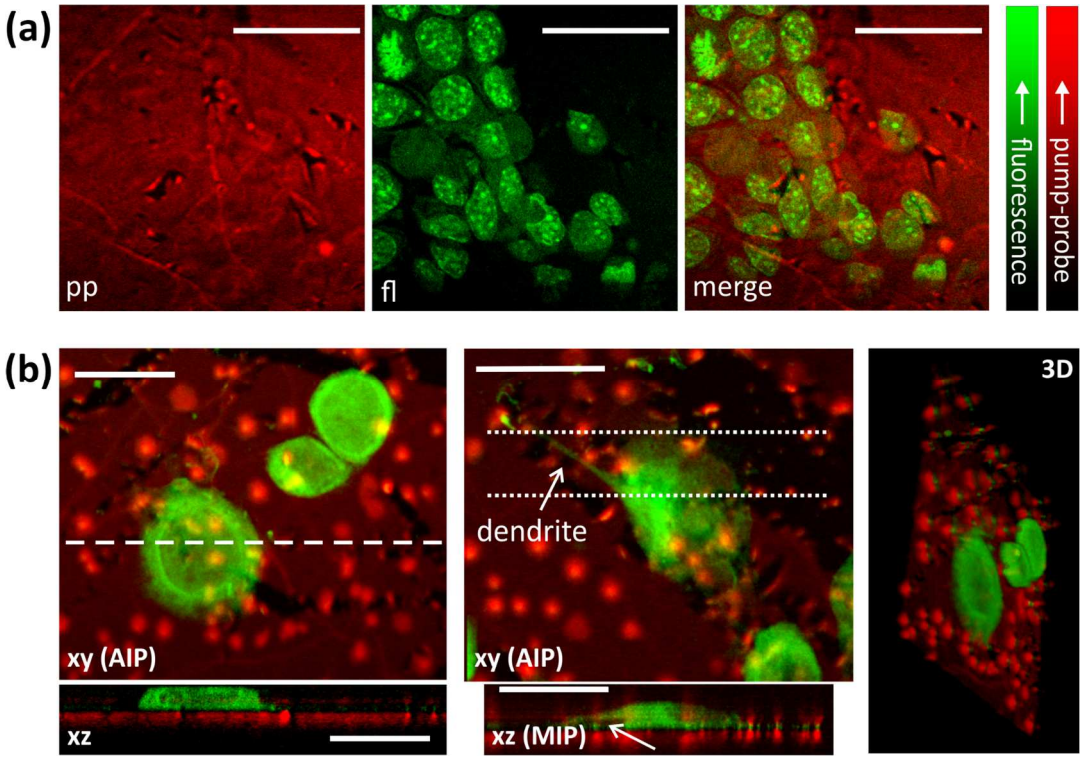

Figure 4.22 (a) Fixed mouse neuroblastoma (N2a) cells stained with DAPI imaged on top of SLG. The fluorescence (fl) channel is shown in green, the pump-probe (pp) in red. Scale bar 20 µm. **(b)** Volumetric imaging of fixed unstained N2a cells. Xy images are shown as average intensity projections (AIP) along the respective z-stacks. The xz section along the dashed line is also presented. The xz sections contained in between the dotted lines in the central image are shown as maximum intensity projection (MIP). Scale bar 20 µm. A 3D rendering is also shown on the right.

4.4.5. Higher-order pump-probe imaging[1]

When imaging core-shell CdSe/CdS NCs with pump at 800 nm and probe at 1020 nm, the interaction of the beams led to both fluorescence and pump-probe signals.

Fluorescence emission must result from multiphoton absorption of NIR photons, since the absorption spectrum of CdSe/CdS NCs is in the visible spectral range [168]. This is confirmed by the power curves presented in **Figure 4.23(a)**, where the fluorescence signal is plotted as a function of pump and probe powers separately. The fits of the data retrieve a behavior higher than linear, suggesting the presence of multiphoton phenomena. The non-linearity is more pronounced with the probe excitation, presumably due to its longer wavelength which allows for a more efficient two-photon absorption.

The pump-probe power curves shown in **Figure 4.23(b)** reflect a similar behavior compared to the fluorescence ones. Fixing the probe power at 8 mW, the pump-probe signal increases as a function of the pump power with a power of about 1.5. Fixing the pump power at 6 mW, the pump-probe signal increases with a higher power of about 2.5 as a function of the probe power.

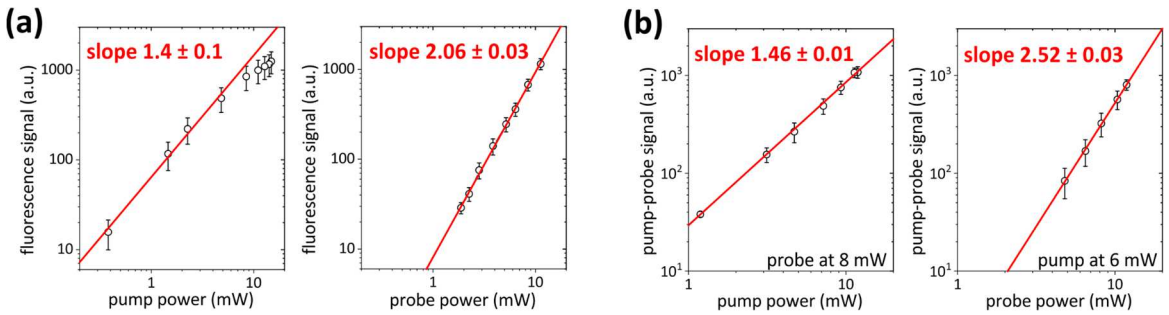

Figure 4.23 (a) Log-log plots of the CdSe/CdS NCs fluorescence intensity as a function of pump (left) and probe (right) powers. Linear fits are shown as a solid red line. **(b)** Log-log plot of the CdSe/CdS NCs pump-probe intensity as a function of pump (left) and probe (right) powers. Linear fits are shown as a solid red line.

In **Figure 4.24**, fluorescence and pump-probe images of a layer of NCs is shown. Both modulus R and in-phase component X of the demodulated pump-probe signal are presented. The contrast in the in-phase image is negative, correspondent to an anti-phase interaction like two-photon absorption (TPA) or excited state absorption (ESA). This means that the probe beam is absorbed together with the pump one in order to allow for the transition to the excited state, or it is subsequently absorbed by the excited state.

[1] The results reported in this section were acquired in collaboration with Dr. Fumihiro Dake (Nikon Corporation, Japan) and presented by him at the conference Optics & Photonics Japan (2017).

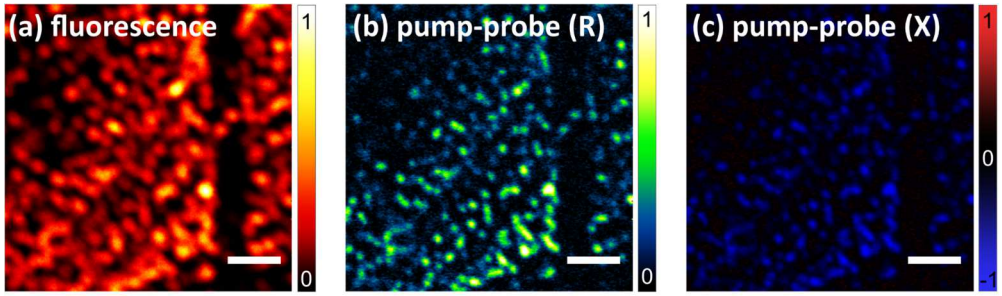

Figure 4.24 (a) Fluorescence and **(b-c)** pump-probe images of CdSe/CdS NCs. Both modulus R **(b)** and in-phase component X **(c)** of the pump-probe signal are shown. Scale bar 2 μm.

Moreover, as shown in **Figure 4.23(b)**, the process should involve at least two probe photons, causing higher-order pump-probe phenomena different from the second-order conventional ones which involve one pump and one probe photon. The increase in non-linearity should allow for a more confined excitation volume, a consequent higher background suppression and higher spatial resolution compared to the two-photon fluorescence signal. This can be seen in the images in **Figure 4.25**, in which fluorescence and pump-probe line profiles along NCs are compared, revealing a better optical resolution. The NCs separation is more evident in the pump-probe images. Moreover, a 2-fold increase in spatial resolution is achieved as shown in graph III.

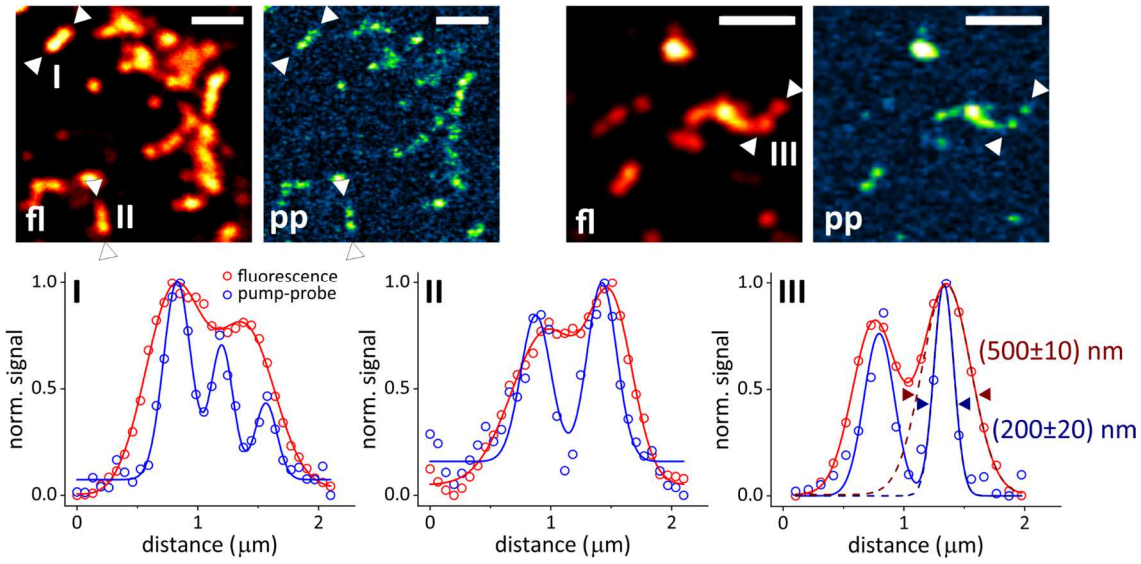

Figure 4.25 Comparison between two-photon fluorescence and pump-probe images of CdSe/CdS NCs. Scale bar 2 μm. Line profiles along the direction marked by the white arrows (I, II, III) are plotted, fitted with multi-peak Gaussian functions and compared. Fluorescence signal is shown in red, pump-probe signal in blue.

This was a preliminary experimental test which aimed at evaluating the resolution of the pump-probe technique, which has yet to be sufficiently assessed. It appears that pump-probe microscopy may possess better optical resolution than two-photon fluorescence, especially when higher-order non-linear phenomena contribute to signal generation.

4.5. Conclusions

In this work, a custom-made multimodal NIR pump-probe microscope was presented. The setup is based on an OPO pumped by a femtosecond Ti:sapphire laser, whose output pump and probe pulses are spatially and temporally overlapped in order to investigate the carrier population of the structures of interest.

Graphene-based samples (single-layer graphene and few-layers graphene and graphene oxide flakes) were successfully characterized with this setup, and they resulted in sharing similar properties. The peculiar absorption properties of graphene permit to use NIR wavelengths to study its excited state dynamics via ground state depletion (GSD) non-linear absorption mechanisms. High SNR imaging with single layer sensitivity is achieved in short exposure times. **Equation 3.1** was demonstrated in these samples. At low powers regime, the pump-probe signal is linear respect to the applied powers, while around 2 $MWcm^{-2}$ it starts to saturate. The signal intensity results also to be linear respect to the number of graphene layers. Spectroscopic studies could be performed with sub-picosecond temporal resolution, and they revealed a graphene excited state dynamics characterized by two timescales. The fastest one is in the 100-fs timescale, while the slowest one falls in the picosecond timescale and it is shorter in multilayer regions.

In addition, the generalized RESOLFT concept, widely exploited in fluorescence nanoscopy, was implemented in the pump-probe setup in order to achieve label-free sub-diffraction imaging capabilities. In particular, the pump absorption saturation was identified as the optimal transition to be exploited for this purpose, using a non-modulated doughnut-shaped saturation beam.

The saturation properties and the consequent suppression of the pump-probe signal were extensively studied in SLG. The suppression efficiency was shown to be exponentially dependent on the applied power, which can be kept as low as few $MWcm^{-2}$ (10-20 mW). Since graphene exhibits an ultrafast excited state dynamics, also the temporal alignment of the saturation pulse plays a key role in obtaining efficient signal suppression at low powers. The precise temporal overlap between the pulses is a critical point for achieving maximum efficiency, as a displacement of the order of the system temporal response dramatically decreases the signal suppression capabilities. The demonstrated ability to minimize the illumination powers by optimizing the temporal overlap is especially important for imaging samples with low damage threshold and opens the possibility to use this technique for biological studies.

The engineering of the saturation beam in a doughnut shape permitted to achieve a resolution improvement over two-fold with limited applied powers and to increase the information content on the graphene defects structure. The saturation-based technique keeps

the quantization of the pump-probe signal with the number of layers, increasing not only the spatial resolution but also the layer sensitivity.

Moreover, it appears that pump-probe microscopy may possess better optical resolution than two-photon fluorescence, especially when higher-order non-linear phenomena contribute to pump-probe signal generation.

The presented results demonstrate the great potential of the pump-probe technique. Its high sensitivity, chemical specificity and high temporal and spatial resolution **open the path to imaging of a variety of non-fluorescent chromophores and nanomaterials**, which were previously inaccessible. Moreover, **the saturated pump-probe technique gives access to higher spatial information beyond the diffraction limit and it can be applied in principle to any samples showing a known saturable absorption transition**.

With the implementation of NIR illumination, saturated pump-probe microscopy opens up the possibility to image in scattering media and tissues, and to be integrated into a multimodal non-linear microscopy platform with intrinsic sectioning capabilities, together with 2PEF, SHG, and SRS label-free techniques, in order to broaden its use in biology and material sciences.

5. Saturated Stimulated Raman Scattering microscopy @ LASIE (Osaka)

This research was carried out in a 5-months period in the Prof. Fujita group at Laboratory for Scientific Instrumentation and Engineering (LASIE) at the Department of Applied Physics of Osaka University, Japan (http://lasie.ap.eng.osaka-u.ac.jp/home.html).

A custom microscopy setup, used to obtain the results presented inside this chapter, was entirely designed and realized at the Photonics Center at Osaka University (http://www.parc.osaka-u.ac.jp/en/) by Dr. Hiroyuki Kawagoe, Kota Koike and me, under the supervision of Prof. Katsumasa Fujita. Experiments and data analysis were planned and performed by Dr. Hiroyuki Kawagoe, Kota Koike and me, under the supervision of Prof. Katsumasa Fujita. Dr. Ryosuke Oketani and Prof. Nicholas Isaac Smith contributed to the results with useful discussions.

These results were presented in Japanese symposia (GNP 2017, JSLM 2018, JSAP Spring meeting 2018) and international conferences (ELMI 2018).

5.1. Aim

The Ph.D. research on the applicability of super-resolution approaches based on saturation phenomena for super-resolution label-free pump-probe imaging was completed with the implementation of a saturated stimulated Raman scattering (SRS) microscope.

The SRS microscopy technique was presented in **Section 3.4**, and it is becoming of widespread use for label-free imaging of small biomolecules due to its stronger signal and higher SNR compared to other Raman-based techniques. Since NIR light is used for sample illumination, SRS microscopy provides relatively poor spatial resolution and axial sectioning compared to other types of optical microscopy using visible light, and the challenge of spatial resolution improvement is still open.

The method suggested here to achieve super-resolution SRS imaging is based on the application of the differential saturated excitation (dSAX) concept, introduced **in Section 2.3.2**. In principle, the non-linear response caused by SRS signal saturation (see **Section 1.2.2**) can be used to get access to higher spatial frequencies and to shrink the effective PSF, as it was already demonstrated in fluorescence [44] and in CARS [87] microscopy.

This small project aimed at a preliminary demonstration of the applicability of SAX for super-resolution SRS imaging, and it was developed through the achievement of the following goals:

1. Design and realization of a custom SRS microscope (**Section 5.2**).
2. Theoretical simulations of the SRS saturation curve and of the dSAX approach to check the applicability of the technique and the expected outcome in terms of resolution improvement (**Section 5.4.1**).
3. Preliminary experiments on diamond particles and PMMA beads to check the performance of the setup and of the non-linearity extraction algorithm (**Section 5.4.2**).

5.2. Optical setup

The custom SRS microscope setup (**Figure 5.1**) is realized combining two mode-locked picosecond pulsed laser beams (Nd:VAN pump HighQ picoTRAIN™, 76 MHz, 6 ps, Spectra Physics) with an inverted Nikon Eclipse Ti microscope body. The picoTRAIN™ output at 1064 nm is used as Stokes beam. The second frequency-doubled output at 532 nm is coupled to an optical parametric oscillator (OPO, Levante Emerald, APE GmbH) whose tunable output (700-980 nm) is used as pump beam. The Stokes beam is modulated at 2 MHz with an acousto-optic modulator (AOM, 3080-197, Crystal Technology Inc.) driven by a function generator (specs). The beam is focused with a lens (L) in the AOM crystal and then re-collimated at the output with a lens whose adjustable position on the optical axis can be exploited to control the axial position of the focus at the sample plane. The two laser beams are spatially combined with a dichroic beamsplitter (SP1000, Asahi Spectra USA Inc.) and their pulses are temporally synchronized using a manual delay line inserted in the pump optical path. The illumination spot is created through a 60× 1.2NA water immersion objective (UPlanSApo, Olympus) and it is scanned in the focal plane with a pair of galvanometric mirrors. The polarization of both beams is set to vertical using two linear polarizers, and the power of the beams is controlled with two half-wave plates in front of the polarizers.

The transmitted beams are collected by an objective identical to the excitation one, and then they are spectrally filtered by two identical bandpass filters (FF01-850/310-25, Semrock) in order to select only the pump beam. A fast photodiode (DET36A, Thorlabs) connected to a lock-in amplifier (LIA, SR844, Stanford Research Systems) referenced to the AOM frequency is used to extract the SRS signal as a loss of pump photons (stimulated Raman loss, SRL). The amplitude R of the signal is used as preferred LIA output.

To further increase the detection efficiency, the detector output is electrically filtered by a low-pass (EF526, 15 MHz low pass filter, Thorlabs), a band-pass (KR2792-2-BNC, 2 MHz bandpass filter, KR Electronics), and a high-pass (EF517, 1 MHz high pass filter, Thorlabs) filter before the LIA.

A non-descanned epi-fluorescence detection path is added to the setup, in order to have a tool for beam alignment and an additional channel for multimodal imaging. The emission is separated from the excitation before the illumination objective using a dichroic beamsplitter (FF746-SDi01-25x36x3.0, Semrock), and the fluorescence is additionally filtered (FF01-750/SP-25, Semrock) and collected by a photomultiplier tube (H7422-40, Hamamatsu).

The scanning and the imaging acquisition are controlled using a data acquisition board (DAQ) and a custom made software written with LabVIEW (NI), while the images are analyzed with ImageJ/Fiji (NIH) [162].

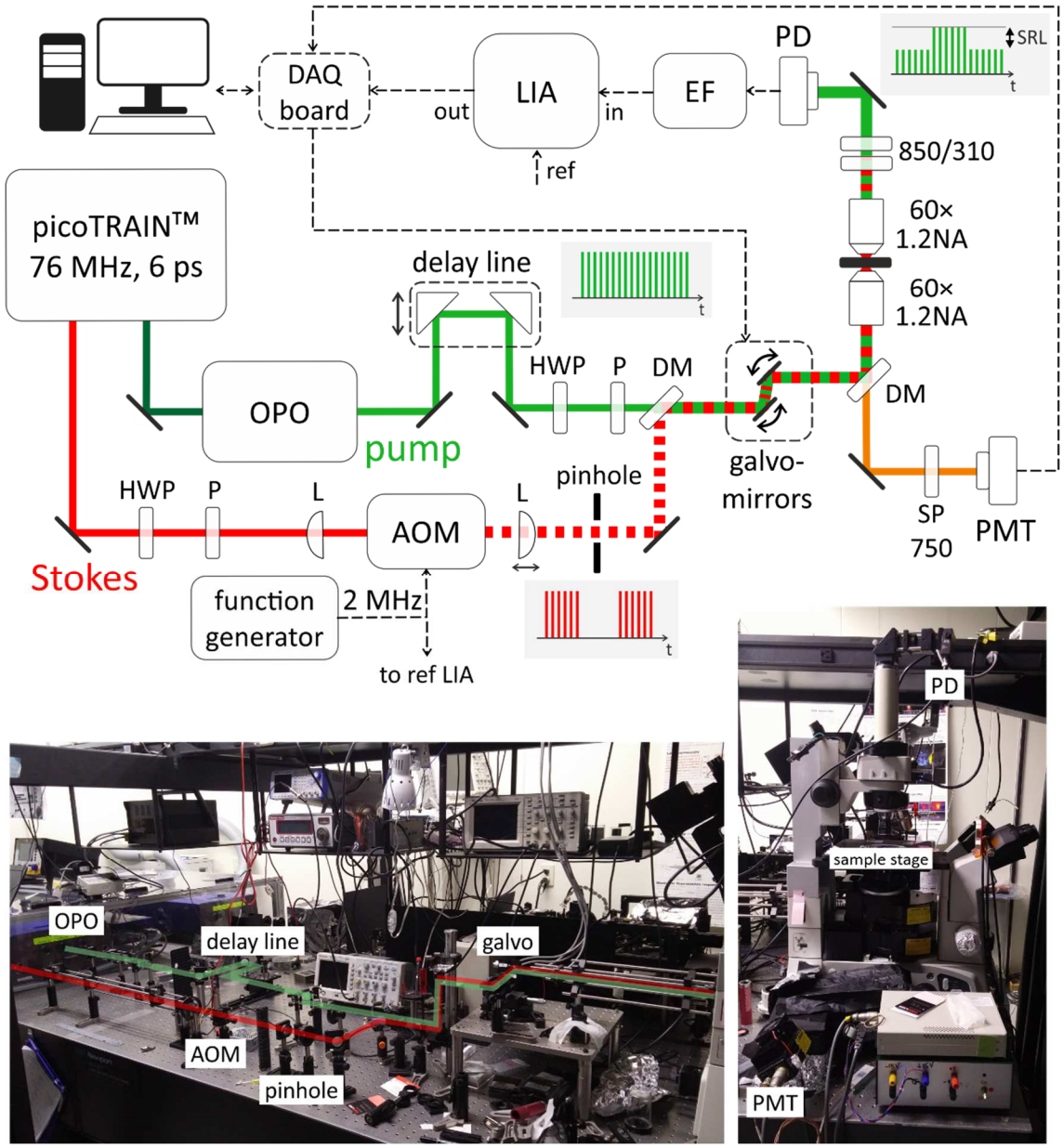

Figure 5.1 Custom SRS optical setup built in the Photonic Center at Osaka University. The pump beam optical path is shown in green, the Stokes one in red. OPO: optical parametric oscillator, HWP: half-wave plate. P: linear polarizer, L: lens, AOM: acousto-optical modulator, DM: dichroic mirror, PMT: photomultiplier tube, SP: short-pass filter, PD: photodiode, LIA: lock-in amplifier, EF: electrical filter, NA: numerical aperture, DAQ: data acquisition, SRL: stimulated Raman loss, ref: reference, in: input, out: output. Inset pulse diagrams show the high-frequency modulation scheme which allows for SRL detection.

5.2.1. Custom software and FOV calibration

The layout of the LabVIEW-based custom software is presented in **Figure 5.2(a)**. Through this software the imaging parameters can be set (on the left), the image is reconstructed and visualized live (middle) and it can be saved (on the right). The scanning of the laser beam is controlled setting separately the initial and the final output voltages for the two x and y galvo-

mirrors, and the number of steps (i.e., pixels) they need to do inside the defined voltage range. The rest position of the galvo mirrors is set to 0 V, which means that positive and negative voltages can be applied. In order to relate the applied voltage to a length dimension, a micrometer calibration grid with 10 µm spacing between reflective lines is imaged in **transmission** (**Figure 5.2(b)**). A scanning range $\Delta V = 2\,V$ results to cover all the accessible FOV of the system. The calibration of the scanning system was done as follows:

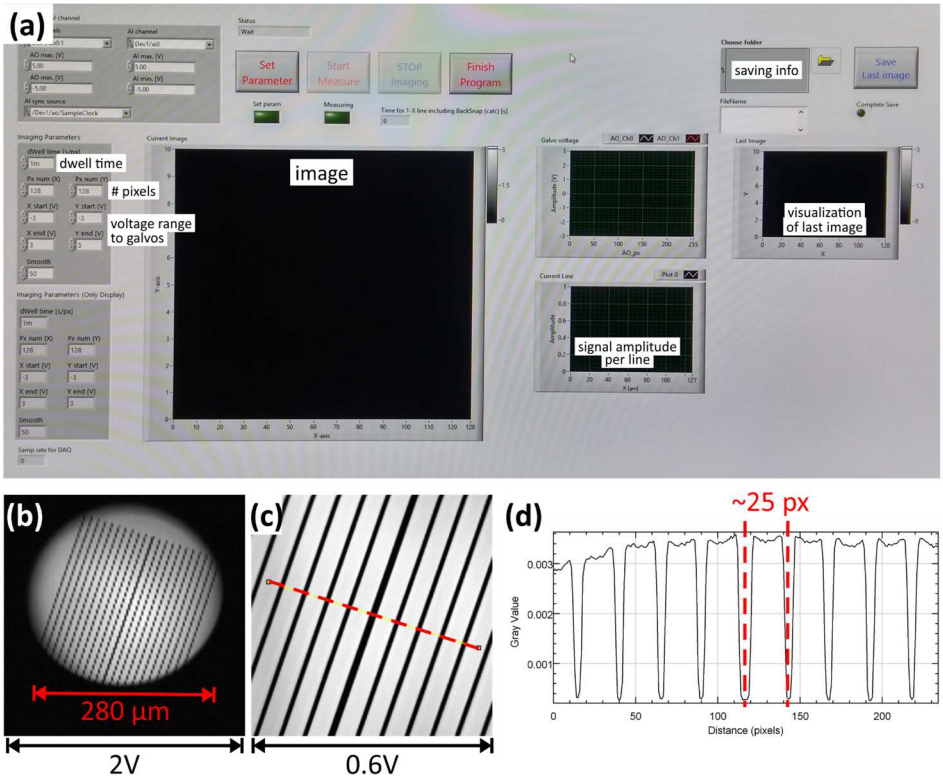

Figure 5.2 (a) Custom microscope software written in LabVIEW. The main controls are highlighted in the image: imaging parameters setting on the left, image visualization in the middle, image saving on the right. **(b)** Transmission image of the calibration grid sample with voltage range of the galvos set to 2 V on both direction. All the achievable FOV is imaged, and, after the calibration, it results to be 280 µm wide. **(c)** Zoom image of the calibration grid, setting the galvos range to 0.6 V on both directions. **(d)** Line profile along the dashed line in **(c)**, needed for the calibration of the scanning parameters.

- knowing the scanning range of the image expressed as voltage and the number of pixels used, the amount of volts per pixel is calculated. In **Figure 5.2(c)** the scanning range is $\Delta V = 0.6\,V$ in both directions, and 256×256 pixels were used. This means that the volts per pixel are $\frac{0.6\,V}{256\,px} = 0.0023\,\frac{V}{px}$;
- plotting the line profile across different grid lines (see **Figure 5.2(d)**) and fitting them to find the central positions, the spacing between the lines in *number of pixels* is calculated (~25 pixels);

- knowing the nominal distance between lines in micrometer (10 µm in this case), the previously calculated average distance in number of pixels, and the previously calculated V/px coefficient, the calibration factor (CF) in µm/V, needed to convert the voltage in a distance value, is calculated: $CF = \frac{10\ \mu m}{25\ px \times 0.0023 \frac{V}{px}} \sim \mathbf{174}\ \frac{\boldsymbol{\mu m}}{\boldsymbol{V}}$.

The CF depends on the microscope itself and must be recalculated if changing the illumination objective. With this factor, FOV and pixel size can be retrieved as

$$FOV = \Delta V \times CF$$
$$pixel\ size = \frac{FOV}{\#pixels} = \frac{\Delta V \times CF}{\#pixels} \qquad \textbf{(5.1)}$$

The maximum achievable FOV in transmission (**Figure 5.2(b)**) is about 280 µm in diameter.

5.2.2. Stokes modulation

The high-frequency modulation of the Stokes beam is achieved through an AOM driven by a function generator. A sine wave at 2 MHz is sent as input signal to the modulator (**Figure 5.3**, magenta signal). The modulated laser beam is detected after the AOM with a fast photodiode (DET10A, Thorlabs) and the signal is visualized with an oscilloscope to check the quality of the modulation (**Figure 5.3**, green signal). In principle, the bandwidth of the detector is enough to see the single Stokes pulse at 76 MHz, but the oscilloscope is not triggered on the pulse repetition rate but on the modulation frequency.

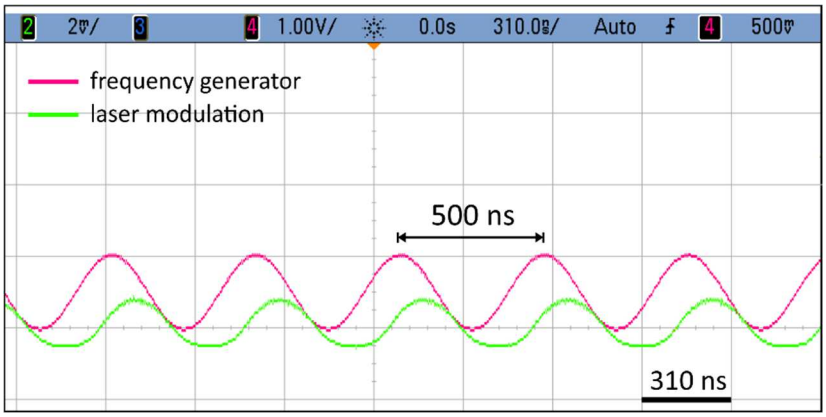

Figure 5.3 Oscilloscope screenshot showing the 2-MHz sinusoidal wave at the frequency generator output used to drive the AOM and as reference for the lock-in (magenta signal), and the resultant modulated laser beam at the output of the AOM (green signal).

After a proper alignment of the AOM respect to the input beam, a diffraction efficiency $DE = \frac{P_1(on)}{P_0(off)} \sim 80\%$ (where $P_1(on)$ is the AOM output beam power at the first diffraction order when the AOM is on, and $P_0(off)$ is the AOM output power when the AOM is off) and a modulation depth $MD = \frac{V_{pk-pk/2}}{V_{ave}} \sim 94\%$ (where V_{pk-pk} and V_{ave} are the peak-to-peak

amplitude and the average value of the AOM output, respectively, as detected with a fast photodiode and seen with an oscilloscope) are achieved. The DE parameter defines the available Stokes power at the objective: the higher DE, the higher the power. The MD parameter defines the quality of the modulation, which will be transmitted to the detected signal and will affect its effective demodulation by the lock-in.

5.2.3. Spatial alignment

The superimposition of pump and Stokes focal spots at the sample plane is achieved combining the two beams with a dichroic mirror (DM), while their axial alignment is done changing the focal position of the Stokes beam with a lens after the AOM in order to match the focal position of the pump.

The beam alignment is performed imaging 200-nm orange fluorescence beads dispersed on a coverglass (**Figure 5.4**). Being the pump beam tunable in the range 700-980 nm to match the vibrational resonance of interest, a change in wavelength will also cause a change in the alignment due to chromatic aberrations. It was checked that the alignment done at 803 nm persists at 816 nm, but it is lost at 932 nm.

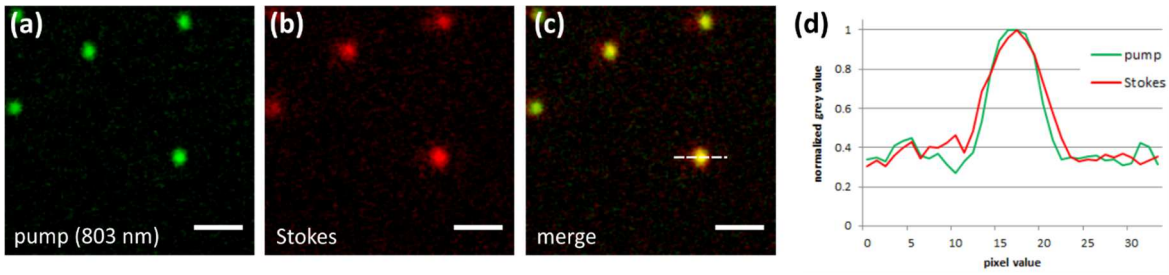

Figure 5.4 Fluorescence images of 200-nm orange beads acquired with **(a)** pump beam tuned to 803 nm and **(b)** Stokes beam. The merge of the two images **(c)** shows the superimposition of the two beams on the sample plane. Intensity profiles are shown in **(d)**.

5.2.4. Pulses characterization and temporal alignment

The temporal alignment of pump and Stokes picosecond pulses can be checked and adjusted using an autocorrelator (Model 409, Spectra Physics). Moving the delay line in the pump optical path, the appearance of the SFG signal at wavelength $\frac{1}{\lambda_{SFG}} = \frac{1}{\lambda_p} + \frac{1}{\lambda_s}$ is verified at the output of the autocorrelator, due to the simultaneous interaction of both pulse on the non-linear crystal contained in the instrument.

While aligning, also the quality of the pulses can be checked with an oscilloscope connected to the autocorrelator output (), and their width can be calculated. First, the time scale of the

oscilloscope needs to be calibrated using an etalon with a known thickness which will delay the pulses of a known quantity (20 ps in this case). Second, the autocorrelation width can be extracted from the Gaussian fit of the pulses. Since theoretical models of ultrafast lasers often predict $sech^2$ pulse shapes, the autocorrelation width is divided by 1.54 to obtain a better pulse width estimation. The values obtained for these laser beams are about 6.5 ps and 13 ps for pump and Stokes pulses, respectively.

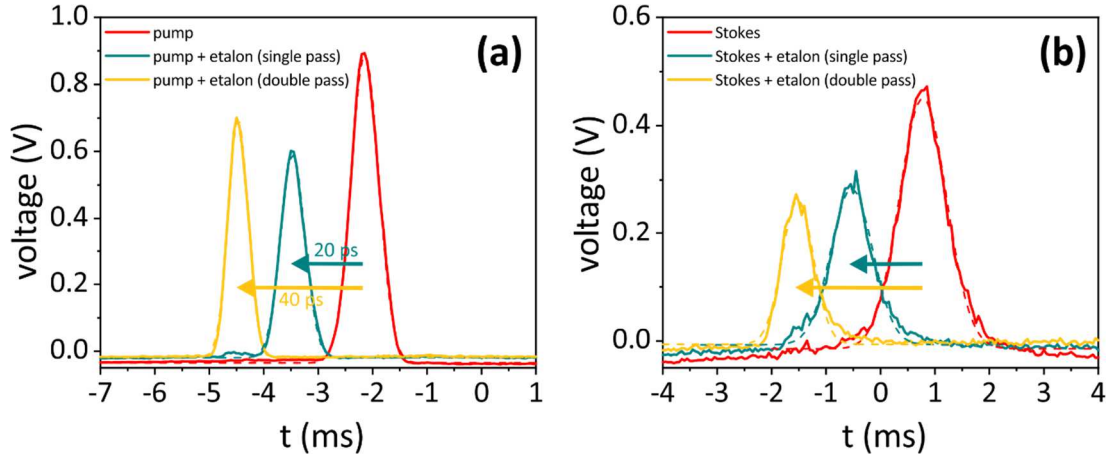

Figure 5.5 Autocorrelator traces of pump **(a)** and Stokes **(b)** pulses as recorded with the oscilloscope (red traces). In order to measure the pulse width, the temporal scale of the oscilloscope (in ms) needs to be calibrated in picoseconds. This is done inserting an etalon which will delay the pulses of 20 ps (blue traces) and of 40 ps (yellow traces). In this example the calculated calibration factor is 18 ps/ms.

5.3. Samples

The dSAX approach was applied to SRS imaging of

(i) diamond powder (3-5 μm size, IRM, Tomei Diamond), tuning the pump wavelength to **932 nm** to excite the vibrational resonance at 1332.5 cm^{-1}. This sample was also used as a model for some preliminary theoretical simulations that will be presented in paragraph 5.4.1;

(ii) Poly(methyl methacrylate) (PMMA) beads (1-10 μm mixture), tuning the pump to **810 nm** to excite the resonance at 2946 cm^{-1}.

Preliminary experimental results using these samples are presented in **Section 5.4.2**.

5.4. Results and discussion

5.4.1. Theoretical simulations

The applicability of the dSAX method to SRS imaging was first checked through simulations using Matlab (MathWorks). The theoretical model of SRS signal generation and saturation, presented in section 1.2.2, was applied to nanodiamonds imaging in order to derive their **SRS saturation curve**. Moreover, applying the dSAX algorithm, the **amount of non-linear signal** due to saturation and the **effective PSF** under saturated imaging conditions were calculated. The optical parameters of nanodiamonds necessary for the computation were taken from [87,178] and are listed in **Table 5.1** together with the imaging parameters. The imaging parameters were chosen as the ones available with the custom-made experimental setup presented in **Section 5.2**.

nanodiamonds optical parameters		
resonance vibrational frequency	ω_v	$2\pi c \times 1332.5\ cm^{-1}$
bandwidth of the Raman line	Γ	$2\pi c \times 1.7\ cm^{-1}$
molecular number density	N	$1.762 \times 10^{23}\ cm^{-3}$
Raman scattering differential cross-section	$\frac{\partial \sigma_{Raman}}{\partial \Omega}$	$2.7 \times 10^{-29}\ cm^2$
imaging parameters		
pump frequency	ω_p	$\frac{2\pi c}{931.88\ nm}$
Stokes frequency	ω_s	$\frac{2\pi c}{1064\ nm}$
numerical aperture	NA	1.2
pulse width	t_p	$7\ ps$
refractive index (water)	n	1.333

Table 5.1 Optical and imaging parameters used for simulations.

SRS saturation curve. The plot of the simulated SRS intensity $|\Delta T_{SRS}|$ as a function of the applied powers I_p and I_s is presented in **Figure 5.6**, and it was calculated following the theory summarized in **Section 1.2.2**:

$$\left|\Delta T_{SRS}(I_p I_s)\right| \propto \chi_I^{(3)res}\, I_p\, I_s \qquad \textbf{(5.2)}$$

with

$$\chi^{(3)\ res}(\omega) = \frac{2Nc^4}{\hbar\omega_s^4}\left(\frac{\partial \sigma_{Raman}}{\partial \Omega}\right)\frac{\omega_v\, \Delta N}{\omega_v^2 - (\omega_p - \omega_s)^2 - i\Gamma(\omega_p - \omega_s)} \qquad \textbf{(5.3)}$$

and

$$\begin{cases} \Delta N(t_p) \propto e^{-t_p/\tau_{\Delta N}} \\ \frac{1}{\tau_{\Delta N}} = -2\left(\frac{4\pi c}{\hbar\omega_s^2}\right)^2\left(\frac{\partial\sigma_{Raman}}{\partial\Omega}\right)\frac{\Gamma}{4\left(\omega_v-(\omega_p-\omega_s)\right)^2+\Gamma^2}\, I_p\, I_s \end{cases} \quad (5.4)$$

The SRS signal intensity exhibits a linear behavior (slope equal to 1 in the log-log plot in **Figure 5.6**) at low power densities, while it starts to saturate at higher power levels. Around 10^{12} W^2cm^{-4} the signal response starts to deviate from linearity, as can be seen in the inset zoomed graph in **Figure 5.6**, reaching a saturation plateau around 10^{14} W^2cm^{-4}.

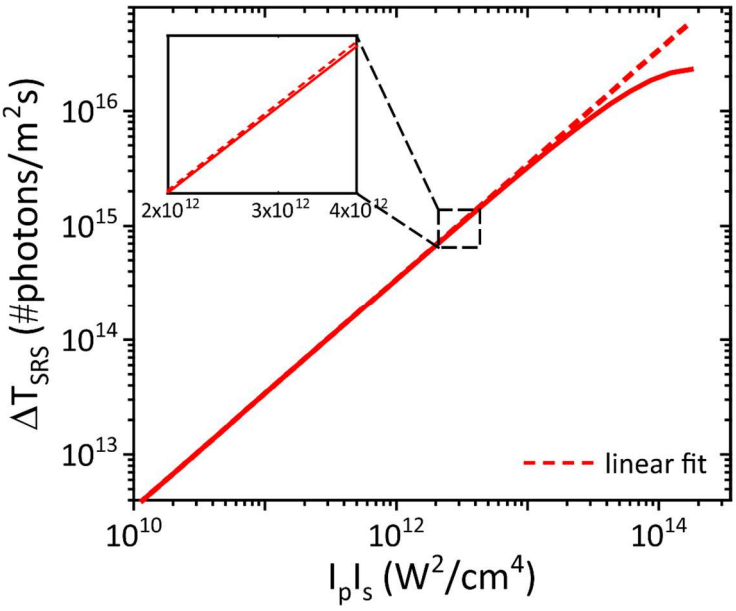

Figure 5.6 Log-log plot of the simulated SRS response of nanodiamonds as a function of the applied power densities product (solid line). A linear fit (slope equal to 1) was performed on the first data points.

Non-linear signal extraction. Starting from the simulated SRS saturation curve (**Figure 5.6**), the amount of second- and third-order non-linearities were calculated with the dSAX method presented in **Section 2.3.2**, and they are plotted as a function of the applied powers in **Figure 5.7**. These non-linearities account for the saturation phenomenon.

The second-order non-linearity (solid green line) was calculated as $\Delta T_{NL}^{(2)} = \Delta T_L - \Delta T_{SRS}$ and it starts to appear around 10^{10} W^2cm^{-4}, acquiring its typical quadratic behavior respect to the applied power.

The third-order non-linearity $\Delta T_{NL}^{(3)}$ (solid blue line) was calculated as the deviation of $\Delta T_{NL}^{(2)}$ respect to the second-order linear fit (dashed green line) and it starts to appear at higher powers, around 10^{13} W^2cm^{-4}.

In the same way, higher order components can be extracted from the SRS signal, but they will be relevant at even higher powers.

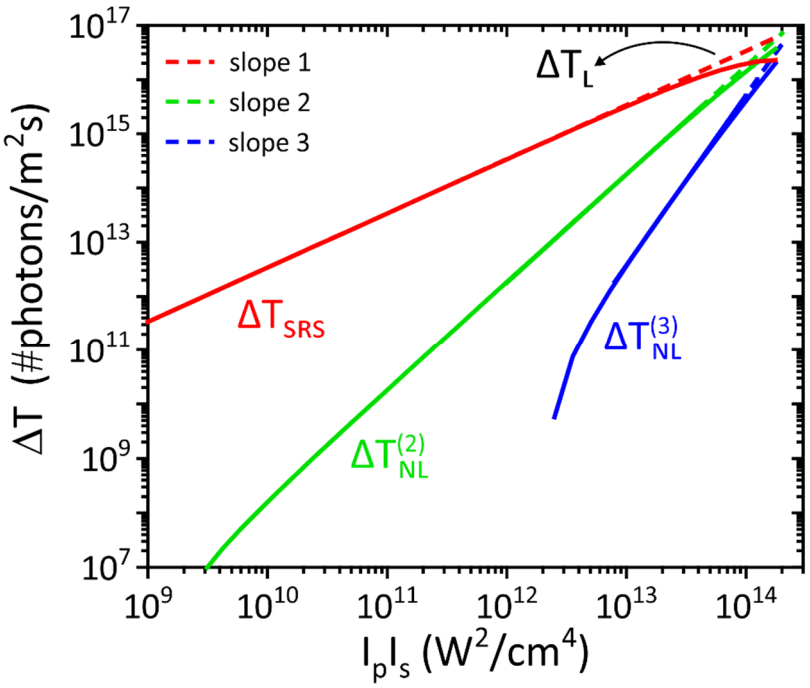

Figure 5.7 Log-log plots of the second- and third-order non-linear components (green and blue solid lines, respectively) of the SRS signal (red solid line). Linear, quadratic and third-order fits are also shown (red, green and blue dashed lines, respectively).

Noise evaluation. The dSAX method is based on the choice of two signals ΔT_1 and ΔT_2 acquired at two different power levels I_1 and I_2 (here for simplicity of writing $I \equiv I_p I_s$) in order to extract the second-order non-linearity $\Delta T_{NL}^{(2)}$ which appears under saturation conditions

$$\Delta T_{NL}^{(2)}(I_2) = \Delta T_L(I_2) - \Delta T_2(I_2) = \left(\frac{I_2}{I_1}\right)\Delta T_1(I_1) - \Delta T_2(I_2) \qquad \textbf{(5.5)}$$

The number of required signals multiplies according to the order of the non-linearity that wants to be extracted (see **Section 2.3.2**). The choice of the two conditions will affect the noise level of the extracted non-linear signal. Since in super-resolution imaging a good level of SNR is required, a study on the noise behavior as a function of the chosen parameters is necessary.

Starting from the noise on the detected SRS signal, which was approximated as *shot noise* and calculated as the *square root of the signal*, and applying error propagation rules, the noise on the second-order extracted signal was calculated at various conditions. In **Figure 5.8(a-c)** results are graphed. The SRS signal is plotted as a solid red curve, while the extracted second-order non-linear signal as a solid green curve. Since a log-log plot is used, only the '+' component of the noise is represented on top of the data as a shaded area. The noise of the detected SRS signal is too small to be seen. The two power levels I_1 and I_2 chosen for the differential approach are reported for each graph. In (b), I_2 was increased respect to the condition in (a) from 10^3 W^2cm^{-4} to 10^6 W^2cm^{-4}, without any consequent change in the noise

amount of the second-order component. In (c), I_1 was increased respect to the condition in (b) from 1 W^2cm^{-4} to 10^5 W^2cm^{-4}, leading to a remarkable decrease in the noise level. This means that the choice of I_1 governs the SNR of the super-resolution image reconstructed with the second-order component, and that higher powers are desirable for high SNR.

The same calculations were performed for the extraction of the third-order non-linearity $\Delta T_{NL}^{(3)}$, as explained in [64]. Results are shown in **Figure 5.8(d-f)**, where the SRS signal is still drawn as a red solid curve and the extracted third-order component as a blue solid curve. In this case, three powers I_1, I_2 and I_3 are required in the differential approach, and they were varied according to the values reported under each graph. In (e), I_2 was increased respect to the condition in (d) from 10^8 W^2cm^{-4} to 10^{10} W^2cm^{-4}, leading to a remarkable decrease in the noise level (blue shaded area). In (f), I_1 and I_3 were increased respect to the conditions in (e), I_1 from 10^5 W^2cm^{-4} to 10^6 W^2cm^{-4} and I_3 from 10^{11} W^2cm^{-4} to 5×10^{12} W^2cm^{-4}, without bringing any variation in the noise level. This means that only the choice of I_2 governs the SNR of the super-resolution image reconstructed with the third-order component, and that higher powers are desirable for high SNR.

In conclusion, the extraction of the non-linearities using power levels as high as possible, but below the saturation level, is desirable in order to keep a high SNR in the image.

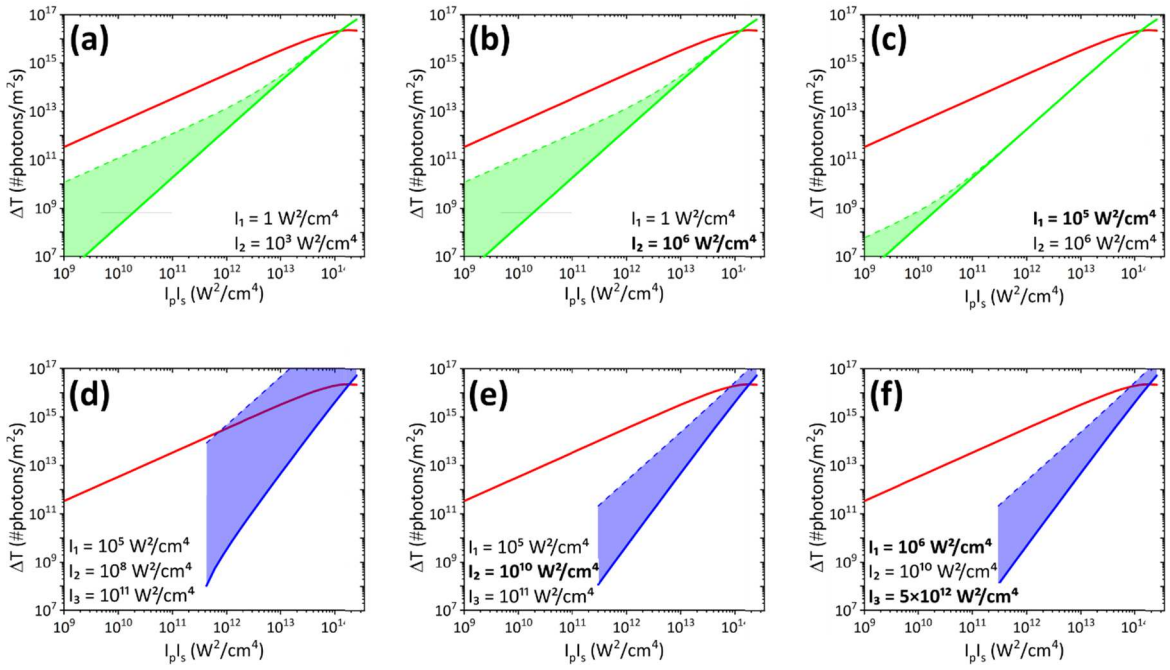

Figure 5.8 (a-c) Noise evaluation in second-order non-linearity extraction using different power conditions as reported. The simulated SRS signal is shown as a solid red line, the calculated second-order component as a green solid line, and the noise as a shaded area on top of the curve. **(d-f)** Noise evaluation in third-order non-linearity extraction using different power conditions as reported. The simulated SRS signal is shown as a solid red line, the calculated third-order component as a blue solid line, and the noise as a shaded area on top of the curve.

Effective PSF calculation. In order to confirm the improvement in lateral and axial resolution when applying the dSAX method to SRS imaging, effective PSFs were simulated at different Gaussian excitation intensity distributions $I_1(x,y,z), I_2(x,y,z), \dots$ using the same SRS models and the same parameters as the ones used for the previous simulations. In this case, the SRS signal intensity is calculated not as a function of power but as a function of the spatial coordinates. The PSFs were calculated for an excitation objective of NA 1.2, water immersion ($n = 1.333$), like the one used in the experimental setup, and using a 256×256 matrix covering a FOV of 4×4 μm^2 (0.015625 μm/px). In **Figure 5.9**, the normalized PSFs calculated at different power levels (intended as $I_p I_s$) are shown and their profiles along the dashed line are compared. As the excitation power increases, the PSF becomes broader due to saturation effects, as seen in fluorescence [56]. The broadening effect is more prominent for powers higher that 10^{12} W^{2}cm^{-4}, where saturation effects start to become important.

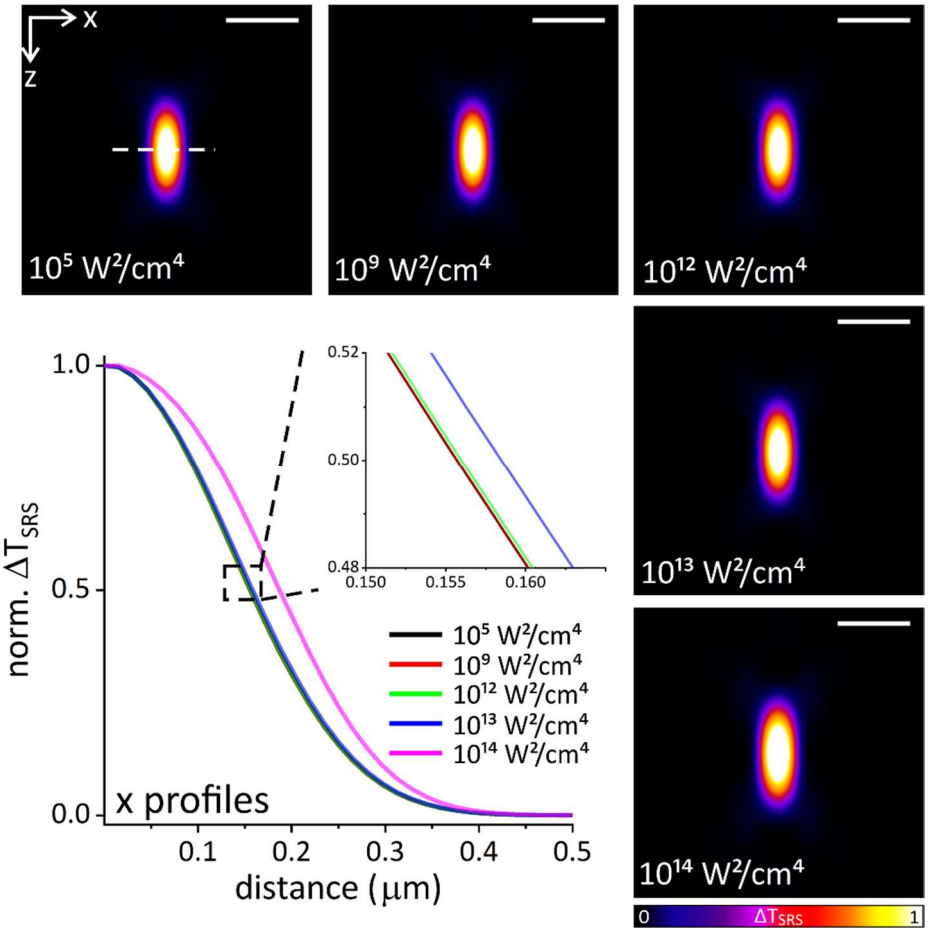

Figure 5.9 Normalized PSFs calculated at different power levels, as reported in each image. Scale bar 1 μm. Line profiles along the dashed line are also shown, highlighting the broadening due to saturation effects.

When the dSAX algorithm is applied to two excitation conditions, the obtained PSF results to be smaller confirming the fact that the extracted non-linearity is concentrated at the center

of the focal spot where saturation effects are more prominent. The dSAX approach results to be effective also for super-resolution SRS imaging.

In **Figure 5.10** the PSFs at excitation intensities I_1 and I_2, and the calculated dSAX PSF are shown, together with the line profiles along the x and z directions. The FWHM of the Gaussian profiles shows a **1.3-fold** resolution improvement in all directions applying the dSAX method.

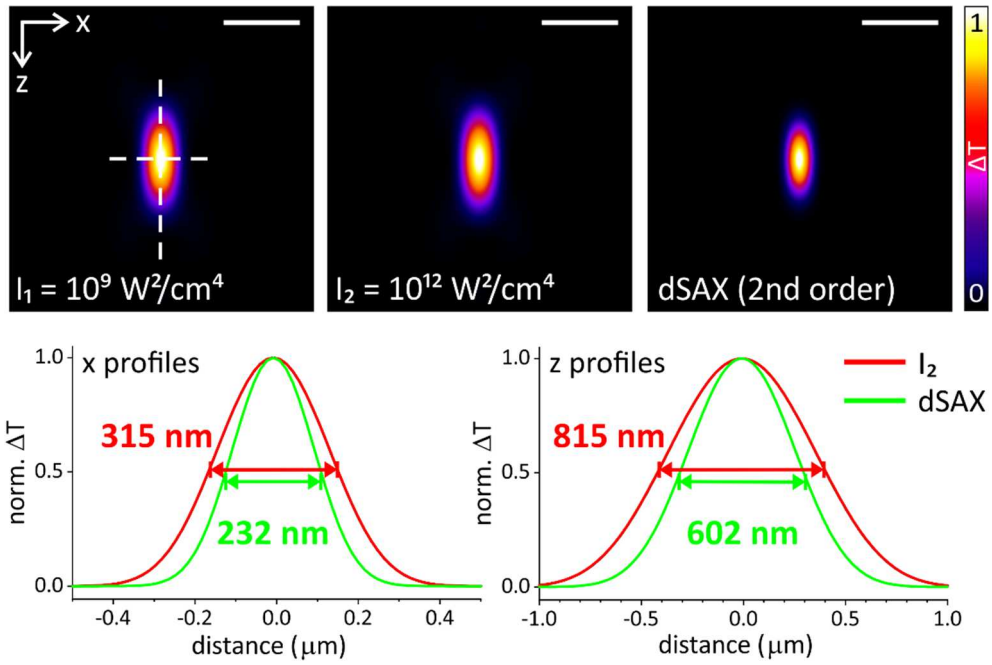

Figure 5.10 Simulated normalized PSFs at 10^9 W^2cm^{-4} and 10^{12} W^2cm^{-4}, and the calculated second-order dSAX normalized PSF. Scale bar 1 μm. Line profiles along the dashed lines are also shown, and the FWHM are reported, which confirm the applicability of dSAX for super-resolution SRS microscopy.

Raman spectrum. In the application of modulated SAX (mSAX) to CARS imaging of nanodiamonds, Yonemaru et al. [87] also achieved, both theoretically and experimentally, a spectral resolution improvement. This is seen as a reduction of the width of the Raman peak centered on the resonance at 1332.5 cm^{-1}. The same study was simulated for the differential SAX (dSAX) applied to SRS imaging, to see if the same improvement can be achieved. The results are presented in **Figure 5.11**, where the same calculation parameters used in **Figure 5.10** are used. As can be seen, a **1.7-fold** spectral resolution improvement is also achieved with dSAX applied to SRS imaging.

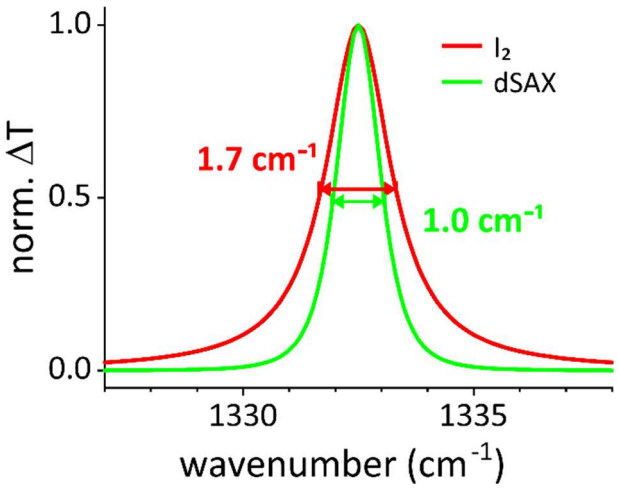

Figure 5.11 Simulated Raman peak around the diamond resonance at 1332.5 cm^{-1}, calculated for $I_2 = 10^{12}$ W^2cm^{-4} and after applying the dSAX at the second-order using $I_1 = 10^9$ W^2cm^{-4}.

5.4.2. Experimental results

Both the saturation of the SRS signal and the applicability of the dSAX approach for increasing spatial resolution were checked for diamond and PMMA particles.

Diamond particles. The main results of diamond imaging are shown in **Figure 5.12**. Images were acquired at different powers between 10^{13}-10^{14} W^2cm^{-4}. In **Figure 5.12(a)** the SRS signal is plotted as a function of the applied powers, which exhibits a linear behavior at lower powers, as highlighted by the red dashed fitting, and a marked saturation close to 10^{14} W^2cm^{-4}, as in the simulated curve (**Figure 5.6**). The images acquired at the powers I_1=4.2×10^{13} W^2cm^{-4} and I_2=1.2×10^{14} W^2cm^{-4} are shown in **Figure 5.12(b)** and they were used to extract the second-order non-linearity and build the dSAX image with improved resolution. Images were acquired using 128×128 pixels and a pixel dwell time of 200 µs. The areas of the image marked with white dashed squares are presented enlarged in **Figure 5.12(c-d)**, and the normalized line profiles along the directions marked by the white arrows are drawn and compared. The profile of the diamond particle in **Figure 5.12(c)** exhibits a decrease in its width after applying the dSAX method. Gaussian fits were performed on the data (dashed lines in the graph) and the obtained FWHM values are reported in the table. The FWHM increases from (2.0 ± 0.1) µm to (2.2 ± 0.1) µm when increasing the applied power, as a consequence of the broadening of the PSF induced by saturation phenomena (see **Figure 5.9**). Applying the dSAX method, the width decreases to (1.3 ± 0.1) µm revealing a smaller-sized particle and allowing for a 1.7-fold resolution enhancement. Even if the dimension of the main particle is not sub-diffracted, the resolution improvement is still visible, probably because the contribution of sub-diffracted

particles around it decreases. The detail in **Figure 5.12(d)** shows an agglomerate of smaller particles, and the separation between two of them becomes more evident when applying the dSAX method.

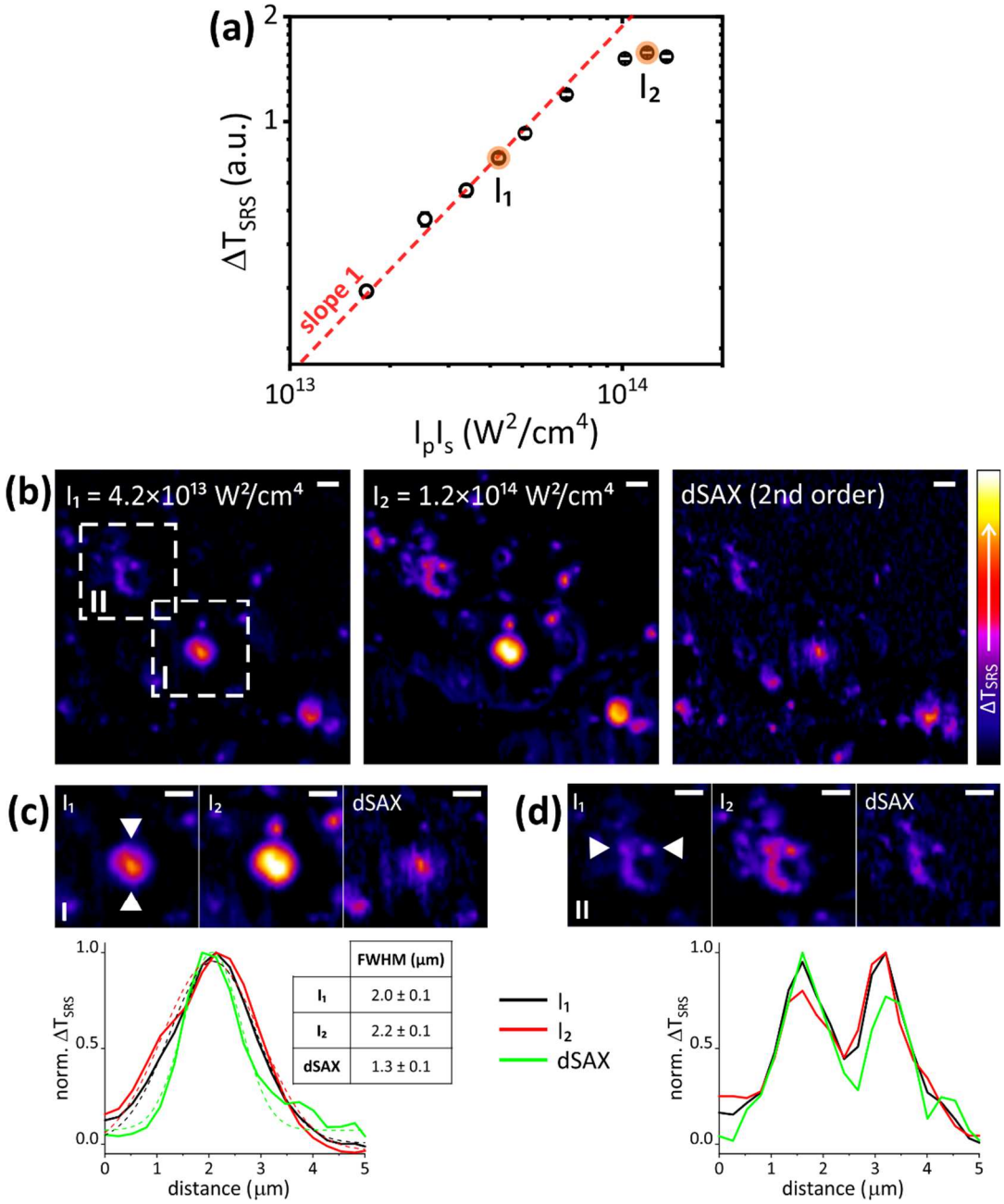

Figure 5.12 dSAX method applied on SRS imaging of diamond particles. **(a)** Experimental saturation curve of diamond. The linear fit at lower powers is shown as a dashed red line. Saturation appears around 10^{14} W^2cm^{-4}. The imaging conditions used for dSAX are marked in the graph with circles. **(b)** Images obtained at the excitation powers highlighted in the graph in **(a)** and the calculated second-order dSAX image (left). The areas in the squares (I and II) are enlarged in **(c)** and **(d)**. Scale bar 2 μm. (c) Detail I. Scale bar 2 μm. Line profiles along the direction of the arrows are plotted and the FWHM of their Gaussian fits are compared. **(d)** Detail II. Scale bar 2 μm. Line profiles along the direction of the arrows are plotted and compared.

PMMA beads. The main results of the SRS imaging of an isolated PMMA bead are shown in **Figure 5.13**. Images were acquired at different powers in the range 10^{15}-10^{16} W^2cm^{-4}. In **Figure 5.13(a)** the SRS signal is plotted as a function of the applied powers. It exhibits the expected linear behavior at lower powers and a marked saturation at higher powers, starting around 10^{16} W^2cm^{-4}. The images used for the extraction of the non-linearity were acquired at the powers I_1=4.9×10^{15} W^2cm^{-4} and I_2=1.1×10^{16} W^2cm^{-4} and are shown in **Figure 5.13(b)** together with the resulting dSAX image. Images were acquired using 128×128 pixels, a pixel dwell time of 500 µs and a lock-in integration time of 300 µs. The normalized line profiles along the direction marked by the white arrows are drawn and the FWHM of their Gaussian fits (dashed lines) are compared. Also in this case, the increase of the PSF when increasing the applied power can be markedly seen. Moreover, the application of dSAX leads to a 1.4-fold resolution improvement.

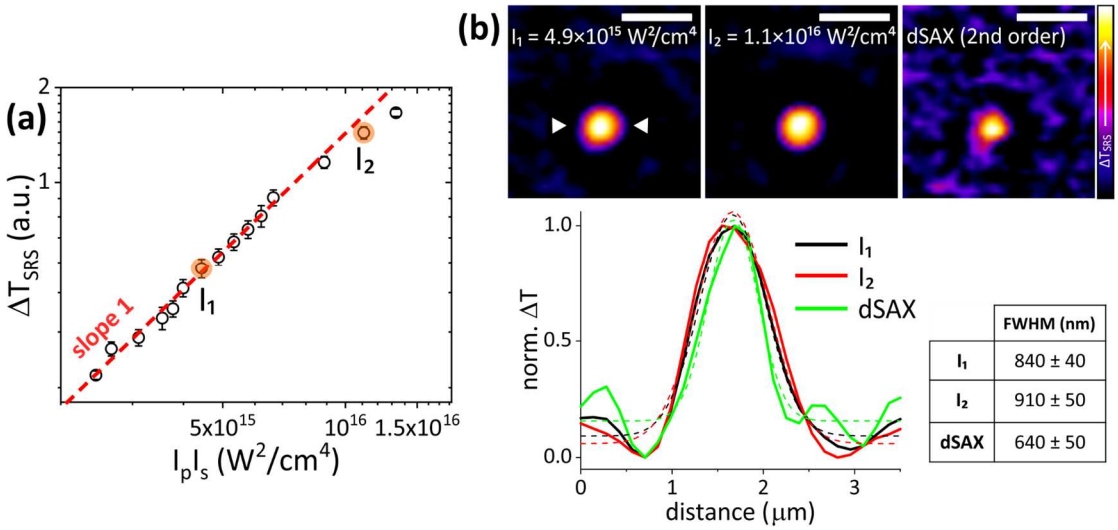

Figure 5.13 dSAX method applied on SRS imaging of a PMMA bead. **(a)** Experimental saturation curve of PMMA. The linear fit at lower powers is shown as a dashed red line. Saturation appears around 10^{16} W^2cm^{-4}. The imaging conditions used for the dSAX approach are marked in the graph with circles. **(b)** Images obtained at the excitation powers highlighted in the graph in **(a)** and the calculated second-order dSAX image (left). Scale bar 2 µm. Line profiles along the direction of the arrows are plotted and the FWHM of their Gaussian fits are compared.

5.5. Conclusions and future perspectives

The preliminary results of this project **confirmed the applicability of the dSAX approach for sub-diffraction label-free SRS imaging**.

As expected from the theory, the SRS signal saturates increasing the applied powers, causing a broadening of the effective PSF. The non-linearity of the saturation phenomenon can be effectively extracted with the dSAX algorithm, providing an isotropic spatial and spectral resolution enhancement of 1.3-fold and 1.7-fold, respectively, as calculated from the simulations of the second-order extraction. Spatial resolution improvement was also achieved experimentally in the dSAX imaging of diamond particles and PMMA beads.

The method proposed in this research is characterized by a straightforward implementation, which requires neither any modifications in a standard SRS microscope setup nor beam modification like a doughnut-shaped beam, providing opportunities of label-free super-resolution imaging for varieties of bioimaging applications.

The SAX approach has been already demonstrated in label-free CARS imaging of nanodiamonds [87]. Even if the two techniques are very similar, better results in terms of SNR are expected with the method here presented. First, because SRS produces a much stronger signal which is free of non-resonant background (see **Section 1.2.2**). Second, because the differential approach applied to SRS possesses a better detection efficiency compared to the modulation approach applied to CARS (see **Section 2.3.2**). Third, because with SRS we can access the second-order non-linearity, while with CARS the resolution improvement starts with the extraction of the much weaker third order non-linearity [87].

Further experiments are needed in order to better assess the performances and the applicability of saturated SRS, especially in label-free imaging of (living) biological samples, in biorthogonal chemical imaging [159], and in thick specimens imaging.

Different aspects of the approach may contribute to a positive result: (a) the confinement of the interaction, due to the non-linearity of the SRS process, will help in the achievement of signal saturation; (b) differently from fluorescence microscopy, the saturation powers that will be used will not cause photobleaching and signal degradation; (c) the use of longer wavelengths will give possibility to image thick specimens; (d) since no beam modifications are needed, the distortion of the beams through the sample will be limited and will not cause signal degradation. This may lead to the development of an easy-to-use super-resolution Raman imaging platform for biological applications for label-free and vibrational tags super-resolution imaging inside living cells and tissues. The improvement of spatial and spectral resolution of SRS microscopy is expected especially for the diagnosis of cells, such as cancer cells, in deep parts of the tissues, where the spatial resolution of optical imaging is significantly degraded.

Such a technique can pave the way for label-free diagnosis of tissue samples that, in the future, can contribute to the medical diagnosis and treatments, such as regenerative medicine.

Conclusion and outlook

This thesis is a **contribution to the field of label-free super-resolution microscopy**, and in particular, it gives insights into the **exploitation of saturation of non-fluorescent-based transitions to break the diffraction barrier in pump-probe microscopy techniques**.

Pump-probe microscopy is gaining much interest in multiple fields, from material to biological sciences, due to its remarkable detection sensitivity and sub-picosecond temporal resolution, which allows to resolve and monitor chemical and atomic ultrafast processes. The exploitation of absorption-based and scattering-based non-linear pump-probe interactions permits the direct imaging of the molecules of interest without any sample modification. In this microscopy field, the development of suitable sub-diffraction methods is still an open challenge that, if unraveled, may increase the availability of label-free approaches for a broader range of applications.

The first achievement of this research concerns the implementation of a transient absorption pump-probe microscope that allows for sub-diffraction imaging capabilities exploiting absorption saturation with a STED-like configuration. This pump-probe microscope achieves sub-picosecond temporal resolution in resolving ultrafast excited state dynamics and high sensitivity in detecting and quantifying single layers of graphene. Thanks to the upgrade with an additional doughnut-shaped non-modulated beam at the pump wavelength, the pump absorption can be saturated at the rim of the focal spot, suppressing the pump-probe signal. Single layer graphene was identified as an excellent candidate to test the technique, due to its broadband saturable absorption. The temporal synchronization of the pulses and the applied saturation power play an essential role in achieving an effective signal suppression and a consequent resolution improvement with relatively low powers. The maximum of the depletion efficiency was found when the three pulses temporally overlapped so that saturation powers around 15-20 mW can be used to achieve a signal suppression of about 80-90% without observing any sample damage. Remarkable resolution improvement and increase in layer sensitivity are achieved in imaging graphene multilayer defects. In principle, this approach can be extended for the super-resolution imaging of any highly-absorbing material or biological system which exhibits saturable absorption. This technique can find applications in the characterization of monomolecular layers and their defects in many other saturable materials, or mapping with improved spatial information weakly or non-fluorescent nanostructures, used in biomedical applications, in biological environments. In this last application, additional axial confinement of the detected pump-probe volume may be useful for following dynamics or interaction processes in three dimensions with an isotropic resolution enhancement, and this can be achieved engineering the saturation beam in the form of a bottle beam.

The second achievement of this research concerns the implementation of a stimulated Raman scattering pump-probe microscope and the experimental demonstration of the saturation of the vibrational transition for the application of the super-resolution SAX approach. Through a differential approach already demonstrated in confocal and two-photon microscopy, the high-order non-linearities contained in the saturated response are extracted from the center of the focal spot, producing a theoretical 1.3-fold isotropic spatial resolution enhancement, which is also confirmed experimentally. This approach is based on a straightforward implementation which does not require any setup modification nor beam engineering, which may lead to the development of an easy-to-use platform for super-resolution pump-probe imaging inside living cells and tissues.

The presented results demonstrate the great potential of absorption-based and scattering-based pump-probe techniques. Their high sensitivity, chemical specificity and high temporal and spatial resolution open the path to imaging of a variety of non-fluorescent chromophores, nanomaterial and vibrational tags which were previously inaccessible. The saturable absorption and vibrational transitions of intrinsic sample components offer similar ways to circumvent the diffraction barrier in label-free microscopy as in advanced super-resolution fluorescence-based methods.

Lastly, thanks to the implementation of NIR illumination, the presented saturated pump-probe microscopies open up the possibility to image in scattering media and tissues, achieving intrinsic optical sectioning and three-dimensional imaging capabilities with spatial resolution beyond the diffraction limit. The integration of these super-resolution methods into a multimodal non-linear microscopy platform together with other non-linear approaches, like multi-photon fluorescence and harmonic generation, will be the future for the advancement of label-free techniques broadening the range of biological and material imaging applications.

References

1. R. L. Sutherland, *Handbook of Nonlinear Optics* (1997), **36**(3).
2. M. Fox, *Optical Properties of Solids* (Oxford University Press, 2001).
3. R. W. Boyd, *Nonlinear Optics* (2003).
4. J. X. Cheng and X. S. Xie, *Coherent Raman Scattering Microscopy* (2013).
5. F. Träger, *Springer Handbook of Lasers and Optics* (2012).
6. M. Bass, C. M. DeCusatis, J. M. Enoch, V. Lakshminarayanan, G. Li, C. MacDonald, V. N. Mahajan, and E. Van Stryland, *Handbook of Optics - Volume IV. Optical Properties of Materials, Nonlinear Optics, Quantum Optics* (2010).
7. M. Sheik-Bahae and M. P. Hasselbeck, "Third order optical nonlinearities," OSA Handb. Opt. **4**, 1 (2000).
8. A. Diaspro, G. Chirico, and M. Collini, "Two-photon fluorescence excitation and related techniques in biological microscopy," Q. Rev. Biophys. **38**(2), 97–166 (2005).
9. W. R. Zipfel, R. M. Williams, and W. W. Webb, "Nonlinear magic: multiphoton microscopy in the biosciences.," Nat. Biotechnol. **21**(11), 1369–77 (2003).
10. M. Göppert□Mayer and M. Göppert-Mayer, "Über elementarakte mit zwei quantensprüngen [Elementary processes with two quantum transitions]," Ann. Phys. (1931).
11. P.-T. Dong and J.-X. Cheng, "Pump – Probe Microscopy□: Theory , Instrumentation , and Applications," Spectroscopy **32**(4), *2*–11 (2017).
12. D. Fu, T. E. Matthews, T. Ye, I. R. Piletic, and W. S. Warren, "Label-free in vivo optical imaging of microvasculature and oxygenation level," J. Biomed. Opt. **13**(4), 040503 (2008).
13. J. Cabanillas-Gonzalez, G. Grancini, and G. Lanzani, "Pump-probe spectroscopy in organic semiconductors: Monitoring fundamental processes of relevance in optoelectronics," Adv. Mater. **23**(46), 5468–5485 (2011).
14. W. M. Tolles, J. W. Nibler, J. R. McDonald, and A. B. Harvey, "A Review of the Theory and Application of Coherent Anti-Stokes Raman Spectroscopy (CARS)," Appl. Spectrosc. **31**(4), 253–271 (1977).
15. E. J. Woodbury and W. K. Ng, "Ruby laser operation in the near IR," in *Proc. Inst. Radio Eng. 50* (1962), p. 2367.
16. M. D. Duncan, P. Oesterun, F. König, and R. L. Byer, "Observation of saturation broadening of the coherent anti-stokes raman spectrum (cars) of acetylene in a pulsed molecular beam," Chem. Phys. Lett. (1981).
17. G. Magnotti, A. D. Cutler, G. C. Herring, S. A. Tedder, and P. M. Danehy, "Saturation and Stark broadening effects in dual-pump CARS of N2, O2, and H2," J. Raman Spectrosc. **43**(5), 611–620 (2012).
18. A. Diaspro, "Confocal and two-photon microscopy□: foundations, applications, and

advances," in (Wiley-Liss, 2002), p. 567.

19. D. Mazza, K. Braeckmans, F. Cella, I. Testa, D. Vercauteren, J. Demeester, S. S. De Smedt, and A. Diaspro, "A new FRAP/FRAPa method for three-dimensional diffusion measurements based on multiphoton excitation microscopy," Biophys. J. **95**(7), 3457–3469 (2008).

20. Y. Sun, H. Wallrabe, C. F. Booker, R. N. Day, and A. Periasamy, "Three-color spectral FRET microscopy localizes three interacting proteins in living cells," Biophys. J. **99**(4), 1274–1283 (2010).

21. H. Wallrabe and A. Periasamy, "Imaging protein molecules using FRET and FLIM microscopy," Curr. Opin. Biotechnol. **16**(1 SPEC. ISS.), 19–27 (2005).

22. L. Scipioni, M. Di Bona, G. Vicidomini, A. Diaspro, and L. Lanzanò, "Local raster image correlation spectroscopy generates high-resolution intracellular diffusion maps," Commun. Biol. **1**(1), 10 (2018).

23. H. Chen, H. Wang, M. N. Slipchenko, Y. Jung, Y. Shi, J. Zhu, K. K. Buhman, and J.-X. Cheng, "A multimodal platform for nonlinear optical microscopy and microspectroscopy.," Opt. Express **17**(3), 1282–1290 (2009).

24. T. Meyer, M. Schmitt, B. Dietzek, and J. Popp, "Accumulating advantages, reducing limitations: Multimodal nonlinear imaging in biomedical sciences - The synergy of multiple contrast mechanisms," J. Biophotonics **6**(11–12), 887–904 (2013).

25. A. Diaspro, P. Bianchini, G. Vicidomini, M. Faretta, P. Ramoino, and C. Usai, "Multi-photon excitation microscopy," Biomed. Eng. Online **5**(1), 36 (2006).

26. P. Bianchini and A. Diaspro, "Three-dimensional (3D) backward and forward second harmonic generation (SHG) microscopy of biological tissues," J. Biophotonics **1**(6), 443–450 (2008).

27. G. Zanini, "Towards optical biopsy of human skin lesions: a two-photon micorscopy feasibility study," Master thesis, Department of Physics, University of Trento (2014).

28. F. Lu, S. Basu, V. Igras, M. P. Hoang, M. Ji, D. Fu, G. R. Holtom, V. A. Neel, C. W. Freudiger, D. E. Fisher, X. S. Xie, A. Victor, C. W. Freudiger, D. E. Fisher, X. Sunney, F. Lu, S. Basu, V. Igras, M. P. Hoang, M. Ji, D. Fu, G. R. Holtom, and V. A. Neel, "Label-free DNA imaging in vivo with stimulated Raman scattering microscopy," Proc. Natl. Acad. Sci. **112**(43), E5902–E5902 (2015).

29. D. B. Murphy and M. W. Davidson, *Fundamentals of Light Microscopy and Electronic Imaging: Second Edition* (2012).

30. G. B. Airy, "On the diffraction of an object-glass with circular aperture," Trans. Cambridge Phil. Soc. **5**, 283–291 (1835).

31. E. Abbe, "Beiträge zur Theorie des Mikroskops und der mikroskopischen Wahrnehmung," Arch. für Mikroskopische Anat. **9**(1), 413–418 (1873).

32. Rayleigh, "XXXI. Investigations in optics, with special reference to the spectroscope," London, Edinburgh, Dublin Philos. Mag. J. Sci. **8**(49), 261–274 (1879).

33. C. J. R. Sheppard and A. Choudhury, "Image Formation in the Scanning Microscope," Opt. Acta Int. J. Opt. **24**(10), 1051–1073 (1977).

34. D. Davydova, A. de la Cadena, D. Akimov, and B. Dietzek, "Transient absorption

microscopy: Advances in chemical imaging of photoinduced dynamics," Laser Photonics Rev. **10**(1), 62–81 (2016).

35. S. Hell and E. H. K. Stelzer, "Properties of a 4Pi confocal fluorescence microscope," J. Opt. Soc. Am. A (1992).

36. S. Hell and E. H. K. Stelzer, "Fundamental improvement of resolution with a 4Pi-confocal fluorescence microscope using two-photon excitation," Opt. Commun. (1992).

37. M. G. L. Gustafsson, D. A. Agard, and J. W. Sedat, "Sevenfold improvement of axial resolution in 3D wide-field microscopy using two objective lenses," in T. Wilson and C. J. Cogswell, eds. (International Society for Optics and Photonics, 1995), **2412**, pp. 147–156.

38. Gustafsson, Agard, and Sedat, "I5M: 3D widefield light microscopy with better than 100 nm axial resolution," J. Microsc. **195**(1), 10–16 (1999).

39. M. G. L. Gustafsson, "Surpassing the lateral resolution limit by a factor of two using structured illumination microscopy.," J. Microsc. **198**(Pt 2), 82–7 (2000).

40. S. W. Hell, "Toward fluorescence nanoscopy.," Nat. Biotechnol. **21**(11), 1347–55 (2003).

41. S. W. Hell and J. Wichmann, "Breaking the diffraction resolution limit by stimulated emission: stimulated-emission-depletion fluorescence microscopy," Opt. Lett. (1994).

42. S. W. Hell, "Fluorescence nanoscopy: Breaking the diffraction barrier by the RESOLFT concept," in *Nanobiotechnology* (2005).

43. I. Testa, E. D'Este, N. T. Urban, F. Balzarotti, and S. W. Hell, "Dual channel RESOLFT nanoscopy by using fluorescent state kinetics," Nano Lett. **15**(1), 103–106 (2015).

44. K. Fujita, M. Kobayashi, S. Kawano, M. Yamanaka, and S. Kawata, "High-resolution confocal microscopy by saturated excitation of fluorescence," Phys. Rev. Lett. **99**(22), 1–4 (2007).

45. B. Harke, J. Keller, C. K. Ullal, V. Westphal, A. Schönle, and S. W. Hell, "Resolution scaling in STED microscopy," Opt. Express **16**(6), 4154 (2008).

46. S. W. Hell, "Microscopy and its focal switch," Nat. Methods **6**(1), 24–32 (2009).

47. M. Hofmann, C. Eggeling, S. Jakobs, and S. W. Hell, "Breaking the diffraction barrier in fluorescence microscopy at low light intensities by using reversibly photoswitchable proteins," Proc. Natl. Acad. Sci. **102**(49), 17565–17569 (2005).

48. P. Bianchini, C. Peres, M. Oneto, S. Galiani, G. Vicidomini, and A. Diaspro, "STED nanoscopy: a glimpse into the future," Cell Tissue Res. **360**(1), 143–150 (2015).

49. G. Vicidomini, P. Bianchini, and A. Diaspro, "STED super-resolved microscopy," Nat. Methods **15**(3), 173–182 (2018).

50. S. Galiani, B. Harke, G. Vicidomini, G. Lignani, F. Benfenati, A. Diaspro, and P. Bianchini, "Strategies to maximize the performance of a STED microscope," Opt. Express **20**(7), 7362 (2012).

51. T. A. Klar, S. Jakobs, M. Dyba, A. Egner, and S. W. Hell, "Fluorescence microscopy with diffraction resolution barrier broken by stimulated emission," Proc. Natl. Acad. Sci. (2000).

52. G. Vicidomini, G. Moneron, K. Y. Han, V. Westphal, H. Ta, M. Reuss, J. Engelhardt, C.

Eggeling, and S. W. Hell, "Sharper low-power STED nanoscopy by time gating.," Nat. Methods **8**(7), 571–573 (2011).

53. P. Bianchini, B. Harke, S. Galiani, G. Vicidomini, and A. Diaspro, "Single-wavelength two-photon excitation-stimulated emission depletion (SW2PE-STED) superresolution imaging.," Proc. Natl. Acad. Sci. U. S. A. **109**(17), 6390–3 (2012).

54. A. Chmyrov, J. Keller, T. Grotjohann, M. Ratz, E. D'Este, S. Jakobs, C. Eggeling, and S. W. Hell, "Nanoscopy with more than 100,000 "doughnuts,"" Nat. Methods **10**(8), 737–740 (2013).

55. F. Göttfert, C. A. Wurm, V. Mueller, S. Berning, V. C. Cordes, A. Honigmann, and S. W. Hell, "Coaligned dual-channel STED nanoscopy and molecular diffusion analysis at 20 nm resolution," Biophys. J. (2013).

56. G. C. Cianci, J. Wu, and K. M. Berland, "Saturation modified point spread functions in two-photon microscopy," Microsc. Res. Tech. **64**(2), 135–141 (2004).

57. A. Diaspro, *Nanoscopy and Multidimensional Optical Fluorescence Microscopy* (CRC Press/Taylor & Francis Group, 2010).

58. M. Yamanaka, S. Kawano, K. Fujita, N. I. Smith, and S. Kawata, "Beyond the diffraction-limit biological imaging by saturated excitation microscopy.," J. Biomed. Opt. **13**(5), 050507 (2008).

59. M. Yamanaka, K. Saito, N. I. Smith, S. Kawata, T. Nagai, and K. Fujita, "Saturated excitation of fluorescent proteins for subdiffraction-limited imaging of living cells in three dimensions Saturated excitation of fluorescent proteins for subdiffraction-limited imaging of living cells in three dimensions," R. Soc. (2013).

60. M. Yamanaka, Y. Yonemaru, S. Kawano, K. Uegaki, N. I. Smith, S. Kawata, and K. Fujita, "Saturated excitation microscopy for sub-diffraction-limited imaging of cell clusters," J. Biomed. Opt. **18**(12), 126002 (2013).

61. M. Yamanaka, Y.-K. Tzeng, S. Kawano, N. I. Smith, S. Kawata, H.-C. Chang, and K. Fujita, "SAX microscopy with fluorescent nanodiamond probes for high-resolution fluorescence imaging.," Biomed. Opt. Express **2**(7), 1946–1954 (2011).

62. J. Humpolíčková, A. Benda, and J. Enderlein, "Optical saturation as a versatile tool to enhance resolution in confocal microscopy," Biophys. J. **97**(9), 2623–2629 (2009).

63. Y. Zhang, P. D. Nallathamby, G. D. Vigil, A. A. Khan, D. E. Mason, J. D. Boerckel, R. K. Roeder, and S. S. Howard, "Super-resolution fluorescence microscopy by stepwise optical saturation," **9**(4), 82–87 (2018).

64. Y. Nawa, Y. Yonemaru, A. Kasai, R. Oketani, H. Hashimoto, N. I. Smith, and K. Fujita, "Saturated excitation microscopy using differential excitation for efficient detection of nonlinear fluorescence signals," APL Photonics **3**(8), 080805 (2018).

65. R. Oketani, A. Doi, N. I. Smith, Y. Nawa, S. Kawata, and K. Fujita, "Saturated two-photon excitation fluorescence microscopy with core-ring illumination," Opt. Lett. **42**(3), 571 (2017).

66. X. Zhang and Z. Liu, "Superlenses to overcome the diffraction limit," Nat. Mater. **7**(6), 435–441 (2008).

67. S. Lee, L. Li, Y. Ben-Aryeh, Z. Wang, and W. Guo, "Overcoming the diffraction limit

induced by microsphere optical nanoscopy," J. Opt. (United Kingdom) **15**(12), (2013).

68. L. Li, W. Guo, Y. Yan, S. Lee, and T. Wang, "Label-free super-resolution imaging of adenoviruses by submerged microsphere optical nanoscopy," Light Sci. Appl. (2013).

69. J. Liu, I. H. Cho, Y. Cui, and J. Irudayaraj, "Second harmonic super-resolution microscopy for quantification of mRNA at single copy sensitivity," ACS Nano **8**(12), 12418–12427 (2014).

70. C. Kuang, S. Li, W. Liu, X. Hao, Z. Gu, Y. Wang, J. Ge, H. Li, and X. Liu, "Breaking the Diffraction Barrier Using Fluorescence Emission Difference Microscopy," Sci. Rep. **3**(1), 1441 (2013).

71. K. Korobchevskaya, C. Peres, Z. Li, A. Antipov, C. J. R. Sheppard, A. Diaspro, and P. Bianchini, "Intensity Weighted Subtraction Microscopy Approach for Image Contrast and Resolution Enhancement," Sci. Rep. **6**(April), 25816 (2016).

72. N. Liu, M. Kumbham, I. Pita, Y. Guo, P. Bianchini, A. Diaspro, S. A. M. Tofail, A. Peremans, and C. Silien, "Far-Field Subdiffraction Imaging of Semiconductors Using Nonlinear Transient Absorption Differential Microscopy," ACS Photonics **3**(3), 478–485 (2016).

73. C. Silien, N. Liu, N. Hendaoui, S. a M. Tofail, and A. Peremans, "A framework for far-field infrared absorption microscopy beyond the diffraction limit.," Opt. Express **20**(28), 29694–704 (2012).

74. I. Pita, N. Hendaoui, N. Liu, M. Kumbham, S. A. M. Tofail, A. Peremans, and C. Silien, "High resolution imaging with differential infrared absorption micro-spectroscopy," Opt. Express **21**(22), 25632 (2013).

75. A. Gasecka, A. Daradich, H. Dehez, M. Piché, and D. Côté, "Resolution and contrast enhancement in coherent anti-Stokes Raman-scattering microscopy," Opt. Lett. **38**(21), 4510 (2013).

76. D. Wang, S. Liu, Y. Chen, J. Song, W. Liu, M. Xiong, G. Wang, X. Peng, and J. Qu, "Breaking the diffraction barrier using coherent anti-Stokes Raman scattering difference microscopy," Opt. Express **25**(9), 10276–10286 (2017).

77. K. Watanabe, A. F. Palonpon, N. I. Smith, L. Chiu, A. Kasai, H. Hashimoto, S. Kawata, and K. Fujita, "Structured line illumination Raman microscopy," Nat. Commun. **6**(May), 10095 (2015).

78. E. S. Massaro, A. H. Hill, and E. M. Grumstrup, "Super-Resolution Structured Pump-Probe Microscopy," ACS Photonics **3**(4), 501–506 (2016).

79. Y.-H. Kim and P. T. C. So, "Three-dimensional wide-field pump-probe structured illumination microscopy: erratum," Opt. Express **25**(25), 31423 (2017).

80. W. Liu and H. Niu, "Diffraction barrier breakthrough in coherent anti-stokes Raman scattering microscopy by additional probe-beam-induced phonon depletion," Phys. Rev. A - At. Mol. Opt. Phys. **83**(2), 1–5 (2011).

81. C. Cleff, P. Groß, C. Fallnich, H. L. Offerhaus, J. L. Herek, K. Kruse, W. P. Beeker, C. J. Lee, and K.-J. Boller, "Ground-state depletion for subdiffraction-limited spatial resolution in coherent anti-Stokes Raman scattering microscopy," Phys. Rev. A **86**(2), 023825 (2012).

82. C. Cleff, P. Groß, C. Fallnich, H. L. Offerhaus, J. L. Herek, K. Kruse, W. P. Beeker, C. J. Lee, and K. J. Boller, "Stimulated-emission pumping enabling sub-diffraction-limited spatial

resolution in coherent anti-Stokes Raman scattering microscopy," Phys. Rev. A - At. Mol. Opt. Phys. **87**(3), 1–9 (2013).

83. W. R. Silva, C. T. Graefe, and R. R. Frontiera, "Toward Label-Free Super-Resolution Microscopy," ACS Photonics **3**(1), 79–86 (2016).

84. D. Kim, D. S. Choi, J. Kwon, S.-H. Shim, H. Rhee, and M. Cho, "Selective Suppression of Stimulated Raman Scattering with Another Competing Stimulated Raman Scattering," J. Phys. Chem. Lett. 6118–6123 (2017).

85. P. Wang, M. N. Slipchenko, J. Mitchell, C. Yang, E. O. Potma, X. Xu, and J.-X. X. Cheng, "Far-field imaging of non-fluorescent species with subdiffraction resolution," Nat. Photonics **7**(6), 449–453 (2013).

86. P. Bianchini, K. Korobchevskaya, G. Zanini, and A. Diaspro, "Pump-Probe Nanoscopy by Means of Transient Absorption Saturation," in *2018 20th International Conference on Transparent Optical Networks (ICTON)* (IEEE, 2018), pp. 1–4.

87. Y. Yonemaru, A. F. Palonpon, S. Kawano, N. I. Smith, S. Kawata, and K. Fujita, "Super-spatial- and -spectral-resolution in vibrational imaging via saturated coherent anti-stokes Raman scattering," Phys. Rev. Appl. **4**(1), 1–7 (2015).

88. G. Deka, K. Nishida, K. Mochizuki, and K. Fujita, "Resolution enhancement in deep-tissue nanoparticle imaging based on plasmonic saturated excitation microscopy," APL Photonics **3**(3), 031301 (2018).

89. A. Danielli, K. Maslov, A. Garcia-Uribe, A. M. Winkler, C. Li, L. Wang, Y. Chen, G. W. Dorn, and L. V. Wang, "Label-free photoacoustic nanoscopy," J. Biomed. Opt. **19**(8), 086006 (2014).

90. D. A. Nedosekin, E. I. Galanzha, E. Dervishi, A. S. Biris, and V. P. Zharov, "Super-resolution nonlinear photothermal microscopy," Small **10**(1), 135–142 (2014).

91. G. Porter, "Flash Photolysis and Spectroscopy. A New Method for the Study of Free Radical Reactions," Proc. R. Soc. A Math. Phys. Eng. Sci. **200**(1061), 284–300 (1950).

92. G. PORTER and M. R. TOPP, "Nanosecond Flash Photolysis and the Absorption Spectra of Excited Singlet States," Nature **220**(5173), 1228–1229 (1968).

93. G. Porter and M. R. Topp, "Nanosecond Flash Photolysis," Proc. R. Soc. A Math. Phys. Eng. Sci. **315**(1521), 163–184 (1970).

94. U. Megerle, I. Pugliesi, C. Schriever, C. F. Sailer, and E. Riedle, "Sub-50 fs broadband absorption spectroscopy with tunable excitation: putting the analysis of ultrafast molecular dynamics on solid ground," Appl. Phys. B Lasers Opt. **96**(2–3), 215–231 (2009).

95. R. Berera, R. van Grondelle, and J. T. M. Kennis, "Ultrafast transient absorption spectroscopy: principles and application to photosynthetic systems," Photosynth. Res. **101**(2–3), 105–118 (2009).

96. F. Preda, V. Kumar, F. Crisafi, D. G. Figueroa del Valle, G. Cerullo, and D. Polli, "Broadband pump-probe spectroscopy at 20-MHz modulation frequency," Opt. Lett. **41**(13), 2970 (2016).

97. D. Polli, L. Lüer, and G. G. Cerullo, "High-time-resolution pump-probe system with broadband detection for the study of time-domain vibrational dynamics," Rev. Sci.

Instrum. **78**(10), 103108 (2007).

98. C. Burda and M. A. El-Sayed, "High-density femtosecond transient absorption spectroscopy of semiconductor nanoparticles. A tool to investigate surface quality," Pure Appl. Chem. (2000).

99. A. Beeby, "Pump-Probe Laser Spectroscopy," in *An Introduction to Laser Spectroscopy* (Springer US, 2002), pp. 105–137.

100. L. Wei and W. Min, "Pump-probe optical microscopy for imaging nonfluorescent chromophores," Anal. Bioanal. Chem. **403**(8), 2197–2202 (2012).

101. M. C. Fischer, J. W. Wilson, F. E. Robles, and W. S. Warren, "Invited Review Article: Pump-probe microscopy," Rev. Sci. Instrum. **87**(3), (2016).

102. T. Virgili, G. Grancini, E. Molotokaite, I. Suarez-Lopez, S. K. Rajendran, A. Liscio, V. Palermo, G. Lanzani, D. Polli, and G. Cerullo, "Confocal ultrafast pump–probe spectroscopy: a new technique to explore nanoscale composites," Nanoscale **4**(7), 2219 (2012).

103. T. Ye, D. Fu, and W. S. Warren, "Nonlinear absorption microscopy," Photochem. Photobiol. **85**(3), 631–645 (2009).

104. M. Seo, S. Boubanga-Tombet, J. Yoo, Z. Ku, A. V. Gin, S. T. Picraux, S. R. J. Brueck, A. J. Taylor, and R. P. Prasankumar, "Ultrafast optical wide field microscopy," Opt. Express **21**(7), 8763 (2013).

105. M. A. Digman, V. R. Caiolfa, M. Zamai, and E. Gratton, "The phasor approach to fluorescence lifetime imaging analysis," Biophys. J. (2008).

106. G. V. Hartland, "Ultrafast studies of single semiconductor and metal nanostructures through transient absorption microscopy," Chem. Sci. **1**(3), 303–309 (2010).

107. C. Y. Dong, P. T. So, T. French, and E. Gratton, "Fluorescence lifetime imaging by asynchronous pump-probe microscopy," Biophys. J. **69**(6), 2234–2242 (1995).

108. C. Buehler, C. Y. Dong, P. T. C. So, T. French, and E. Gratton, "Time-Resolved Polarization Imaging By Pump-Probe (Stimulated Emission) Fluorescence Microscopy," **79**(July), 536–549 (2000).

109. D. Fu, T. Ye, T. E. Matthews, G. Yurtsever, and W. S. Warren, "Two-color, two-photon, and excited-state absorption microscopy," J. Biomed. Opt. **12**(5), 054004 (2007).

110. M. M. Gabriel, J. R. Kirschbrown, J. D. Christesen, C. W. Pinion, D. F. Zigler, E. M. Grumstrup, B. P. Mehl, E. E. M. Cating, J. F. Cahoon, and J. M. Papanikolas, "Direct imaging of free carrier and trap carrier motion in silicon nanowires by spatially-separated femtosecond pump-probe microscopy," Nano Lett. **13**(3), 1336–1340 (2013).

111. S. S. Lo, T. A. Major, N. Petchsang, L. Huang, M. K. Kuno, and G. V. Hartland, "Charge carrier trapping and acoustic phonon modes in single CdTe nanowires," ACS Nano **6**(6), 5274–5282 (2012).

112. C. Y. Wong, S. B. Penwell, B. L. Cotts, R. Noriega, H. Wu, and N. S. Ginsberg, "Revealing exciton dynamics in a small-molecule organic semiconducting film with subdomain transient absorption microscopy," J. Phys. Chem. C **117**(42), 22111–22122 (2013).

113. D. Davydova, A. De La Cadena, S. Demmler, J. Rothhardt, J. Limpert, T. Pascher, D. Akimov, and B. Dietzek, "Ultrafast transient absorption microscopy: Study of excited

state dynamics in PtOEP crystals," Chem. Phys. **464**, 69–77 (2016).

114. S. Chong, W. Min, and X. S. Xie, "Ground-State Depletion Microscopy: Detection Sensitivity of Single-Molecule Optical Absorption at Room Temperature," J. Phys. Chem. Lett. **1**(23), 3316–3322 (2010).

115. Q. Cui, F. Ceballos, N. Kumar, and H. Zhao, "Transient absorption microscopy of monolayer and bulk WSe2," ACS Nano **8**(3), 2970–2976 (2014).

116. Z. Guo, J. S. S. Manser, Y. Wan, P. V. V. Kamat, and L. Huang, "Spatial and temporal imaging of long-range charge transport in perovskite thin films by ultrafast microscopy," Nat. Commun. **6**(1), 1–8 (2015).

117. Z. Guo, Y. Wan, M. Yang, J. Snaider, K. Zhu, and L. Huang, "Long-range hot-carrier transport in hybrid perovskites visualized by ultrafast microscopy," Science (80-.). **356**(6333), 59–62 (2017).

118. Z. Guo, N. Zhou, O. F. Williams, J. Hu, W. You, and A. M. Moran, "Imaging Carrier Diffusion in Perovskites with a Diffractive Optic-Based Transient Absorption Microscope," J. Phys. Chem. C **122**(19), 10650–10656 (2018).

119. Y. Jung, M. N. Slipchenko, C. H. Liu, A. E. Ribbe, Z. Zhong, C. Yang, and J.-X. X. Cheng, "Fast detection of the metallic state of individual single-walled carbon nanotubes using a transient-absorption optical microscope," Phys. Rev. Lett. **105**(21), 1–4 (2010).

120. Y. Wan, Z. Guo, T. Zhu, S. Yan, J. Johnson, and L. Huang, "Cooperative singlet and triplet exciton transport in tetracene crystals visualized by ultrafast microscopy," Nat. Chem. **7**(10), 785–792 (2015).

121. L. Tong, Y. Liu, B. D. Dolash, Y. Jung, M. N. Slipchenko, D. E. Bergstrom, and J.-X. Cheng, "Label-free imaging of semiconducting and metallic carbon nanotubes in cells and mice using transient absorption microscopy," Nat. Nanotechnol. **7**(1), 56–61 (2012).

122. T. Chen, F. Lu, A. M. Streets, P. Fei, J. Quan, and Y. Huang, "Optical imaging of non-fluorescent nanodiamonds in live cells using transient absorption microscopy.," Nanoscale **5**(11), 4701–5 (2013).

123. T. Chen, S. Chen, J. Zhou, D. Liang, X. Chen, and Y. Huang, "Transient absorption microscopy of gold nanorods as spectrally orthogonal labels in live cells," Nanoscale **6**(18), 10536–10539 (2014).

124. L. Zhang, S. Shen, Z. Liu, and M. Ji, "Label-Free, Quantitative Imaging of MoS_2 -Nanosheets in Live Cells with Simultaneous Stimulated Raman Scattering and Transient Absorption Microscopy," Adv. Biosyst. **1**(4), 1700013 (2017).

125. J. Liu and J. M. K. Irudayaraj, "Non-fluorescent quantification of single mRNA with transient absorption microscopy," Nanoscale **8**(46), 19242–19248 (2016).

126. K. S. Novoselov, "Electric Field Effect in Atomically Thin Carbon Films," Science (80-.). **306**(5696), 666–669 (2004).

127. E. Malic and A. Knorr, *Graphene and Carbon Nanotubes: Ultrafast Relaxation Dynamics and Optics* (Wiley-VCH Verlag GmbH & Co. KGaA, 2013).

128. E. Hendry, P. J. Hale, J. Moger, A. K. Savchenko, and S. A. Mikhailov, "Coherent nonlinear optical response of graphene," Phys. Rev. Lett. **105**(9), 1–4 (2010).

129. J. M. Dawlaty, S. Shivaraman, M. Chandrashekhar, F. Rana, and M. G. Spencer,

"Measurement of ultrafast carrier dynamics in epitaxial graphene," Appl. Phys. Lett. **92**(4), (2008).

130. M. Breusing, S. Kuehn, T. Winzer, E. Malić, F. Milde, N. Severin, J. P. Rabe, C. Ropers, A. Knorr, and T. Elsaesser, "Ultrafast nonequilibrium carrier dynamics in a single graphene layer," Phys. Rev. B - Condens. Matter Mater. Phys. **83**(15), 1–4 (2011).

131. R. W. Newson, J. Dean, B. Schmidt, and H. M. van Driel, "Ultrafast carrier kinetics in exfoliated graphene and thin graphite films," Opt. Express **17**(4), 2326 (2009).

132. P. J. Hale, S. M. Hornett, J. Moger, D. W. Horsell, and E. Hendry, "Hot phonon decay in supported and suspended exfoliated graphene," Phys. Rev. B - Condens. Matter Mater. Phys. **83**(12), 4–7 (2011).

133. D. Brida, A. Tomadin, C. Manzoni, Y. J. Kim, A. Lombardo, S. Milana, R. R. Nair, K. S. Novoselov, A. C. Ferrari, G. Cerullo, and M. Polini, "Ultrafast collinear scattering and carrier multiplication in graphene," Nat. Commun. **4**(May), 1–9 (1AD).

134. S. Kumar, M. Anija, N. Kamaraju, K. S. Vasu, K. S. Subrahmanyam, A. K. Sood, and C. N. R. Rao, "Femtosecond carrier dynamics and saturable absorption in graphene suspensions," Appl. Phys. Lett. **95**(19), 2007–2010 (2009).

135. J. Shang, L. Ma, J. Li, W. Ai, T. Yu, and G. G. Gurzadyan, "Femtosecond pump-probe spectroscopy of graphene oxide in water," J. Phys. D. Appl. Phys. **47**(9), (2014).

136. L. Huang, G. V. Hartland, L. Q. Chu, Luxmi, R. M. Feenstra, C. Lian, K. Tahy, and H. Xing, "Ultrafast transient absorption microscopy studies of carrier dynamics in epitaxial graphene," Nano Lett. **10**(4), 1308–1313 (2010).

137. J. Li, W. Zhang, T. Chung, M. N. Slipchenko, Y. P. Chen, J.-X. Cheng, and C. Yang, "Highly sensitive transient absorption imaging of graphene and graphene oxide in living cells and circulating blood," Sci. Rep. **5**(February), 12394 (2015).

138. H. Patel, R. W. Havener, L. Brown, Y. Liang, L. Yang, J. Park, and M. W. Graham, "Tunable Optical Excitations in Twisted Bilayer Graphene Form Strongly Bound Excitons," Nano Lett. **15**(9), 5932–5937 (2015).

139. K.-C. C. Huang, J. McCall, P. Wang, C.-S. S. Liao, G. Eakins, J.-X. X. Cheng, and C. Yang, "High-Speed Spectroscopic Transient Absorption Imaging of Defects in Graphene," Nano Lett. **18**(2), 1489–1497 (2018).

140. B. Gao, G. Hartland, T. Fang, M. Kelly, D. Jena, H. Xing, and L. Huang, "Studies of intrinsic hot phonon dynamics in suspended graphene by transient absorption microscopy," Nano Lett. **11**(8), 3184–3189 (2011).

141. G. Grancini, N. Martino, M. Bianchi, L. G. Rizzi, V. Russo, A. Li Bassi, C. S. Casari, A. Petrozza, R. Sordan, and G. Lanzani, "Ultrafast spectroscopic imaging of exfoliated graphene," Phys. Status Solidi Basic Res. **249**(12), 2497–2499 (2012).

142. W. Min, S. Lu, S. Chong, R. Roy, G. R. Holtom, X. S. Xie, and X. Sunney Xie, "Imaging chromophores with undetectable fluorescence by stimulated emission microscopy," Nature **461**(7267), 1105–1109 (2009).

143. L. Wei, Z. Chen, and W. Min, "Stimulated emission reduced fluorescence microscopy: a concept for extending the fundamental depth limit of two-photon fluorescence imaging," Biomed. Opt. Express **3**(6), 1465–1475 (2012).

144. P.-Y. Lin, S.-S. Lee, C.-S. Chang, and F.-J. Kao, "Long working distance fluorescence lifetime imaging with stimulated emission and electronic time delay," Opt. Express **20**(10), 11445 (2012).

145. F. Dake and Y. Taki, "Time-domain fluorescence lifetime imaging by nonlinear fluorescence microscopy constructed of a pump-probe setup with two-wavelength laser pulses," Appl. Opt. **57**(4), 757 (2018).

146. F. Dake and H. Yazawa, "Experimental assessment of fluorescence microscopy signal enhancement by stimulated emission," Opt. Rev. **24**(5), 642–646 (2017).

147. T. E. Matthews, I. R. Piletic, M. A. Selim, M. J. Simpson, and W. S. Warren, "Pump-probe imaging differentiates melanoma from melanocytic nevi," Sci. Transl. Med. **3**(71), (2011).

148. J. W. Wilson, S. Degan, M. A. Selim, J. Y. Zhang, and W. S. Warren, "In vivo pump-probe microscopy of melanoma and pigmented lesions," in (2012), **8226**, p. 822602.

149. T. Chen and Y. Huang, "Label-Free Transient Absorption Microscopy for Red Blood Cell Flow Velocity Measurement in Vivo," Anal. Chem. **89**(19), 10120–10123 (2017).

150. A. J. Chen, X. Yuan, J. Li, P. Dong, I. Hamza, and J.-X. Cheng, "Label-Free Imaging of Heme Dynamics in Living Organisms by Transient Absorption Microscopy," Anal. Chem. acs.analchem.7b05046 (2018).

151. T. E. Villafana, J. K. Delaney, W. S. Warren, and M. C. Fischer, "High-resolution, three-dimensional imaging of pigments and support in paper and textiles," J. Cult. Herit. **20**, 583–588 (2016).

152. P. Samineni, A. deCruz, T. E. Villafaña, W. S. Warren, and M. C. Fischer, "Pump-probe imaging of historical pigments used in paintings," Opt. Lett. **37**(8), 1310–1312 (2012).

153. R. C. Prince, R. R. Frontiera, and E. O. Potma, "Stimulated Raman scattering: From bulk to nano," Chem. Rev. **117**(7), 5070–5094 (2017).

154. C. W. Freudiger, W. Min, B. G. Saar, S. Lu, G. R. Holtom, C. He, J. C. Tsai, J. X. Kang, and X. S. Xie, "Label-free biomedical imaging with high sensitivity by stimulated raman scattering microscopy," Science (80-.). (2008).

155. P. Nandakumar, A. Kovalev, and A. Volkmer, "Vibrational imaging Based on stimulated Raman scattering microscopy," New J. Phys. **11**, (2009).

156. Y. Ozeki, F. Dake, S. Kajiyama, K. Fukui, and K. Itoh, "Analysis and experimental assessment of the sensitivity of stimulated Raman scattering microscopy," Opt. Express **17**(5), 3651 (2009).

157. B. G. Saar, C. W. Freudiger, J. Reichman, C. M. Stanley, G. R. Holtom, and X. S. Xie, "Video-Rate Molecular Imaging in Vivo with Stimulated Raman Scattering.," Sci. (Washington, DC, United States) **330**(6009), 1368–1370 (2010).

158. J.-X. Cheng and X. S. Xie, "Vibrational spectroscopic imaging of living systems: An emerging platform for biology and medicine.," Science **350**(6264), aaa8870 (2015).

159. L. Wei, F. Hu, Z. Chen, Y. Shen, L. Zhang, and W. Min, "Live-Cell Bioorthogonal Chemical Imaging: Stimulated Raman Scattering Microscopy of Vibrational Probes," Acc. Chem. Res. **49**(8), 1494–1502 (2016).

160. H. Kim, G. W. Bryant, and S. J. Stranick, "Superresolution four-wave mixing microscopy," Opt. Express (2012).

161. L. Gong and H. Wang, "Breaking the diffraction limit by saturation in stimulated-Raman-scattering microscopy: A theoretical study," Phys. Rev. A - At. Mol. Opt. Phys. **90**(1), 1–10 (2014).

162. J. Schindelin, I. Arganda-Carreras, E. Frise, V. Kaynig, M. Longair, T. Pietzsch, S. Preibisch, C. Rueden, S. Saalfeld, B. Schmid, J. Y. Tinevez, D. J. White, V. Hartenstein, K. Eliceiri, P. Tomancak, and A. Cardona, "Fiji: An open-source platform for biological-image analysis," Nat. Methods (2012).

163. X. Li, W. Cai, J. An, S. Kim, J. Nah, D. Yang, R. Piner, A. Velamakanni, I. Jung, E. Tutuc, S. K. Banerjee, L. Colombo, and R. S. Ruoff, "Large-Area Synthesis of High-Quality and Uniform Graphene Films on Copper Foils," Science (80-.). **324**(5932), 1312–1314 (2009).

164. X. Li, Y. Zhu, W. Cai, M. Borysiak, B. Han, D. Chen, R. D. Piner, L. Colombo, and R. S. Ruoff, "Transfer of Large-Area Graphene Films for High-Performance Transparent Conductive Electrodes," Nano Lett. **9**(12), 4359–4363 (2009).

165. "Monolayer Graphene film on Glass; Size: 1"x1"," http://graphene-supermarket.com/Monolayer-Graphene-film-on-Glass-Size-1-x1.html.

166. A. E. Del Rio Castillo, V. Pellegrini, A. Ansaldo, F. Ricciardella, H. Sun, L. Marasco, J. Buha, Z. Dang, L. Gagliani, E. Lago, N. Curreli, S. Gentiluomo, F. Palazon, M. Prato, R. Oropesa-Nuñez, P. S. Toth, E. Mantero, M. Crugliano, A. Gamucci, A. Tomadin, M. Polini, and F. Bonaccorso, "High-yield production of 2D crystals by wet-jet milling," Mater. Horizons **5**(5), 890–904 (2018).

167. L. Najafi, B. Taheri, B. Martín-García, S. Bellani, D. Di Girolamo, A. Agresti, R. Oropesa-Nuñez, S. Pescetelli, L. Vesce, E. Calabrò, M. Prato, A. E. Del Rio Castillo, A. Di Carlo, and F. Bonaccorso, "MoS2 Quantum Dot/Graphene Hybrids for Advanced Interface Engineering of a CH3NH3PbI3 Perovskite Solar Cell with an Efficiency of over 20%," ACS Nano (November 27, 2018).

168. S. Christodoulou, G. Vaccaro, V. Pinchetti, F. De Donato, J. Q. Grim, A. Casu, A. Genovese, G. Vicidomini, A. Diaspro, S. Brovelli, L. Manna, and I. Moreels, "Synthesis of highly luminescent wurtzite CdSe/CdS giant-shell nanocrystals using a fast continuous injection route," J. Mater. Chem. C **2**(17), 3439–3447 (2014).

169. R. R. Nair, P. Blake, A. N. Grigorenko, K. S. Novoselov, T. J. Booth, T. Stauber, N. M. R. Peres, and A. K. Geim, "Fine structure constant defines visual transparency of graphene," Science (80-.). **320**(5881), 1308 (2008).

170. K. F. Mak, J. Shan, and T. F. Heinz, "Seeing many-body effects in single- and few-layer graphene: Observation of two-dimensional saddle-point excitons," Phys. Rev. Lett. (2011).

171. V. I. Klimov, "Spectral and Dynamical Properties of Multiexcitons in Semiconductor Nanocrystals," Annu. Rev. Phys. Chem. **58**(1), 635–673 (2007).

172. F. T. Vasko, "Saturation of interband absorption in graphene," Phys. Rev. B - Condens. Matter Mater. Phys. **82**(24), 1–6 (2010).

173. Q. Bao, H. Zhang, Z. Ni, Y. Wang, L. Polavarapu, Z. Shen, Q. H. Xu, D. Tang, and K. P. Loh, "Monolayer graphene as a saturable absorber in a mode-locked laser," Nano Res. **4**(3), 297–307 (2011).

174. D. Li, L. Xue, Z. Zhu, X. Zhao, and J. Qian, "Graphene oxide nanoparticles for two-photon fluorescence imaging of zebrafish," Opt. Quantum Electron. **48**(11), 1–12 (2016).

175. X. Audier, N. Balla, and H. Rigneault, "Pump-probe micro-spectroscopy by means of an ultra-fast acousto-optics delay line," Opt. Lett. **42**(2), 294 (2017).

176. S. Keshavan, S. Naskar, A. Diaspro, L. Cancedda, and S. Dante, "Developmental refinement of synaptic transmission on micropatterned single layer graphene," Acta Biomater. **65**, 363–375 (2018).

177. A. El Merhie, D. Ito, I. Colombi, S. Keshavan, N. Mishra, V. Miseikis, A. Diaspro, C. Coletti, M. Chiappalone, and S. Dante, "Single layer graphene functionalized MEA for enhanced detection of neuronal network development," Sensors Actuators, B Chem. **277**, 224–233 (2018).

178. I. Pope, L. Payne, G. Zoriniants, E. Thomas, O. Williams, P. Watson, W. Langbein, and P. Borri, "Coherent anti-Stokes Raman scattering microscopy of single nanodiamonds," Nat. Nanotechnol. **9**(11), 940–946 (2014).

List of publications

Peer-reviewed journals

Zanini G., Korobchevskaya K., Deguchi T., Diaspro A., and Bianchini P., "Label-free optical nanoscopy of single layer graphene", ***under revision***.

Le Gratiet A., Pesce L., Oneto M., Marongiu R., **Zanini G.**, Bianchini P., and Diaspro A., "Circular intensity differential scattering (CIDS) scanning microscopy to image chromatin-DNA nuclear organization," *OSA Continuum* **1**, 1068-1078 (**2018**).

Book chapters

Bianchini P., **Zanini G.**, Diaspro A., "Label-free pump-probe nanoscopy", in Astratov V. (Ed.) *Label-free super-resolution microscopy*, Springer, ***in press***.

Conference proceedings

Le Gratiet A., Marongiu R., Pesce L., Oneto M., Bianchini P., **Zanini G.**, Diaspro A, "Label-Free Chromatin-DNA Imaging by Circular Polarized Light Scattering Scanning Microscopy", Biophysical Journal, 116 (3), 499a (**2019**).

Bianchini P., Korobchevskaya K., **Zanini G.**, and Diaspro A., "Pump-probe nanoscopy by means of transient absorption saturation", Proceedings of the 20th International Conference on Transparent Optical Networks (ICTON) (**2018**).

Bianchini P., **Zanini G.**, Korobchevskaya K., Oneto M., Pesce L., Diaspro A., "Resolution passion", European Biophysics Journal with Biophysics Letters, 46, S71 (**2017**).

Cainero I., Oneto M., Pesce L., **Zanini G.**, Lanzanò L., Diaspro A., and Bianchini P., "Combining expansion microscopy and STED nanoscopy for the study of cellular organization", Biophysical Journal, 112 (3), 140a (**2017**).

List of presentations

Oral presentations

Zanini G., Korobchevskaya K., Deguchi T., Diaspro A., and Bianchini P., *Exploring non-linear optical processes for label free microscopy*, Talk presented at the XXIV SIBPA (Società Italiana di Biofisica Pura e Applicata) national congress (**2018**), Ancona, Italy.

Zanini G., *Exploiting optical non-linearities in life sciences*, Invited talk presented at the Women in Photonics workshop (**2018**) at the Leibniz Institute of Photonic Technology, Jena, Germany.

Poster presentations

Zanini G., Korobchevskaya K., Deguchi T., Koike K., Kawagoe H., Oketani R., Smith N.I., Fujita K., Bianchini P. and Diaspro A, *Exploring non-linear processes for label-free microscopy,* Poster presented at the ELMI (European Light Microscopy Initiative) conference (**2018**), Dublin, Ireland.

Zanini G., Koike K., Kawagoe H., Oketani R., Smith N.I., and Fujita K., *Spatial resolution improvement of vibrational imaging with saturated Stimulated Raman Scattering microscopy,* Poster presented at the 43rd JSLM (Japan Society for Laser Microscopy) symposium (**2018**), Osaka, Japan.

Zanini G., Deguchi T., Dake F., Taki Y., Korobchevskaya K., Diaspro A., and Bianchini P., *Exploring saturation processes in near-IR transient absorption microscopy*, Poster presented at the FOM (Focus On Microscopy) conference (**2017**), Bordeaux, France.